Journal of Materials Chemistry A

ROYAL SOCIETY OF CHEMISTRY

REVIEW

View Article Online
View Journal | View Issue

Cite this: J. Mater. Chem. A, 2026, 14, 7909

A review on the recent advances in graphyne-based materials and their applications

Drisya G. Chandran, N. Ramkumar and Rima Biswas *

Graphyne-based materials (GBMs) have emerged as a versatile and promising class of carbon nanomaterials, featuring mixed sp- and sp^2-hybridized carbon atoms, and have garnered considerable attention in recent years owing to their unique electronic structures, tunable pore architectures, and exceptional mechanical and chemical stability. These distinct characteristics make them suitable for a broad spectrum of applications, including water purification, hydrogen storage, nanoelectronics, sensing, and catalysis. This review critically examines recent advances in GBMs from both experimental and theoretical perspectives. We highlight the synthesis methods, different structural properties, and diverse applications of GBMs, along with insights from density functional theory (DFT) calculations and molecular dynamics (MD) simulations. Advances in molecular modeling, particularly DFT, have provided an atomic-level understanding of the electronic structure, adsorption energetics, and reaction mechanisms, while MD simulations have provided deep insights into the transport mechanisms, hydration effects, energy barriers, and interaction dynamics within GBM frameworks. The current challenges associated with large-scale synthesis, cost-effectiveness, long-range structural order, crystallinity, operational stability under diverse conditions, toxicity, and integration into practical systems are critically examined. Finally, future directions are proposed to guide the continued advancement and real-world implementation of GBMs. This review serves as a valuable resource for researchers and engineers involved in the design and development of next-generation GBMs for sustainable technological applications.

Received 3rd November 2025
Accepted 6th January 2026

DOI: 10.1039/d5ta08904b

rsc.li/materials-a

Introduction

Over the past two decades, carbon-based nanomaterials have attracted exceptional scientific attention owing to their extraordinary structural versatility, tunable physicochemical properties, and transformative potential across diverse technological sectors. While graphene (GRA) has historically dominated the field of two-dimensional (2D) carbon materials because of its exceptional electron mobility, mechanical strength, and chemical stability,[1–3] increasing demand for functional diversity has driven interest toward graphyne (GY). Structurally, GY is composed of coexisting sp- and sp^2-hybridized carbon atoms arranged within a periodic framework incorporating acetylenic linkages.[4] This hybrid bonding scheme introduces an intrinsically porous lattice architecture absent in GRA,[5,6] endowing properties that can be selectively modulated through precise structural and chemical engineering.[7,8] The incorporation of carbon–carbon triple bonds into the GY lattice disrupts the purely sp^2 conjugation characteristic of GRA, thereby altering the electronic density of states and imparting anisotropic charge transport behaviour.[9] These modifications translate into tunable band gaps, enhanced chemical reactivity, and greater mechanical flexibility. Critically, the periodic distribution of intrinsic pores governed by the spatial arrangement of acetylenic linkages controls the molecular sieving and ionic transport phenomena. Such precision in mass transport has positioned GBMs at the forefront of next-generation membranes for selective ion separation, desalination, and gas purification.[7]

The escalating crisis of global water scarcity compounded by industrial pollution and climate change has intensified the demand for advanced water treatment and resource recovery technologies.[10,11] Industrial sectors such as mining, petrochemicals, and agrochemicals continue to discharge heavy metals, persistent organics, and other hazardous contaminants into aquatic systems, posing acute risks to both environmental safety and human health.[12] Considering that over 97% of the Earth's water exists as saline reserves, desalination has emerged as a critical strategy to augment freshwater supply.[13,14] Conventional desalination techniques including multi-stage flash distillation and thermal vapor compression suffer from high capital expenditure and significant energy consumption.[15,16] Membrane-based approaches, particularly reverse osmosis (RO), have gained market dominance due to their operational simplicity, scalability, and reduced carbon

School of Chemical Engineering, Vellore Institute of Technology, Vellore – 632014, Tamil Nadu, India. E-mail: rima.biswas@vit.ac.in

footprint.[17–21] However, conventional polymeric membranes face intrinsic trade-offs between permeability and selectivity, as well as susceptibility to fouling and chemical degradation. These limitations have spurred intense research into nanostructured membrane materials capable of achieving high salt rejection rates, rapid water flux, and long-term operational stability.[22,23] In this context, the atomic precision and inherent porosity of GY make it an ideal candidate for advanced separation platforms, as computational and experimental studies have shown superior ion rejection efficiencies and enhanced water permeability compared to conventional membranes.

Beyond water purification, GY's extended π-conjugation network and abundant active sites enable diverse applications in electrochemical energy storage, heterogeneous catalysis, and nanoelectronics.[24] As anode materials for Li, Na, and K ion batteries, GY frameworks have demonstrated high theoretical capacities, fast ion diffusion kinetics, and structural robustness under repeated cycling.[25,26] In catalysis, heteroatom-doped GY has exhibited remarkable activity for oxygen reduction reactions (ORRs), hydrogen evolution reactions (HERs), and CO_2 reduction, in many cases surpassing conventional carbon catalysts in both turnover frequency and stability.[24] Additionally, the tunable band gap and high carrier mobility render GY attractive for gas sensing, biosensing, and photodetection platforms.

Despite these promising prospects, large-scale synthesis of defect-free GY sheets remains a challenge, with current fabrication approaches such as cross-coupling polymerization, chemical vapor deposition (CVD), and on-surface synthesis yielding limited lateral dimensions and defect control. Here, computational materials science plays a decisive role in bridging the gap between theoretical potential and experimental realization.[27] Density functional theory (DFT) and molecular dynamics (MD) simulations offer complementary insights, enabling predictive modeling of electronic structures, adsorption energetics, ionic transport dynamics, and mechanical resilience prior to synthesis. Density functional theory, a quantum-mechanical framework, has been indispensable in elucidating the fundamental energetics and electronic configurations of GY-based systems. For instance, Deb *et al.*[28] proposed a novel carbon allotrope, pentagraphyne (PG-yne), and evaluated its potential as an anode material for Li and Na ion batteries using DFT calculations. Differential adsorption energy analysis indicated that PG-yne can accommodate up to eight Li or Na ions, achieving a high theoretical capacity of 680 mAh g^{-1}. Similarly, a three-dimensional (3D) porous GY-based structure (3D-PGY) and a sandwich-type composite of graphene/PGY/graphene (G/PGY/G) were developed by Liu *et al.*[29] When employed as the anode material for Li, Na, and K ion batteries, 3D-PGY delivers a theoretical specific capacity of about 558 mAh g^{-1}. The corresponding average open-circuit voltages for Li, Na, and K ion storage are 0.48/0.52/0.29 V for 3D-PGY and 1.08/1.04/1.39 V for the G/PGY/G configuration. In hydrogen storage research, Singh *et al.*[30] explored the hydrogen storage potential of zirconium (Zr)-decorated γ-GY monolayers using DFT and reported that each Zr atom anchored on the 2D γ-GY surface can adsorb up to seven H_2 molecules, exhibiting an average adsorption energy of −0.44 eV per H_2. This corresponds to a gravimetric hydrogen density of 7.95 wt% and a desorption temperature of 574 K, parameters well-suited for practical fuel-cell operation. Such studies exemplify how first-principles calculations can pinpoint optimal dopants, predict stable configurations, and quantify performance-limiting factors before experimental synthesis.

While DFT provides atomistic-level energy landscapes, it is inherently restricted in time and length scales.[31] Classical MD simulations address this limitation by enabling the exploration of atomic trajectories over nanosecond to microsecond regimes, thus capturing the dynamic interplay between ions, molecules, and the GY matrix under realistic thermodynamic conditions. Majidi *et al.*[32] leveraged MD simulations to examine the permeation behavior of Hg^{2+} and Cu^{2+}, through functionalized pores of γ-GY-1 nanosheets under an external electric field. The electrostatic interactions between ions and the –NH_2 group were stronger than those with the –COOH group, enabling the –NH_2 pore to facilitate higher ion permeation across all applied electric fields. At a more computationally intensive level, *ab initio* molecular dynamics (AIMD) incorporates quantum effects into dynamic simulations, making it invaluable for modeling adsorption–desorption cycles, thermal stability, and structural relaxation at finite temperatures.[33] Gao *et al.*[34] explored the hydrogen storage capability of holey graphyne (HGY), which exhibits strong potential for energy storage applications. Employing DFT and AIMD simulations, the authors investigated Li-functionalized single-layer HGY for H_2 storage. The DFT results indicated that Li atoms bind firmly to the HGY surface without exhibiting clustering tendencies, with each Li site capable of adsorbing up to four H_2 molecules at an average adsorption energy of −0.22 eV per H_2.

Previous reviews on GBMs have offered limited insights into their structural attributes, synthesis strategies, and functional applications,[24,27,35–38] and the existing literature remains fragmented, particularly lacking comprehensive analyses that concurrently address first-principles insights and dynamic simulations of GY systems. The emerging novelty and versatility of GBMs warrant a more comprehensive and unified examination. In particular, integrating both MD and DFT approaches is essential to unravel their fundamental mechanisms and to establish GBMs as indispensable materials for advanced environmental remediation and sustainable technologies. The synergistic integration of DFT and MD methodologies provides a multi-scale computational framework capable of guiding the rational design of GBMs for targeted applications. Accordingly, this review aims to bridge existing knowledge gaps by delivering an in-depth discussion of the recent advances in GBMs, with particular emphasis on DFT- and MD-based studies. We begin by outlining the structural diversity and synthesis strategies, followed by an overview of the intrinsic properties of GBMs, and key application domains reported in the literature. Subsequently, we critically evaluate computational studies, highlighting case examples that demonstrate the predictive and diagnostic capabilities of atomistic simulations. Finally, we discuss the current challenges and future research perspectives aimed at translating the unique potential of GBMs from theoretical models to practical technologies.

Structure of GBMs

A coherent understanding of GBMs necessarily begins with their atomic and topological structures, as these features dictate both intrinsic properties and functional behavior. Accordingly, this section focuses on the structural diversity of GBMs, establishing the foundation for subsequent discussions on synthesis, properties, and applications.

Interestingly, a novel family of carbon allotropes known as "Graphynes" emerged, which are one-atom-thick planar sheets made up of phenyl rings joined by acetylene bonds (–C≡C–). The existence of GY was hypothesized prior to the 1960s,[39] but it garnered significant attention following the discovery of fullerenes. Theoretical investigations into GY structures have been actively pursued since the 1980s. In 1987, Baughman *et al.*[40] described GY as a stable crystalline carbon allotrope with high degrees of sp hybridization, and it was named after graphite and ethyne because of the ethynyl units and aromatic moiety rings (which represent the sp- and sp^2-hybridized carbon).[41,42] The ratio of sp and sp^2 hybridized bonds defines the kinds of GY structures, such as α-GY, β-GY, γ-GY, graphdiyne (GDY), graphtriyne (GTY), graphtetrayne (GTTY), and δ-GY (6,6,12-GY) (see Fig. 1a–j).[43] They are referred to as GY-*n* based on the number of acetylene linkages and have a porosity of 18–25% caused by bonds between phenyl rings, giving GY an exciting future in ion permeation. Moreover, all allotropes of pristine GY contain intrinsic tunable holes, and they can perform well in ion rejection when compared to other nanoporous membranes.[44]

The size of the pores within the GY structure can be modified by changing the number of acetylene bonds between the adjacent benzene rings.[27] More specifically, GDY is a carbon allotrope featuring twin acetylenic groups with sp-hybridized acetylenic connections between neighbouring benzoic rings, which endow it with high π-conjugation. It was first suggested by Haley *et al.*[45] in 1997 and is expected to be one of the most stable diacetylene-containing sp^2 carbon compounds. Initial studies concentrated on the synthesis of GDY from structurally similar organic compounds and on the use of computational modeling of related materials to predict its fundamental properties.

The carbon–carbon triple bonds and uniformly distributed triangular pore structure of GDY provide numerous reactive sites and enable multiple reaction pathways, owing to its chemical decoration.[46] The presence of two acetylenic linkages effectively doubles the length of the carbon chains connecting the hexagonal rings.[47] Consequently, GDY does not retain the superior mechanical properties characteristic of GY. Graphdiyne exhibits a lower mechanical stiffness than that of GY and GRA, with an in-plane stiffness of 120 N m^{-1}. This corresponds to a Young's modulus of approximately 375 GPa, assuming a nominal thickness of 0.320 nm. While GDY is classified within the GY family, its distinctive properties often warrant separate consideration in research and applications.[47,48] Graphenylene is a 2D sp^2-carbon network generated by the fusion of hexatomic rings and tetratomic rings. In 2011, Balaban and Vollhardt[49] introduced the graphenylene structure. In recent times, graphenylene has received a lot of interest owing to its pore structure and thermodynamic stability. It has been employed as a membrane to separate gases, but not to desalinate water.[50]

Although the ideal atomic structures of GBMs elucidate the origin of their unique properties, their experimental realization is inherently governed by the feasibility of synthesis. The presence of sp–sp^2 hybridized carbon frameworks imposes significant kinetic and thermodynamic constraints, directly influencing crystallinity, defect formation, and structural fidelity. Therefore, a critical assessment of synthesis strategies is essential to bridge idealized structural models with experimentally attainable GBMs. The following section reviews the available synthesis routes, emphasizing their structural limitations and practical challenges.

Synthesis of GBMs

Initial strategies for the synthesis of extended GY networks have been proposed and gradually refined.[51,52] Notably, in 1994, Diederich[52] emphasized that the advancement in novel carbon phases heavily relies on precise organic synthesis techniques, particularly modern acetylene chemistry, bolstered by innovative organometallic synthetic strategies.

Furthermore, embracing unconventional strategies originating from diverse scientific fields could be pivotal in uncovering innovative and unprecedented synthetic routes. Early studies proposed that the controlled oligomerization of cyclocarbon could lead to the formation of γ-GY. Kehoe *et al.*[53] created three dehydrobenzoannulenes (DBAs a, b, and c) using an intramolecular cyclization strategy. Subsequently, the DBAs d and e were synthesized by Yoshimura *et al.*[54] using a combination of intramolecular bonding and double elimination. In 2008, Haley[55] outlined synthetic strategies for constructing substructures of the non-natural, planar carbon network GDY, utilizing the dehydrobenzo[56] annulene framework, and explored their optoelectronic properties. He further emphasized the critical need to extensively explore and employ metal-catalyzed cross-coupling, homocoupling, and metathesis reactions as key strategies for the successful synthesis of target GDY architectures. Advancing the synthesis of GY materials may involve utilizing surfaces as templates or scaffolds, similar to the strategies employed in the CVD of GRA from organic precursors on metal surfaces.[57] The value of synthesizing extended GY materials largely hinges on the unique properties that they are expected to exhibit, especially their electronic behaviour. Prominent GBMs development timelines are shown in Fig. 2.

In 2010, γ-GDY was successfully synthesized on copper substrates *via* the Glaser–Hay cross-coupling reaction using hexaethynylbenzene as the precursor.[58] Energy-dispersive X-ray spectroscopy (EDX) analysis indicates that the GDY film is composed exclusively of elemental carbon. The authors further utilized Raman spectroscopy to examine the structural uniformity and quality of the GDY film on copper foil and to verify the presence of characteristic carbon–carbon bonds predicted by its theoretical model. The results revealed the presence of both

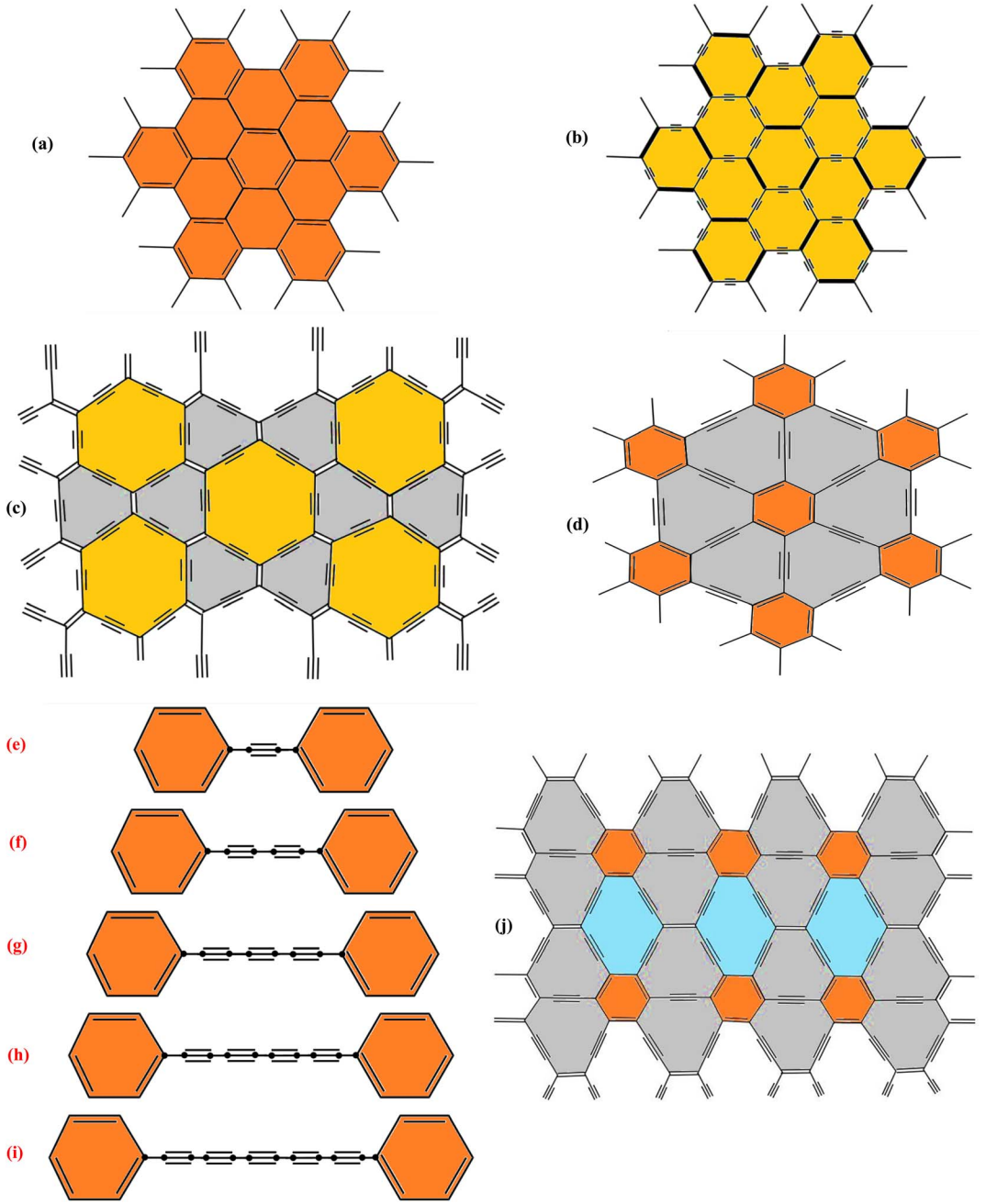

Fig. 1 Schematic of the structures of (a) GRA, (b) α-GY, (c) β-GY, (d) γ-GY, and γ-GY architectures: (e) γ-GY-1, (f) γ-GY-2, (g) γ-GY-3, (h) γ-GY-4, (i) γ-GY-5, and (j) δ-GY.

aromatic rings and carbon–carbon triple bonds, characteristic of the acetylenic linkages in GDY. These findings suggest the successful synthesis of GDY. The proposed approach enables the synthesis of nanometer-scale GDY and GTTY structures, albeit with limited long-range order. To further tailor the characteristics of GBMs for specific applications, researchers have investigated various functionalization strategies including substitution, heteroatom doping, and formation of GY-based nanocomposites. Initially, efforts were directed toward expanding the structural diversity of GY derivatives, leading to the first experimental synthesis of hydrogen-substituted graphyne (HsGY), which was accomplished by Deng and co-workers[59] through cross-coupling polymerization between 1,3,5-triethynylbenzene and 1,3,5-tribromobenzene. Over time, the structural integrity and stability of nanoscale GDY remained unresolved.

In this context, Yuan and Ding[60] systematically investigated the electronic and geometric structures of carbyne on various transition metal surfaces. They observed that on less reactive metals, carbyne adopts a polyynic structure, which tends to exhibit a curved geometry. In contrast, on catalytically active metal surfaces, carbyne prefers a linear polycumulenic

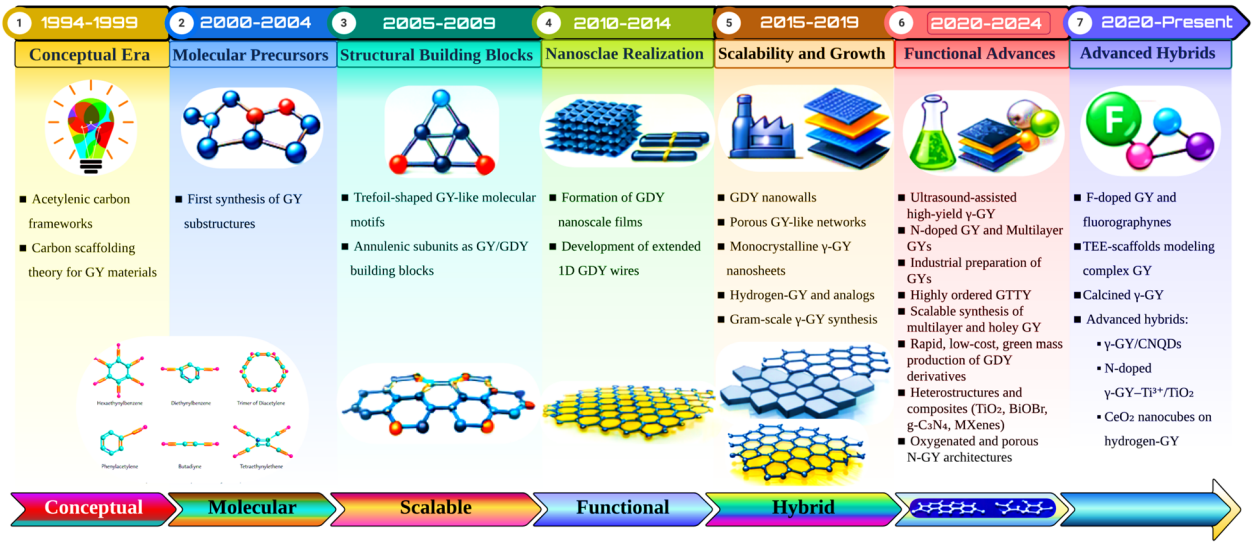

Fig. 2 Evolution and development timeline of GBMs.

configuration due to its greater stability. These structural preferences highlight the potential of metal-assisted self-assembly of carbyne as a strategic approach for the synthesis of GY.

Following these developments, the design and synthesis of GBMs have been extensively developed, enabling the creation of structures with different length scales.[61–63] In these studies, the coupling reaction of acetylenes serves as a pivotal method for synthesizing novel GY-type molecules and materials. However, the resulting materials often exhibit strong aggregation tendencies, complicating the fabrication of thinner films necessary to reveal their intrinsic properties and broaden their application spectrum. Addressing this challenge requires the rational design and synthesis of precursors, the development of effective connection methodologies, and the construction of GYs and GDYs with precise topologies and controlled thicknesses. Therefore, this underscores the pressing need for innovative strategies to engineer GYs with diverse structural configurations for advanced technological applications. In response to the challenges associated with synthesizing GY materials with specific topologies and reduced aggregation, Wu *et al.*[64] developed an alkyne metathesis reaction to synthesize a 2D GY-like porous carbon-rich network. The high catalytic reactivity of this synthesis method significantly reduces reaction time, effectively minimizing oxidation and aggregation. In order to synthesize a GY-like porous carbon-rich network, 1,3,5-tripropynylbenzene was utilised as the precursor, which underwent polymerization catalyzed by tris(*t*-butoxy)(2,2-dimethylpropylidyne)tungsten(VI) at 80 °C for 24 h under an argon atmosphere, without stirring. Beyond these synthetic strategies, hydrogen substitution has been explored as a means to further modulate GY properties. Although less frequently studied, hydrogen substitution provides a way to fine-tune the structural and electronic properties without substantially altering its conjugated network. This subtle modification can improve the material's stability, electronic tunability, and interaction with surrounding molecules, making HsGY a topic of growing interest. Theoretical studies suggest that GY is a promising candidate for the oxygen evolution reaction (OER) owing to its high charge carrier mobility.[65]

In a significant advancement, mechanochemical ball milling has been proposed as a low-cost and scalable approach to induce carbon–carbon bond rearrangements and generate GY-like structures without the need for metal catalysts or high-temperature processing. However, the structural nature of the materials produced *via* this method remains a subject of active debate. Early work by Li *et al.*[66] achieved the synthesis of a six-fold symmetric γ-GY spoked wheel (see Fig. 3) by employing a triyne intermediate (DBA f) and executing a 12-fold intramolecular Stille coupling reaction.

Cui *et al.*[67] later synthesized HsGY *via* a ball milling method, utilizing tribromobenzene ($C_6H_3Br_3$) and CaC_2 as precursors. By substituting $C_6H_3Br_3$ with hexabromobenzene (C_6Br_6), GY was subsequently synthesized using the same ball milling approach.[66] Subsequent mechanochemical advances enabled gram-scale γ-GY production, notably through the conversion of benzene using calcium carbide (CaC_2) under ball-milling conditions, as depicted in Fig. 4, highlighting the scalability and cost-effectiveness of this approach.[68,69] Nevertheless, structural analyses consistently indicate that such products exhibit limited crystalline coherence and high defect densities. Li *et al.*[70] synthesized HsGY films at the gas–liquid interface *via* an alkyne metathesis reaction using 1,3,5-tripynylbenzene (TPB) as the precursor. The resulting HsGY film exhibits a layered structure and is suitable as a sulfur host matrix for lithium–sulfur batteries (LSBs), owing to its extended π-conjugated carbon framework composed of acetylenic linkages and benzene rings. Song *et al.*[71] introduced an innovative and facile liquid/liquid interfacial synthesis strategy as a general approach for the preparation of GY analogs. This approach enabled the fabrication of various substituted GY analogs, including hydrogen-substituted (H-GY), methyl-substituted (Me-GY), and fluorine-substituted (F-GY) variants. These materials feature

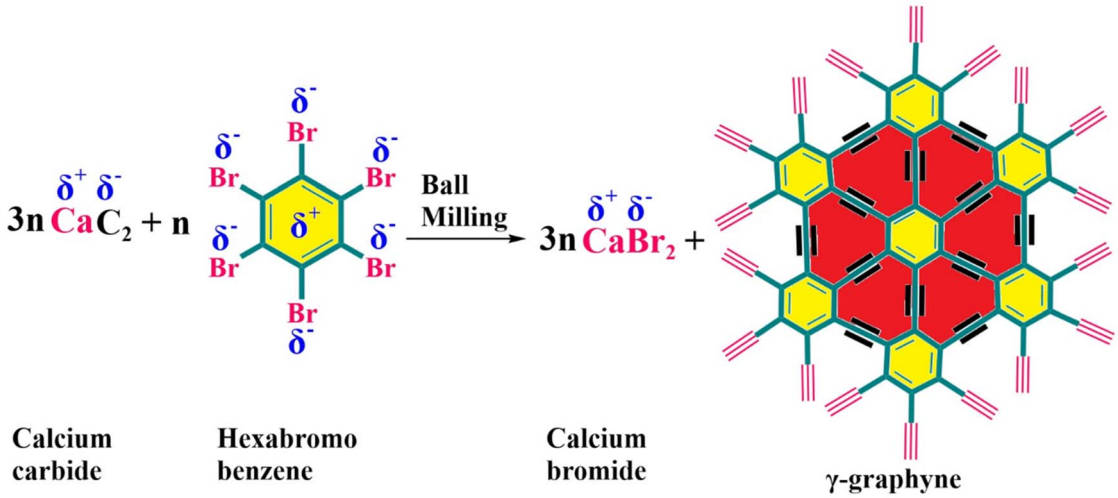

Fig. 3 Synthesis of γ-GY by the mechanochemistry method.[66]

a unique structural motif, characterized by a single acetylenic linkage between adjacent benzene rings, resulting in distinct pore architectures and electronic properties. The synthesized GY analogs formed continuous, large-area films with well-organized, gauze-like membrane structures observable at the micrometer scale. The electrical conductivities of H-GY, Me-GY, and F-GY were measured at 0.041 S m^{-1}, 0.076 S m^{-1}, and 0.028 S m^{-1}, respectively, highlighting the effect of functional substitution on their electronic performance. Yang *et al.*[72] prepared porous HsGY *via* liquid–liquid interfacial polymerization. Although considerable progress has been made in the study of GYs, their synthesis remains a significant challenge, primarily due to the difficulty in constructing acetylenic (C≡C) linkages.

In 2020, Lin *et al.*[73] further employed a modified mechanochemical route to synthesize γ-GY for photocatalytic applications, demonstrating functional utility but without resolving intrinsic disorder or establishing extended periodicity. Ding *et al.*[74] successfully produced γ-GY by using CaC_2 and hexabromobenzene ($PhBr_6$) as reactants through the sonochemical method. Atomically precise fabrication of well-defined nanostructures is possible using on-surface synthesis methods. Sedona *et al.*[75] reported the on-surface synthesis of extended linear GY molecular wires (GY MWs) through an Ullmann-type aryl halide homocoupling reaction. To circumvent the challenges associated with highly reactive terminal alkynes, the authors employed 1,2-bis(4-bromophenyl)ethyne (DBPE) as a molecular precursor. In this design, the acetylenic group is positioned internally, linked by two phenyl rings, each functionalized with a bromine atom at the para position. This configuration facilitates controlled linear homocoupling, leading to the formation of long GY MWs arranged in dense, ordered arrays. Moreover, Yu *et al.*[76] fabricated GY MWs through on-surface synthesis with stepwise reactions.

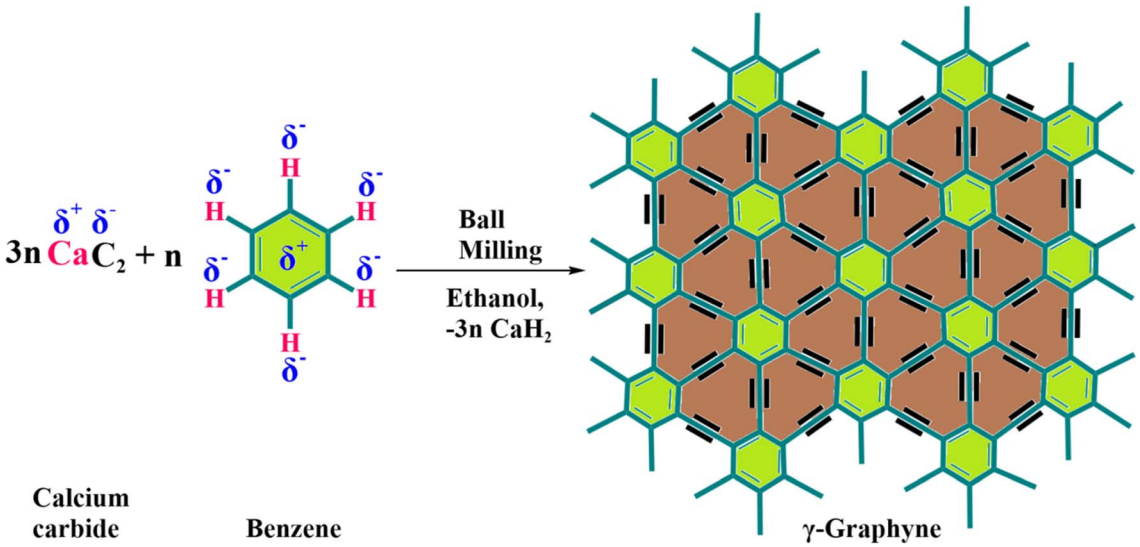

Fig. 4 Synthesis of γ-GY by the modified mechanochemical method with benzene and CaC_2 as precursors.[68]

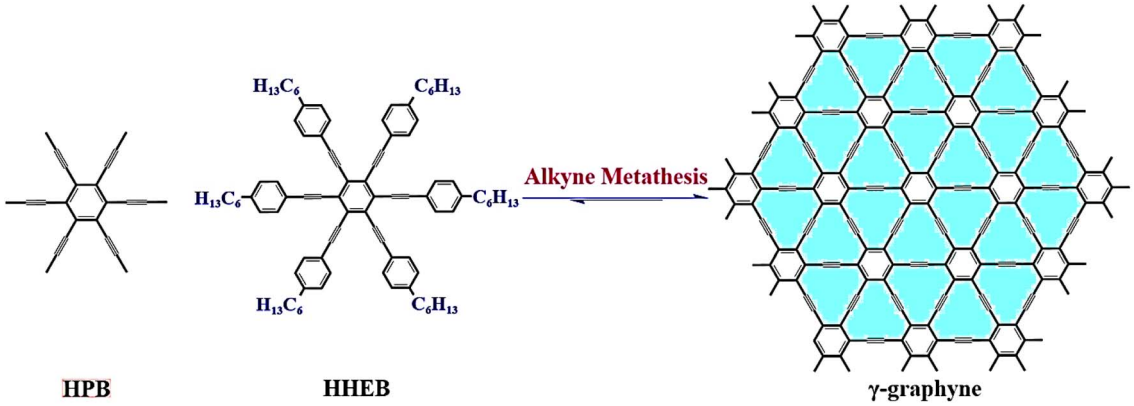

Fig. 5 Bulk synthesis of γ-GY through alkyl metathesis[82] using monomers 1,2,3,4,5,6-hexapropynylbenzene (HPB) and 1,2,3,4,5,6-hexakis [2-(4-hexylphenyl)ethynyl] benzene (HHEB).

Nitrogen (N)-doped GY incorporates nitrogen atoms into the carbon framework, introducing charge delocalization, modifying the electronic band structure, and creating chemically active sites. These changes significantly enhance the performance of GY in applications such as electrocatalysis, sensing, and energy storage. Ding *et al.*[77] reported a one-step ball-milling approach for the first facile synthesis of nitrogen-doped GY (N-GY) with controllable doping sites. By employing CaC_2 and pyrazine as reactants, nitrogen atoms were precisely incorporated into the γ-GY framework, leveraging pyrazine as both a nitrogen source and structural modifier. The resulting material showed an average yield of one gram. In a study by Abdi *et al.*,[78] a nitrogen-doped GY analogue called triethynylbenzene coupled with cyanuric chloride (TCC) was synthesized through a solvothermal (Sonogashira cross-coupling) reaction between 1,3,5-triethynylbenzene (1,3,5-TEB) and cyanuric chloride in an equimolar ratio. This approach enabled the formation of a conjugated network incorporating triazine moieties, introducing a nitrogen functionality into the carbon framework.

To overcome the challenges associated with constructing acetylenic (C≡C) linkages, recently one research group of Liang *et al.*[79] designed a novel precursor, 1,3,5-tris(tribromomethyl) benzene (tTBP), bearing tribromomethyl functional groups and successfully transformed this compound into a C≡C triple-bonded structural motif through on-surface dehalogenative homocoupling reactions conducted under ultrahigh-vacuum conditions. Drop-coating technique was employed by Gao *et al.*[80] to produce γ-GY/TiO_2 nanotube (GY/TNT) heterostructures. In a significant advancement in carbon allotrope research, Pan *et al.*[81] reported the direct bottom-up synthesis of crystalline GTTY using hexa(buta-1,3-diyn-1-yl)benzene as a precursor. The resulting GTTY exhibited a 2D lamellar architecture with uniform 0.9 nm pores, 80% sp-hybridized carbon atoms, a direct band gap of 1.3 eV, an electrical conductivity of 0.285 S m^{-1} at room temperature, and outstanding charge carrier mobilities of 1.47 × 10^3 cm^2 V^{-1} s^{-1} (holes) and 2.98 × 10^3 cm^2 V^{-1} s^{-1} (electrons).

Another study reported the synthesis of γ-GY *via* reversible dynamic alkyne metathesis reaction of alkynyl-substituted benzene monomers, which is depicted in Fig. 5. This work focused on reaction feasibility.[82] More recently, Yang *et al.*[83] have optimized mechanochemical parameters to enhance the dye adsorption performance, again confirming that localized acetylenic linkages can be introduced efficiently, yet long-range ordered γ-GY lattices remain elusive. However, growing evidence suggests that mechanochemical routes predominantly yield disordered or semi-ordered carbon frameworks with localized acetylenic linkages, rather than long-range ordered GY lattices.

Barua *et al.*[84] synthesized γ-GY *via* a one-pot Sonogashira cross-coupling reaction, employing $PhBr_6$ and CaC_2 as the primary reactants, and obtained an overall product recovery of approximately 80%, as shown in Fig. 6.

The synthesis of bulk γ-GY has long posed a significant challenge due to its complex structure and stability requirements. Desyatkin *et al.*[85] reported a breakthrough in this area by demonstrating the scalable synthesis of multilayer γ-GY *via* crystallization-assisted irreversible cross-coupling polymerization. This method enabled the formation of well-defined multilayer γ-GY crystals with structural integrity and uniformity, marking a major step toward the practical realization and exploration of this elusive carbon allotrope. Nitrogen-doped GY compounds (NGY-1 and NGY-2) were synthesized *via* the Sonogashira–Hagihara cross-coupling reaction, employing hydrogen-deficient multi-acetylene and polyhalogenated monomers as co-monomers.[86] The development of hybrid materials such as GY-based nanocomposites that integrate GY with metals, metal oxides, polymers, or other nanostructured materials has opened new possibilities for multifunctional materials. These composites leverage the intrinsic properties of GY while enhancing the mechanical strength, chemical functionality, and application-specific performance, particularly in catalysis, energy conversion, environmental remediation, and nanodevices. *Via* an *in situ* sonochemical process, Zheng *et al.*[87] prepared BiOBr nanocomposites with nitrogen doping on GY. Liu *et al.*[88] used a Castro–Stephens-type coupling reaction to synthesize ultrathin single-crystalline HGY with a new monomer called 1,3,5-tribromo-2,4,6-triethynylbenzene (see Fig. 7).

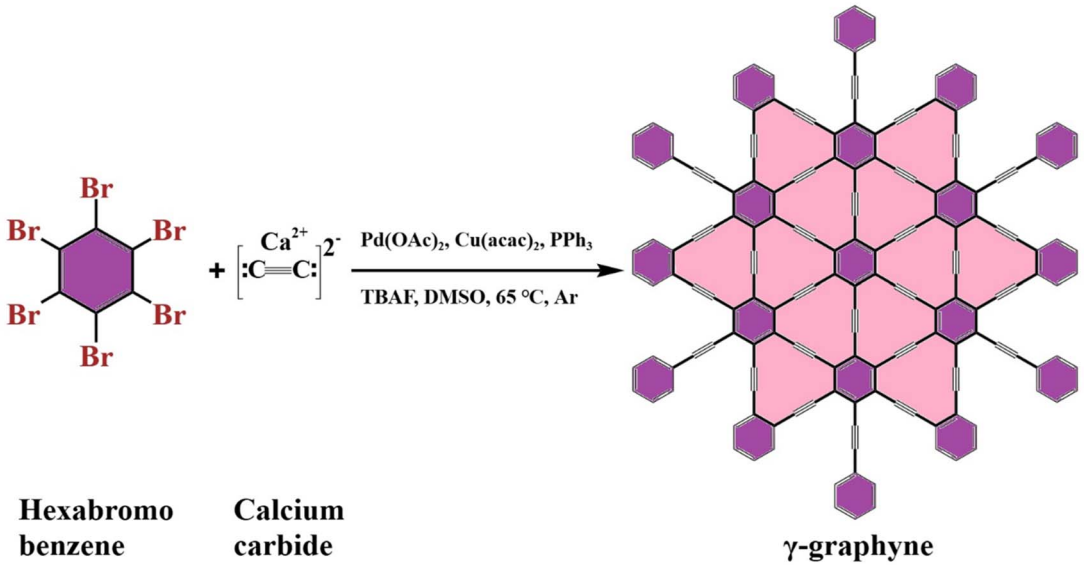

Fig. 6 One-pot Sonogashira cross-coupling reaction for synthesizing γ-GY.[84]

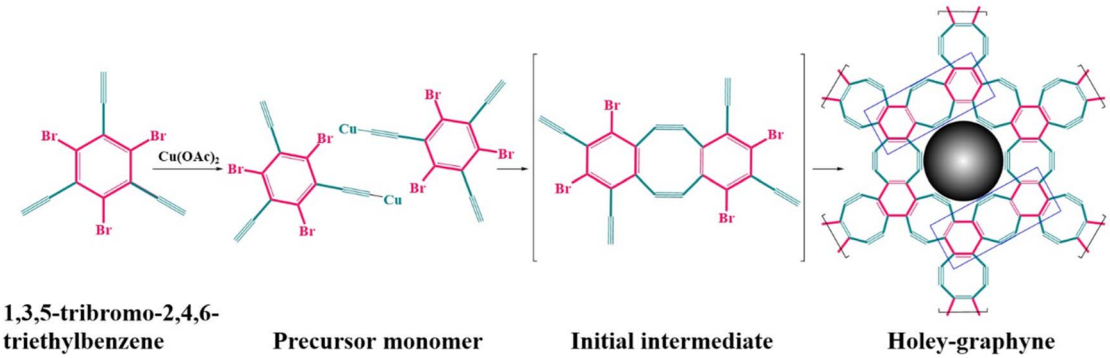

Fig. 7 Synthesis of ultrathin, single, crystalline HGY *via* the Castro–Stephens-type coupling reaction.[88]

The newly developed HGY was constructed by alternately linking sp^2-hybridized benzene rings with sp-hybridized C≡C bonds. It features large intrinsic pores with diameters in the range of approximately 0.8–1.0 nm.

Liu *et al.*[89] used a mechanochemical ball-milling strategy to construct GDY-based Ni-doped MoS_2 heterojunctions for photocatalytic hydrogen evolution. Here, mechanochemistry primarily enabled composite formation and interfacial charge-transfer engineering, with GDY embedded in a multiphase system rather than formed as a long-range crystalline network, highlighting the limitation of this approach for achieving ordered sp–sp^2 carbon lattices. The highly energetic and random nature of ball milling induces bond breaking and defect formation, which hinders the controlled assembly of long-range ordered sp–sp^2 carbon networks needed for true GY crystals. Wu and co-workers[90] produced titanium dioxide (TiO_2)/γ-GY nanocomposites. The controlled synthesis of GYs with specific topologies and desirable functional properties remains a major concern. To address this, He *et al.*[91] introduced a novel one-pot approach for the synthesis of γ-GY *via* a palladium (Pd)-catalyzed decarboxylative coupling reaction between hexabromobenzene and acetylenedicarboxylic acid (see Fig. 8). This method, conducted under mild conditions, offers a significant improvement over conventional techniques such as mechanical ball milling or ultrasonic-assisted synthesis. Notably, it enables the production of γ-GY with high yields and low equipment demands, making it a promising strategy for scalable and cost-effective manufacturing. Additionally, the resulting γ-GY-supported Pd nanoparticles exhibited high catalytic activity, further highlighting the practical potential of this approach.

Zhang *et al.*[92] fabricated a GRA/γ-GY heterostructure *via* a mechanosynthesis route, and the obtained material showed enhanced electromagnetic wave absorption across gigahertz and terahertz ranges. Moreover, this study demonstrates the strength of combining high-conductivity GRA with sp–sp^2 hybridized γ-GY to improve dielectric loss and impedance matching, leveraging the long-range order and crystallinity of both materials. While the approach is scalable and cost-effective, the reliance on pre-synthesized components and precise assembly limits uniformity over large areas, and

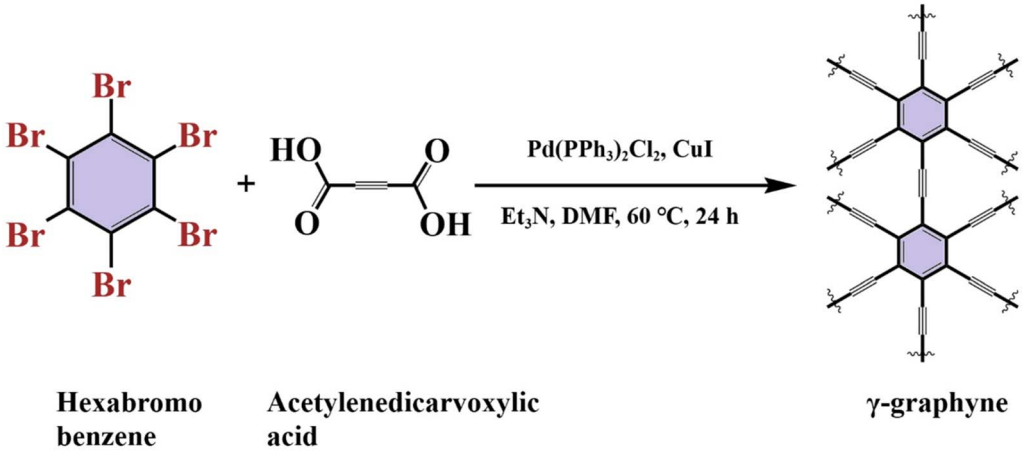

Fig. 8 One-pot synthesis of γ-GY.[91]

interfacial defects may reduce reproducibility and long-term stability. Yin *et al.*[93] employed a dehalogenative homocoupling reaction to synthesize hydrogen-substituted graphdiyne (HsGDY) in a powder form, providing a relatively simple, eco-friendly, and moderately scalable method. The work highlights the importance of hydrogen substitution in tuning the electronic properties and maintaining sp–sp^2 conjugation. While the method is mild and cost-effective, precise control

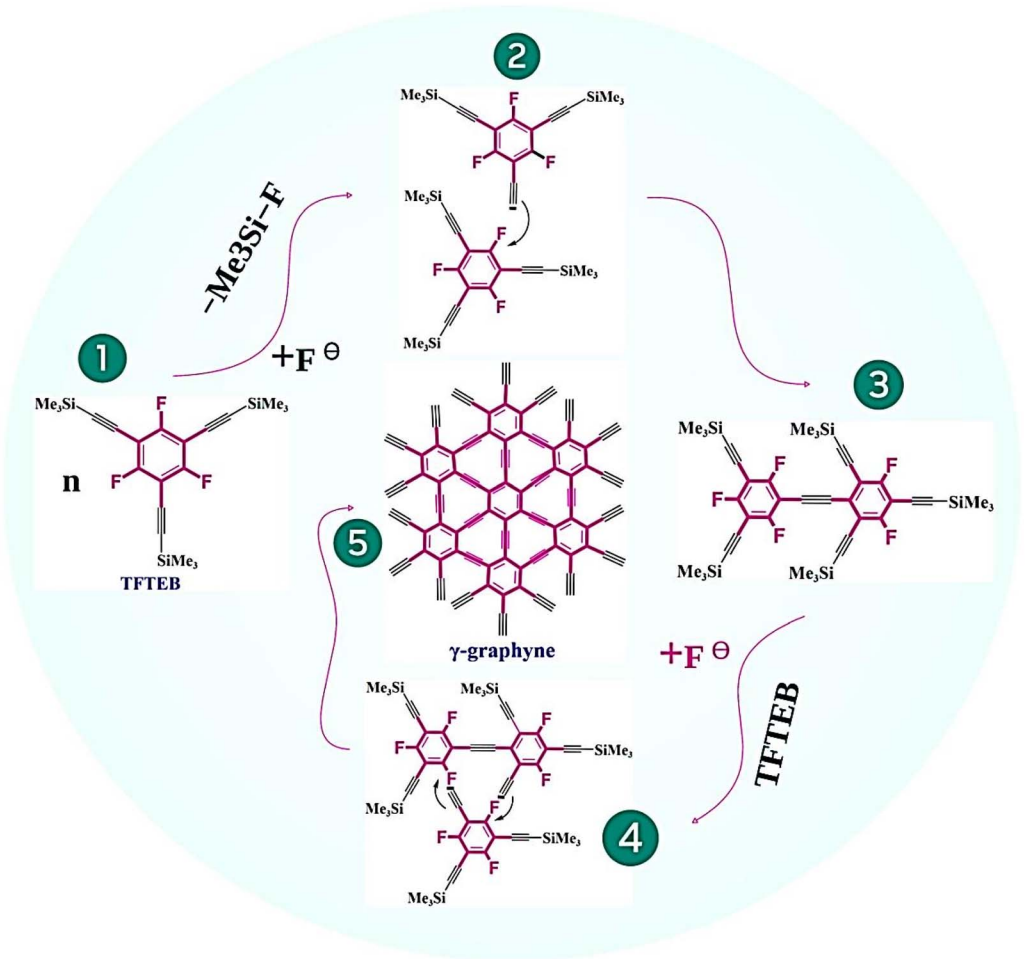

Fig. 9 Gram-scale fast synthesis of γ-GY using a metal-free wet chemistry method.[95] Reaction pathway represents the preparation of γ-GY from 1,3,5-trifluoro-2,4,6-tris[2-(trimethylsilyl)ethynyl]-benzene (TFTEB).

over hydrogen content and achieving uniformity across bulk samples remain challenges, potentially affecting the consistency of electronic performance in devices. Jin and Wu[94] introduced a green, high-yield preparation method for GDY and HsGDY using sustainable precursors under environmentally benign conditions. The method successfully balances scalability, cost-effectiveness, and environmental considerations. Although precise control over long-range structural order and domain size remains a challenge, their materials demonstrated efficient visible-light photocatalytic activity due to enhanced charge separation. However, the work also reveals the limitations: defect density and surface functionalization are critical factors, and uncontrolled defects can degrade photocatalytic stability, limiting practical application.

Rapid gram-scale synthesis of γ-GY and its functional derivatives using a straightforward metal-free wet-chemical method (see Fig. 9) was introduced by Song *et al.*[95] This approach relies on nucleophilic aromatic substitution reactions between fluoro-(hetero)arenes and alkynyl silanes, facilitated by catalytic TBAF. The fluoride ions effectively remove protecting groups from the alkynyl silanes, generating reactive alkynylide species that drive crosslinking. This versatile method tolerates a wide range of functional groups and enables the synthesis of diverse fluorine (F) and N-enriched γ-GY derivatives using electron-deficient fluoro-substituted (hetero)arenes as starting materials. The metal-free wet-chemical method offers a scalable and cost-efficient process inspiring the development of novel carbon-based materials.

Huang *et al.*[96] successfully fabricated ternary N-GY-Bi_2S_3/BiOBr composites *via* an *in situ* ultrasound-assisted method. In another study, Zhao *et al.*[97] reported the synthesis of nitrogen-doped GY/g-C_3N_4 (NGY/CN) composites *via* an *in situ* sonochemical method. For the effective removal of levofloxacin, Li *et al.*[98] developed flower-like N-GY/bismuth oxyhalide ($BiOCl_{0.5}Br_{0.5}$) microspheres *via* a simple, one-step sonochemical method. The incorporation of N-GY significantly improved both the adsorption capacity and the photocatalytic degradation efficiency under visible light, surpassing the performance of pristine $BiOCl_{0.5}Br_{0.5}$. This study also demonstrates the promising application of N-GY-based composites in advanced photocatalytic water purification. In an innovative approach combining environmental remediation and materials synthesis, Li *et al.*[99] suggested a green method for producing oxygen-doped GY through the mechanochemical degradation of decabromodiphenyl ether (BDE-209), a hazardous brominated flame retardant. The synthesized material demonstrated excellent electrical conductivity and a high specific capacitance of 257.6 F cm^{-3}, making it a strong candidate for electrochemical energy storage. This work not only presents a sustainable pathway for GY synthesis but also offers a practical solution for the disposal of persistent organic pollutants. Huang *et al.*[100] hydrothermally synthesized porous N-GY/TiO_2/Ti_3C_2 heterostructures with strong interfacial coupling and later[101] produced ternary *x*-N-GY/Bi/BiOBr composites *via* solvothermal synthesis, promoting efficient charge separation and superior photocatalytic activity.

Lee *et al.*[102] reported the fabrication of heteroatom-doped (F-doped) GY. Planetary milling was carried out to enhance the structural and electrochemical properties of GY. This approach facilitated the formation of fine particles and increased the content of alkynyl carbon, thereby promoting a higher density of electrochemically active sites and improving both electrical and ionic conductivity. Fluorine, possessing the highest electronegativity (3.98), introduces significant polarity and dipole moments into the GY framework upon doping. As a result, F-doping contributes to improved electrical conductivity and supports superior ultrafast cycling stability. The combined effects of alkynyl carbon and F doping in the GY structure suggest that F-doped GY holds strong potential as an active material for high-performance electrical double-layer capacitors (EDLCs). Krøll *et al.*[103] explored the stepwise synthesis of tetraethynylethene (TEE) scaffolds as molecular models for segments of 6,6,12-GY, an all-carbon network composed of interspersed sp-and sp^2-hybridized carbons within a GRA-like lattice. Utilizing a series of Sonogashira coupling reactions, the authors constructed various TEE derivatives starting from vinylic dibromide precursors and phenylacetylene. Through carefully controlled protodesilylation and cross-coupling steps, they obtained mono-, di-, and trimeric TEE structures with different arylation patterns, including fully substituted and linearly conjugated trimers. The synthesized TEE scaffolds exhibited excellent solubility in chlorinated solvents, providing well-defined model compounds for investigating the properties of 6,6,12-GY.

Shu *et al.*[104] reported F-functionalized GY decorated with transition metals for CO_2 electroreduction, where surface fluorination allowed the precise control of hydrophobicity and adsorption sites, yielding a material with high surface area, uniform active centers, and long-range structural order. The method is cost-effective, eco-friendly, and scalable, offering improved catalytic efficiency, though large-scale electrode fabrication and long-term stability remain challenges. Chen *et al.*[105] explored the effect of calcination temperature on γ-GY for simultaneous electrochemical detection of dopamine, uric acid, and ascorbic acid. Their thermal treatment approach fine-tuned the material's porosity, conductivity, and crystallinity, resulting in enhanced sensitivity and selectivity. While energy-efficient and scalable, precise temperature control is critical to reproducibility. Min *et al.*[106] fabricated γ-GY/graphitic carbon nitride quantum dot (CNQD) hybrids by a facile solution-based self-assembly method, improving the tribological performance of epoxy composites *via* strong interfacial interactions and uniform dispersion. The process is environmentally friendly and cost-effective, though uniform large-scale incorporation of quantum dots may be a challenge. Tian *et al.*[107] developed N-doped γ-GY coupled with Ti^{3+}-doped TiO_2 using hydrothermal-assisted *in situ* growth for photocatalytic green ammonia synthesis. The heterostructure exhibited enhanced visible-light absorption, charge separation, and abundant active sites, providing high efficiency with good crystallinity and structural order, though long-term stability under illumination remains a concern. Zhang *et al.*[108] synthesized highly dispersed cerium dioxide (CeO_2) nanocubes on HsGY sheets for room-

Table 1 Recent advances in the experimental synthesis of GBMs

Synthesis method	Graphyne-based material	Developments and limitations	Ref.
Gas–liquid interface *via* alkyne metathesis	HsGY films	Interface-confined growth enables film formation but crystallinity control remains limited; energy storage (Li–S batteries); high reversible capacity and cycling stability	70
Liquid–liquid interfacial synthesis	GY analogs	Continuous large-area films; gauze-like membranes; structures are polycrystalline with limited long-range order	71
Liquid–liquid interfacial polymerization	Porous HsGY	Good crystallinity; area up to 33 cm^2; high Na-ion storage performance; scalability, but synthesis complexity is high	72
Solid–liquid interface *via* mechanosynthesis	γ-GY	Direct benzene-to-γ-GY conversion; gram-scale; low environmental impact; scalable; long-range crystalline order over large areas remains elusive due to mechanochemical disorder	68
Stepwise on-surface approach	GY nanowires	Atomically precise nanowires; limited to surfaces and small areas; not scalable	76
On-surface Ullmann-like aryl halide homocoupling	Gy MWs	Long, linear, ordered molecular wires; requires UHV/metal substrates; limiting practicality	75
Modified mechanochemical method	γ-GY	GY-like frameworks with high defect density rather than ideal crystals; γ-GY as an electron transfer layer	73
Ultrasound-promoted method	γ-GY	Method is nontoxic, low cost, easy to be industrialized; high yield; structural heterogeneity persists; solar energy applications	74
Mechanochemical ball-milling	N-doped GY	Tunable N sites; effective for doping and functionalization but induces defects and amorphization	77
Sonogashira cross-coupling	N-GY	Controlled chemical bonding; limited film size and scalability	78
Dehalogenative homocoupling	HsGY	Short reaction time; large-scale industrial synthesis; metal-free advantage; crystallinity still moderate	79
Drop-coating method	γ-GY/TiO_2 nanotube array heterostructures	Environmentally friendly; GY acts as functional coating rather than standalone crystal; photoelectrochemical and photoelectrocatalytic application	80
Glaser–Hay coupling	GTTY	Highly ordered crystalline GTTY-average thickness of 4.5 nm; 80% sp-carbon content; precisely controlled and well-defined chemical structure	81
Modified mechanochemical method	γ-GY	Simple, efficient; prioritizes scalability over crystallinity	83
One-pot Sonogashira cross-linking	Pristine γ-GY	High yield, CaC_2 as the acetylene source; claims pure, defect-free structure under mild conditions; large-area crystallinity not established; energy storage, electronic, and optoelectronic applications	84
Sonogashira–Hagihara cross-coupling	N-doped GY	Copolymerization-based direct organic synthesis; high supercapacitor performance with excellent cycling properties; construction of functional heteroatoms-doped GY; strong chemical control; moderate scale	86
In situ sonochemical synthesis	N-doped GY/BiOBr composite	Composite-focused rather than intrinsic GY order; excellent photocatalysis	87
Castro–Stephens-type coupling	HGY	First, ultrathin, single-crystalline HGY; high structural precision but low throughput; applications in optoelectronic and energy-related fields	88
Crystallization-assisted irreversible cross-coupling polymerization	γ-GY	Scalable multilayer γ-GY; aperiodic sheet stacking; thermally stable up to 240 °C, transforms at higher temperatures; ordered covalent lattice formed under kinetic control	85
Mechanochemical	GRA/γ-GY heterostructure	Functional performance prioritized over structural perfection; as electromagnetic wave (EMW) absorber	92

Table 1 (*Contd.*)

Synthesis method	Graphyne-based material	Developments and limitations	Ref.
Dehalogenative homocoupling	HsGDY	Pd catalyst-free; short reaction time; scalable; improved practicality with moderate order; application in electrochemical catalysis	93
One-pot method	Few layer γ-GY	Easy to perform with mild reaction conditions, low-cost, high yield with low equipment requirements; outperforms ball milling or ultrasonic synthesis in yield but not crystallinity; application in catalysis	91
Hot-solvent method	GDY and HsGDY	Low cost; high yield; safer than traditional cross-coupling methods and mechanical routes; limited structural order; application in photocatalysis	94
Metal-free nucleophilic crosslinking method	GY and its derivatives	Fast, gram-scale synthesis; metal-free; scalable; cost-effective approach; reduced synthetic barriers for GY derivatives; functional group tolerance; significant step toward industrial feasibility; applications in catalysis	95
Hydrothermal method	Porous N-GY/TiO_2/Ti_3C_2 composites	First construction of porous N-GY/TiO_2/Ti_3C_2 composites; GY acts as active component in hybrids; superior photocatalytic activity	100
In situ sonochemical synthesis	N-doped GY/porous g-C_3N_4 composites	CaC_2-based synthesis; composite limits structural assessment; applications in photocatalysis	97
In situ sonochemical synthesis	N-GY/$BiOCl_{0.5}$–$Br_{0.5}$ microsphere	Functional integration emphasized; applications in photocatalysis	98
Solvothermal method	N-GY-Bi/BiOBr composites	3D microspheres; hierarchical architecture over crystallinity; applications in photocatalysis	101
In situ ultrasound-assisted synthesis	N-GY–GY/Bi_2S_3/BiOBr composites	First synthesis; superior photocatalytic activity; multi-phase complexity; applications in photocatalysis	96
Mechanochemical	Oxygenic GY	Green synthesis; hazardous decabromodiphenyl ether converted into oxygenic GY; highly ordered multilayered structure; electrode for supercapacitors; high electrochemical performance; excellent cycling stability	99
Planetary milling	F-doped GY	Excellent EDLCs performance; cycling stability; high doping efficiency, lattice order uncertain	102
Stepwise–Sonogashira couplings	6,6,12-GY	TEE scaffolds-molecular models of 6,6,12-GY segments	103
Aromatic nucleophilic substitution strategy	Fluorographynes	Tunable fluorine content enables wettability control; novel strategy for catalysts with tunable hydrophobic microenvironments; chemical versatility over crystallinity	104
Ultrasonic sonochemical method	Calcined γ-GY	Electrochemical sensing; structural disorder acceptable for sensing	105
Hydrothermal method	γ-GY/graphitic (CNQDs) hybrids	Advanced materials; hybrid functionality focus; aerospace applications	106
Mechanochemical	N-doped γ-GY/Ti^{3+}-doped TiO_2	Prepared for photocatalytic nitrogen fixation and enhanced photocatalytic activities; interface engineering dominates	107
Hydrothermal method	CeO_2/HsGY	GY as conductive scaffold; humidity-independent NH_3 sensing	108

temperature NH_3 sensing. The hydrothermal growth method ensured uniform nanocube distribution and excellent crystallinity, resulting in high sensitivity, selectivity, and humidity-independent performance, while precise nanocube size control is critical for consistent sensor functionality. The recent experimental and theoretical developments in GBM synthesis are presented in Tables 1 and 2.

Despite notable progress in GBM synthesis, the realization of large-area, highly crystalline, and defect-controlled materials remains limited, reflecting fundamental challenges that have persisted since the theoretical proposal of GY in the mid-1990s, including the thermodynamic instability of acetylenic linkages and the lack of efficient error-correction during growth. Early efforts through the 2000s and 2010s were largely limited to theoretical studies and molecular or oligomeric fragments, with GDY emerging as a more accessible analogue but without achieving long-range crystalline GY. From the late 2010s onward, multiple synthesis strategies have been explored, each involving intrinsic

Table 2 Recent theoretical advancements in GBMs

Material	Method	Theoretical advancement	Ref.
Oxygenated GY	DFT	Predicted tunable electronic band structure upon oxygen coverage; zero-gap to semiconducting transition *via* functionalization	109
α,β,γ-GY	DFT	First systematic first-principles evaluation of structural, elastic, electronic properties including band structures, Fermi velocity, strain effects	110
cp-GY (carbon pentagons + acetylenic links)	DFT	Novel low-energy GY polymorph; distorted/anisotropic Dirac cones and semimetallic nature-new electronic possibilities	111
Doped/heteroatom GY/GDY	DFT	Predicted mechanical, optical and electronic properties of GY with B, N, P, Al dopants; tunable band features	112
PG-yne	DFT	Energetically more favorable than other GY family members, including experimentally synthesized GY and GDY; dynamically, thermally, and mechanically stable up to 1000 K; high carrier mobility with excellent optical properties; promising for future electronic and optoelectronic applications	113
D GY-like covalent triazine framework (GYCTF)	Dispersion-corrected DFT	Functionalized GY-like frameworks; Mg-ion adsorption and surface interactions on GY derivatives for battery applications	114
Nonconventional α-GY nanocarbon	DFT	Proposal of nonconventional GY lattices inspired by sp^2 nanocarbon haeckelites; systematic mapping of the structural and electronic properties of modified α-GY nanocarbons	115
PG-yne	Atomistic reactive MD simulations	Mechanical properties and fracture behavior of PG-yne monolayers and nanotubes; structural topology strongly influences elastic constants; PG-yne systems-extended, topology-independent plastic deformation region prior to fracture	116
R-GY	DFT	Theoretical HER/OER activity predicted for novel R-GY; demonstrating GY's catalytic potential	117
α-2 GY based catalysts	DFT + machine learning (ML)	Large-scale DFT screening, integrated with machine learning, identifies stable dual-atom catalysts on graphyne, highlighting TM–TM DACs as a promising catalyst class with high electroactivity and long-term durability	118
γ-GY	Density functional tight binding method within the DFTBEPHY framework	Advanced modeling of electron–phonon coupling and charge transport in semiconducting GYs; GYs exhibit GRA-like electronic properties with intrinsic band gaps; phonon-limited mobilities lie between GRA and MoS_2 for GY and are comparable to MoS_2 for GDY	119
TH-GY	DFT, AIMD, and classical reactive MD simulations	Novel 2D allotrope that combines triangular (T) and hexagonal (H) rings, connected by acetylenic linkages; AIMD and phonon analyses confirm thermal and dynamical stability; band structure calculations reveal metallic behavior and a Young's modulus of 263–356 GPa	120

trade-offs between crystallinity, scalability, and process complexity. On-surface synthesis under ultra-high vacuum provides unparalleled atomic-level precision and well-defined acetylenic coupling, serving as a critical proof of concept, yet its stringent vacuum conditions, substrate dependence, low throughput, and sub-millimeter growth areas fundamentally preclude scalable production. CVD, despite being the most scalable approach for 2D materials, has thus far failed to yield highly crystalline GY, as high growth temperatures promote competing sp^2 carbon formation, bond rearrangements, and irreversible defect accumulation, resulting in polycrystalline or amorphous GY-like films with limited domain sizes. In contrast, solution-based, mechanochemical, and ultrasonic-assisted routes developed after 2020 enable gram-scale production of γ-GY and related derivatives under comparatively mild, cost-effective, and in some cases, metal-free conditions, making them attractive for large-scale processing; however, limited reaction control leads to high defect densities, incomplete acetylenic coupling, stacking disorder, and poor long-range order, causing material properties to fall well below theoretical expectations.

A notable advance in the 2022–2025 period is the emergence of crystallization-assisted irreversible cross-coupling polymerization. This approach enables bulk solution polymerization of multilayer γ-GY, where a crystallization step promotes long-range ordering and network growth beyond surface-confined domains. Unlike conventional Sonogashira or Glaser coupling methods, which often yield small fragments or require stringent surface control, this strategy (i) operates in bulk solutions and is therefore scalable, (ii) forms extended covalent networks rather than isolated oligomers, and (iii) yields significantly larger material quantities.

As a result, it offers the best balance between structural quality and scale-up potential. A very recent development reports a metal-free nucleophilic wet-chemistry route that produces γ-GY derivatives at gram scale under mild conditions. Gram-scale production at bench level is an important milestone: it demonstrates that reagents and reaction conditions can be adapted to produce larger batches without transition-metal catalysts (*i.e.*, reducing cost and contamination issues). This metal-free wet route thus represents a highly practical path to scale because it simplifies reagents and reactor conditions. Overall, no single method yet satisfies the combined requirements of large-area growth, high crystallinity, low defect density, scalability, cost-effectiveness, and environmental benignity: on-surface synthesis excels in structural precision, CVD in scalability, and mechanochemical routes in cost and throughput, but each suffers fundamental limitations. As of 2025, crystallization-assisted and metal-free wet-chemical strategies represent the most promising pathways toward practical GBMs, provided that future efforts prioritize defect-aware growth, precursor design, and rigorous structure–property correlations. In this context, theoretical advancements play a critical complementary role. Table 2 summarizes the recent progress in DFT and the advanced simulation approaches that elucidate structure–property relationships and thus guide experimental efforts. These studies offer predictive insights into thermodynamic stability, preferred bonding motifs, and feasible lattice topologies, enabling rational selection of precursors, functional groups, and synthesis conditions. Furthermore, theoretical screening of functionalization, doping, and lattice engineering strategies identifies promising GY allotropes with targeted electronic, mechanical, and catalytic properties prior to experimental realization, thereby reducing trial-and-error synthesis and accelerating the development of scalable, application-ready GBMs.

Fundamental properties of GBMs

Beyond enabling material fabrication, synthesis routes define the structural realism of GBMs, thereby setting the limits of their measurable properties. Variations in bonding integrity, defect distribution, and layer uniformity arising from different synthesis approaches have a direct impact on the properties of the resulting materials. GY is a novel 2D carbon allotrope that exhibits a combination of unique structural and physicochemical properties. Unlike GRA, which consists solely of sp^2-hybridized carbon atoms, GY incorporates both sp and sp^2 hybridizations due to the presence of acetylenic linkages between benzene rings. This hybrid bonding imparts GY with exceptional mechanical strength, thermal stability, and chemical robustness, while also enabling selective permeability and high surface area. These distinctive attributes have sparked growing interest in GY and its analogues for various applications. The properties of GBMs can be broadly categorized into mechanical, thermal, electronics, magnetic, optical, and structural domains (see Fig. 10). Accordingly, the following sections provide a concise overview of aforementioned properties, highlighting relevant findings from various studies and their implications for practical applications.

Mechanical properties

One of the notable attributes of GY is its exceptional mechanical properties, making it a subject of significant research interest.[121,122] The mechanical behavior of GBMs is primarily

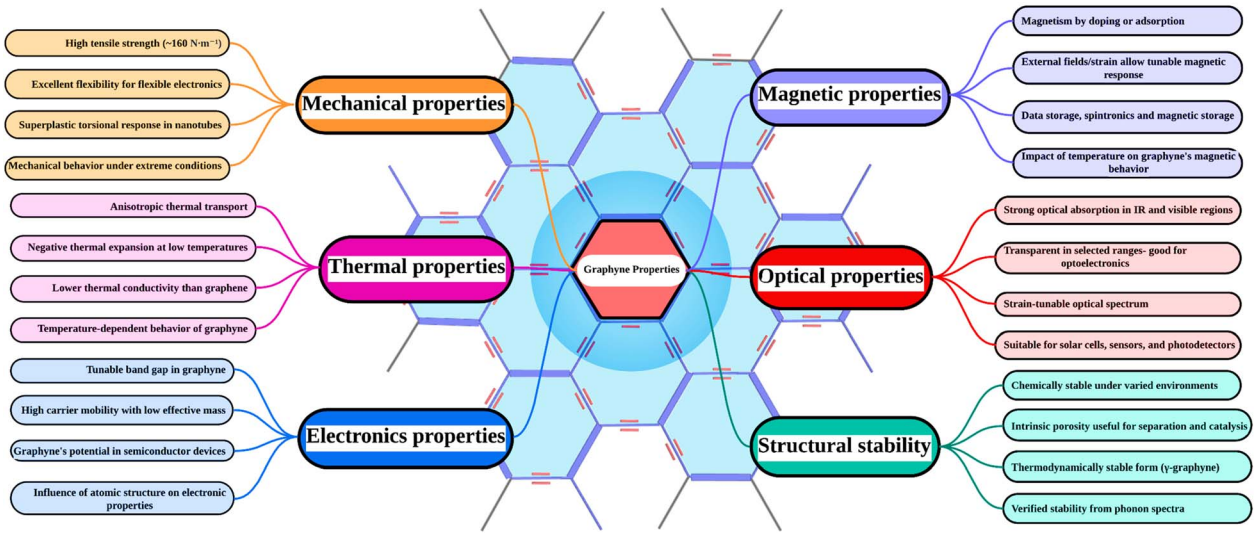

Fig. 10 Schematic highlighting the versatile properties of GBMs.

attributed to the presence of acetylenic linkages. These linkages play a crucial role in determining key mechanical properties, such as Young's modulus and fracture stress, thereby influencing the overall strength and structural integrity of the material. The mechanical properties are observed both in infinite sheets[123–125] and at the nanoscale in flake-like structures. Cranford and Buehler[124] employed MD simulations using the ReaxFF (Reactive Force Field) potential to examine the mechanical properties of GY flakes. Their study revealed notable tensile strength and fracture strain values under both armchair and zigzag loading conditions, underscoring the material's mechanical resilience and anisotropic behavior. In a separate study, Yang and Xu[126] explored the various effects of acetylenic group incorporation on the mechanical behavior of GY family structures under applied tensile loads. Using MD simulations, they observed that under armchair loading, the fracture strain remained nearly constant, while tensile strength progressively decreased with the elongation of acetylenic chains. Conversely, under zigzag loading, the tensile strength remained relatively unchanged, whereas a slight increase in fracture strain was noted. This behavior was attributed to the lower atomic density and reduced number of bond linkages within the molecular plane of GBMs.

Despite having half the density of GRA, it retains comparable interfacial adhesion and out-of-plane deformation to GRA. Key elastic properties including in-plane rigidity and Poisson's ratio influence its mechanical behavior. Poisson's ratio of GYs is 0.429, which is twice that of GRA. Moreover, the value approaches that of a perfectly incompressible material (0.5). Thus, GY demonstrates high structural preservation under tensile stress.[123] Theoretical studies indicate that γ-GY has a lower in-plane strength than that of GRA (*i.e.*, 170–240 N m^{-1}) but remains the most stable under shear stress.[124,127] Poisson's ratio exhibits a steady decrease from γ-GY to α-GY, indicating that γ-GY demonstrates the highest structural stability under shear stress, whereas α-GY shows lower stability.[124] The fracture limit of the γ-GY network is path-dependent, as revealed by uniaxial tensile tests. Young's modulus was determined to be 532.5 GPa in the armchair direction and 700.0 GPa in the zigzag direction, highlighting its anisotropic mechanical behavior. The ultimate tensile strength of GY-*n* is predicted to follow a linear scaling relationship, being directly proportional to the number of atomic linkages within the structure. Fracture analysis indicates that crack initiation predominantly occurs at weaker single bonds within the acetylenic linkages, ultimately leading to the catastrophic failure of the entire sheet.[125] In-plane stiffness and Poisson's ratio are key elastic parameters used to characterize the mechanical behavior of GBMs. Studies have shown that these materials typically exhibit lower in-plane stiffness than GRA.[123,128] Furthermore, their Poisson's ratios, ranging from 0.39 to 0.87, are notably higher than that of GRA.[129]

Ajori *et al.*[130] examined the impact of vacancy defects on the mechanical properties of GY, specifically strain, stress, Young's modulus, and Poisson's ratio, through MD simulations utilizing the Tersoff–Brenner potential. Their study revealed that GY exhibits reduced mechanical strength and stiffness in comparison to GRA, highlighting the influence of structural defects on its overall mechanical performance. Nonetheless, research by Shao *et al.*[131] and Zhang *et al.*[132] suggests that the mechanical properties of GBMs may vary with temperature. Although these initial studies offer important observations, further investigation is needed in this area to fully understand and characterize the temperature-dependent behavior of GBMs. Wu *et al.*[133] conducted MD simulations with the adaptive intermolecular reactive empirical bond order (AIREBO) potential to assess the fracture stress, fracture strain, and stiffness of GY structures under armchair and zigzag loading conditions. Their results demonstrated that the number of acetylenic chains connecting the hexagonal rings strongly depends on the mechanical properties of GBMs. Recently, Xiao *et al.*[134] have experimentally investigated the mechanical properties of GDY films for the first time using atomic force microscopy (AFM) nanoindentation techniques. The measured three-dimensional elastic modulus ranged from 145.6 to 273.6 GPa, with an average value of 218.5 GPa. This experimentally determined elastic modulus is notably lower than the ideal theoretical value, which can be attributed to the presence of structural defects and the finite thickness of the synthesized GDY films. Previous studies have shown that the elastic modulus of carbon nanostructures decreases significantly with the increase in vacancy.[135] In addition, Xiao *et al.*[134] reported a pronounced reduction in elastic modulus with the increase in layer number in GDY films, further highlighting the strong influence of thickness and structural imperfections on their mechanical performance. GY exhibits notable impact resistance and distinctive elastic wave propagation behavior, indicating strong structural robustness for protective nanomaterial applications.[136] The elastic properties of γ-GY are highly sensitive to nanoscale dimensions, an important consideration for the design of nano-mechanical devices.[137] Mechanical anisotropy and deformation behavior have been shown to depend strongly on atomic configuration and bonding topology.[138] Combined DFT and continuum modeling approaches have been employed to evaluate the stiffness and compliance constants across different GY allotropes, revealing pronounced variations in elastic constants with the type of structure.[139] Recent studies have emphasized fundamental mechanical parameters such as breaking strength and failure strain derived from stress–strain responses, underscoring the suitability of GY for flexible nanoelectronic applications.[140] Furthermore, MD simulations have elucidated the effects of wrinkling, fracture mechanisms, and anisotropic tensile loading in various GY configurations, providing deeper insights into mechanical failure processes.[141] Across all reviewed studies, the mechanical parameters consistently demonstrate that GBMs possess robust mechanical stability, reinforcing their potential as promising candidates for membrane-related applications.

Thermal properties

Thermal transport properties are critical considerations for materials used in nanotechnology and related fields, as they directly impact the efficiency and functionality of nanoscale

Table 3 Different properties of GBMs along the x and y directions of their structures

Properties	Ultimate strength, σ (N m^{-1})		Ultimate strain, ε (%)		In-plane stiffness, C (N m^{-1})		Poisson's ratio, ν		Hole, μ_h ($\times 10^4$ cm^2 V^{-1} s^{-1})		Electron mobility, μ_e ($\times 10^4$ cm^2 V^{-1} s^{-1})		
Direction	σ_x	σ_y	ε_x	ε_y	C_x	C_y	ν_x	ν_y	μ_{hx}	μ_{hy}	μ_{ex}	μ_{ey}	Ref.
GY	17.84, 16.68, 14.34, 14.44	18.83, 21.16, 31.97, 20.47	20, 11.2, 8.19, 11.2	20, 14.8, 13.24, 17.7	166, 170.4, 166.3, 162.1, 150, 170.2, 164, 163	224.0, 169.2, 162.5, 159.6	0.417, 0.416, 0.429, 0.42, 0.39	0.42, 0.38	—	—	—	—	123–126, 128 and 172–174
GDY	10.71, 9.54	13.54, 20.84	6.3, 10.9	8.0, 20.8	123.1, 150.2, 100, 118.6, 121.8	185.2, 117.5	0.446, 0.40, 0.453	0.40	1.91	1.97	17.22	20.81	48, 126, 172 and 174–176
α-GY	10.88	12.18	15.6	17.8	39.9, 24, 21.98, 22.48, 42.8	40.2, 42.4	0.863, 0.87, 0.874, 0.72	0.72	2.960	3.316	2.716	3.327	110, 125, 174 and 176–178
β-GY	12.75	15.50	13.0	16.2	87.1, 83.77, 73.07, 93.6	87.4, 92.1	0.49, 0.647, 0.67, 0.52	0.51	0.856	1.076	0.798	0.892	110, 125, 174, 176, 177 and 179
6,6,12-GY	13.09, 34.71, 30.15	20.64, 41.94, 35.85	11.6, 0.134, 0.13	14.7, 0.191, 0.2	117.3, 121.1, 347, 348, 333, 341.09	149.1, 152.1	0.39, 0.164, 0.169, 0.18	0.49	12.29	42.92	24.48	54.10	110, 125, 172, 174, 176, 180 and 181

devices. Several theoretical approaches have been employed to investigate the thermal conductivity of GBMs, including the use of non-equilibrium MD simulations,[142,143] equilibrium MD with the Green–Kubo approach,[144] and the Boltzmann transport equation framework.[145,146] These diverse methodologies offer complementary perspectives on phonon transport and thermal behavior in GBMs, enhancing the predictive understanding of their heat conduction properties. Zhang *et al.*[147] investigated the thermal conductivities of four GBMs and observed a significant reduction in thermal conductivity, primarily attributed to the presence of acetylenic linkages. These linkages introduce lower atomic densities and weaker single bonds, which hinder efficient heat transport. Among the structures studied, 6,6,12-GY uniquely exhibited anisotropic thermal conductivity, distinguishing it from the other GY-n sheets analyzed. Ouyang *et al.*[148] explored the thermal transport properties of γ-GY nanoribbons and reported that their thermal conductance is approximately 40% lower than that of GRA. Different properties of GBMs are tabulated in Table 3.

Interestingly, the study found that the thermal conductance remained largely unaffected by the presence of acetylenic linkages. The thermal characteristics of 2D materials are influenced by interatomic spacing, leading to reduced thermal conductivity at higher temperatures.[149] The lower molecular density and weaker single carbon bonds in the acetylene link contribute to a significant reduction in GY's thermal conductivity.

Notably, the thermal conductivity of GY is primarily determined by the number of aromatic rings rather than the presence of alkyne bonds. Additionally, both temperature and external strain influence the thermal sensitivity of GY structures. Hu *et al.*[150] reported that pristine γ-GY nanotubes possess exceptionally low thermal conductivity, substantially lower than that observed in typical, defect-laden, or chemically modified carbon nanotubes (CNTs). Zhang *et al.*[151] examined the thermal conductivity of δ-GY and found that it consistently decreased with the increase in temperature, a behavior attributed to the influence of acetylenic linkages within the structure. This observation, along with similar findings from previous studies, highlights the inherent challenge of heat transport in GBMs, which stems from their characteristically low thermal conductivity. The minimal thermal efficiency of α-GY, β-GY, and γ-GY are 0.920, 1.650, and 2.456, respectively.[152]

An additional area of growing interest is the thermoelectric performance of GBMs. Environmentally safe thermoelectric materials enable direct conversion between heat and electricity, with GY exhibiting superior thermoelectric characteristics compared to GRA. Despite their relatively low thermal conductivity compared to GRA, GBMs have demonstrated promising thermoelectric behavior in theoretical studies. The inherent band gaps in their electronic structures are key contributors to enhanced Seebeck coefficients, leading to a potentially high thermoelectric figure of merit. These characteristics make GBMs attractive candidates for next-generation thermoelectric materials, as supported by the findings previously reported in the literature.[145,146,153] Typically, an ideal thermoelectric material is expected to exhibit a dimensionless figure of merit (ZT) greater than 3. In a study by Sun *et al.*,[153] ZT values of 3 and 4.8

were reported for p-type holes and n-type electrons, respectively, in GBMs at 293 K. These results were obtained by integrating MD and first-principles simulations with the Boltzmann transport theory. Such high *ZT* values highlight the strong potential of GBMs as promising candidates for high-performance thermoelectric applications. Studies on GRA/GY heterostructures showed that thermal conductivity is significantly reduced by defects, due to increased phonon scattering.[154] DFT calculations show that acetylenic linkages significantly reduce GY's thermal conductivity, which decreases with the increase in temperature due to enhanced phonon scattering, indicating strong potential for thermoelectric applications.[155] The MD results indicate that Sun-GY exhibits an intrinsically low thermal conductivity (*i.e.*, $\sim$24.6 W m^{-1} K^{-1} at 300 K), several orders of magnitude lower than GRA (*i.e.*, $\sim$3000 W m^{-1} K^{-1}), due to strong phonon scattering induced by acetylenic linkages and reduced phonon group velocities.[156]

Electronic properties

Electronic properties are among the most essential attributes governing a material's functionality in various technological applications. For GBMs, a thorough understanding of their electronic structure is crucial for tailoring their performance in fields such as nanoelectronics, optoelectronics, and energy storage. As such, investigating the electronic characteristics of GBMs is fundamental to unlocking their full potential in both theoretical and applied research. Strain-induced band gap energy variations affect the electronic characteristics of α, β, and γ-GYs.[157] From a theoretical perspective, GBMs exhibit remarkable electronic characteristics, particularly due to their intrinsic and tunable band gaps ranging between 0.44 and 2.23 eV. This contrasts sharply with GRA, which inherently lacks a band gap, thereby constraining its applicability in semiconductor-based electronic devices.[158–160] The incorporation of carbon–carbon triple bonds in GBMs imparts distinctive electronic characteristics, such as reversed chirality and shifted Dirac cone momentum, which collectively contribute to the tunability of their band gaps.[161] Dirac cones, initially known as a hallmark of GRA's electronic structure, have also been theoretically predicted in GBMs using first-principles calculations, underscoring their distinct electronic behavior and expanding their potential in next-generation electronic devices.[158] The Brillouin zone of γ-GY with directional anisotropy and rectangular symmetry showed two distorted Dirac cones. The separation between the upper and lower Fermi level positions of the two Dirac cones gives rise to self-doped semiconducting behavior. These findings indicate that the presence of a Dirac cone is not a unique feature of GY. Furthermore, the emergence of Dirac cones does not require a high crystal lattice symmetry, and can occur even at low-symmetry points within the structure.

Numerous studies have proposed tight-binding models to describe the p_z/p* bands, aiming to enhance the understanding of the electronic structures of various GBMs and to elucidate the conditions governing the presence or absence of Dirac cones.[162] Owing to its asymmetric structure, γ-GY features two characteristic edge terminations, commonly referred to as armchair and zigzag configurations. Additionally, theoretical studies indicate that γ-GY nanoribbons exhibit semiconducting properties, with armchair and zigzag forms yielding band gaps of 0.59–1.25 eV and 0.75–1.32 eV, respectively.[163] GY nanoribbons with either zigzag-like or divan-like edge configurations demonstrate low band gaps in the range of 0.4 to 0.9 eV and exhibit impressive charge carrier mobilities, reaching values as high as 3104 cm^2 V^{-1} s^{-1}. Moreover, GDY and GDY nanotubes exhibit significantly higher distortion potential parameters than GRA or CNTs, attributed to the stronger bonding strength of triple bonds.

Experimental investigations of GDY films grown on substrates have measured their electrical conductivity and confirmed intrinsic semiconducting behavior.[41] At room temperature, the electrical conductivity of GDY films was reported to be approximately 2.52×10^{-4} S m^{-1}, indicative of semiconducting charge transport. This conductivity is comparable to that of silicon and several orders of magnitude lower than that of GRA, thereby experimentally validating the semiconducting nature of GDY. In another study, GDY has been demonstrated as a tunable electrode material, with electrochemical reactivity governed by its electronic structure and surface chemistry.[164] Oxidation to graphdiyne oxide (GDYO) and subsequent chemical (cr-GDYO) or electrochemical (er-GDYO) reduction significantly enhances electron-transfer kinetics, yielding performance comparable to CNTs and GRA-based electrodes. These results highlight GDY as a promising material for carbon electrochemistry and electroanalytical applications.

Among the various parameters governing the performance of semiconducting materials, electron mobility plays a pivotal role. Notably, GBMs possess inherently high electron mobility.[165,166] The electronic properties of GBMs can be notably influenced by the stacking arrangement of their layers, as variations in stacking methods introduce distinct interlayer interactions that modify the overall electronic behavior. León and Pacheco[167] explored the electronic characteristics of bilayer GBMs under different stacking configurations for both metallic and semiconducting variants. Their findings revealed that in the semiconducting form, the band gap can be effectively modulated by altering the stacking arrangement. Zheng *et al.*[168] investigated the effects of stacking on the electronic properties of GBMs, specifically focusing on bandgap and charge mobility. They found that the Bernal stacking of benzene rings led to the most energetically stable configurations for both bilayer and trilayer GBMs. Compared to single-layer GBMs, these stacked structures exhibited reduced bandgaps and demonstrated metallic characteristics, indicating a significant modulation of electronic behavior based on stacking arrangements. In these multilayer configurations, the bandgaps were notably reduced compared to the intrinsic bandgap of monolayer GBMs. Moreover, the bilayer and trilayer systems exhibited metallic behavior as a result of their specific stacking arrangements. Additional in-depth investigations have highlighted the presence of intrinsic band gaps and enhanced electronic properties in GBMs with various layering and stacking configurations.[157,169,170] First-principles calculations reported a GY

allotrope with a Dirac nodal line electronic structure, showing semi-metallic bands that could enable high-speed electron transport similar to GRA.[171]

Scalable synthesis of multilayer γ-GY was demonstrated with a direct band gap of ~0.48 eV, experimentally confirming that GY can behave as a semiconductor rather than a metal.[85] A first-principles study showed that AB-stacked γ-GY bilayers have a tunable band gap (*i.e.*, ~1.26–1.88 eV) controlled by biaxial strain, demonstrating how mechanical strain can modulate electronic structure for device design.[182] Recent computational work predicted high carrier mobilities: electrons up to $\sim 10^4$ cm^2 V^{-1} s^{-1} and holes $\sim 10^3$ cm^2 V^{-1} s^{-1} at room temperature, making GY competitive with established 2D semiconductors for transistor channels.[119]

Magnetic properties

The magnetic properties of carbon-based materials have attracted significant attention due to their potential applications as lightweight, non-metallic magnets and their promising prospects in the field of spintronics.[165,183] In general, GY nanoribbons subjected to zigzag directional loading tend to exhibit a magnetic semiconductor ground state, characterized by ferromagnetic ordering at the edges with opposing spin orientations. In contrast, those loaded along the armchair direction typically behave as non-magnetic semiconductors, with their band gap depending on the ribbon width.[166] Furthermore, the electronic structure of GBMs can be effectively tuned through the adsorption of 3d transition metal atoms, which induces spin polarization and imparts notable magnetic properties, transforming them into spin-polarized semiconductors. Zhang *et al.*[184] experimentally investigated the paramagnetic behavior of pristine GBMs and those doped with nitrogen. Their findings showed that nitrogen doping enhanced the paramagnetic properties of GBMs, resulting in a more pronounced and well-defined saturated magnetic moment compared to the undoped counterpart. Notably, the introduction of asymmetric pyridinic nitrogen *via* substitution reactions led to a significant local magnetic moment of $0.98\mu_B$. These results suggest that pyridinic nitrogen is more effective in enhancing the magnetic properties of GBMs than simple nitrogen site doping. In a subsequent investigation, the researchers successfully fabricated a hybrid composite of GBMs doped with ferrous ions using an efficient and low-cost synthesis method. This composite demonstrated notable ferromagnetic behavior, underscoring its promise for future applications in magnetic and spintronic devices.[184] Zhan *et al.*[185] reported the synthesis of cobalt-doped GDY nanosheets that exhibit clear room-temperature ferromagnetism. The cobalt atoms form a kagome lattice and provide magnetic moments, producing ferromagnetic behavior not seen in undoped GDY.

Transition-metal doping in GY-like allotropes such as B-GY can induce spin splitting and half-metallicity, making these materials promising for spintronic applications with tunable magnetic characteristics driven by strong d–p orbital coupling.[186] Strain and magnetic field modeling of γ-GY predicts alterations in magnetic susceptibility and transport properties under external magnetic fields, suggesting the sensitivity of magnetic responses to mechanical and field conditions.[187] Kang *et al.*[188] performed magneto-transport experiments on nitrogen-doped GDY, showing distinct negative and positive magnetoresistance behaviors at low temperatures, indicating magnetic carrier interactions and tunable magnetic transport behaviour. Device-level theoretical work on zigzag γ-GY nanoribbons demonstrates gate-tunable fully spin-polarized currents and pure spin currents, indicating practical routes for generating and controlling spin polarization without conventional ferromagnets.[189] Additionally, first-principles modeling of HGY reveals potential for collinear antiferromagnetic ground states *via* specific impurity adsorption strategies, offering a novel type of magnetism in 2D p-electron systems.[190] These advances establish GBMs as flexible platforms for magnetism and spin transport in nanoscale devices.

Optical properties

Furthermore, these materials have excellent optical features, which are characterized by their absorption behavior, resulting from light interaction with electrons and atoms.[177] Zheng *et al.*[191] synthesized GDY *via* cross-coupling reactions and experimentally characterized its optical properties. They observed that GDY exhibits a strong ultraviolet photoluminescence (PL) peak at ~397 nm and optical absorption around ~280 nm, attributed to its π-conjugated carbon network and the presence of oxygen-containing functional groups that induce charge transfer and light emission. The α-, β-, and γ-GY's demonstrate high electron polarization, as indicated by their large static dielectric permittivity (absorption coefficient) at zero photon energy. The β-GY's absorption decreases with the increase in energy due to resonance effects. All three GYs exhibit strong absorption and reflectance in the infrared-to-visible range, with γ-GY exhibiting the highest absorption in the visible spectrum. This entire figure of merit makes GY an attractive candidate for water purification.[192,193] Recently, 8-16-4-GY has been predicted to exhibit optical transparency with strong infrared activity, demonstrating the influence of topology on optical spectra.[194] Nie *et al.*[195] prepared the GDY-polymethyl methacrylate (PMMA) composite films and measured nonlinear optical properties using laser characterization techniques. These GDY-PMMA films demonstrated a nonlinear modulation depth of ~4.94% and significant nonlinear optical response in the near-infrared region, suitable for photonic applications such as mode-locked fiber lasers. Irida-GY showed a strong anisotropic photoresponse, enabling polarization-dependent optoelectronic applications.[196] The BN-GY analogues were predicted to possess intense UV absorption and visible transparency, expanding the photonic potential.[197] The DFT/TD-DFT studies on 6,6,12-GY fragments revealed visible-range one- and two-photon absorption enhanced by solvent effects,[198] while layered γ-GY showed stacking-induced redshifts in absorption peaks.[199] Raman analyses of GY, GDY, and GTY further elucidate the role of acetylenic units in light-matter interactions, reinforcing their optical tunability.[200]

Structural and stability properties

A clear understanding of the structural and stability properties is crucial for the development of high-performance carbon-based nanoscale materials. Structural optimization approaches such as edge functionalization and the modulation of ribbon width play a significant role in enhancing both the mechanical integrity and overall stability of these materials. Using DFT, Bai *et al.*[201] explored the structural and stability characteristics of GDY nanoribbons. Their findings indicated that one-dimensional GDY nanoribbons possess higher cohesive energies, and thus, greater energetic stability, than the 2D GDY sheets. Additionally, nanoribbons with zigzag edge terminations were found to be more stable than those with armchair configurations. Enyashin and Ivanovskii[202] studied the structural and stability properties of various fluorographynes *via* DFT calculations. Their study demonstrated that the incorporation of F atoms significantly enhances the stability of GY sheets, with stability increasing proportionally to the fluorine-to-carbon ratio. Conversely, a higher proportion of sp^1-hybridized carbon atoms in the GY framework was shown to negatively impact the stability of both pristine and fluorinated GY structures. Qu *et al.*[179] established a correlation between the structural configuration of GBMs and their elastic properties. The findings revealed that an increase in the proportion of acetylenic linkages leads to a reduction in both in-plane stiffness and layer modulus while resulting in a higher Poisson's ratio. These structural dependencies were primarily attributed to variations in bond density. Employing MD simulations, Solis *et al.*[203] explored the structural stability of GY and GDY nanoscrolls. Their results demonstrated that all examined structures were capable of forming stable nanoscrolls, primarily due to the greater porosity of GY and GDY compared to GRA. This increased porosity leads to a reduction in π–π stacking interactions, thereby promoting the formation and stability of the scroll architecture.

GDY has been extensively characterized using multiple experimental structural techniques including scanning electron microscopy (SEM), transmission electron microscopy (TEM), X-ray diffraction (XRD), Raman, X-ray photoelectron spectroscopy (XPS), Fourier transform infrared (FT-IR) spectroscopy, and AFM.[204] These measurements confirm the presence of a planar porous structure with uniformly distributed sp–sp^2 carbon and verify the successful synthesis and structural integrity of GDY films and powders. These methods also help correlate structural features (*i.e.*, pore distribution and bonding environments) with the material's properties. TEM and high-resolution transmission electron microscopy (HRTEM) reveal that synthesized GDY exhibits a lamellar porous structure with a clear interlayer spacing (*i.e.*, ~0.365 nm) and abundant pore channels, which are key structural features that influence stability and functionality.[205] The observed morphology indicates a stable layered form, although with some amorphous features due to structural defects. The γ-GY has been experimentally synthesized using a modified mechanochemical method. Structural confirmation was performed using Raman spectroscopy, XPS, XRD, SEM, and TEM, which verify the co-existence of sp and sp^2 carbon and reveal the morphology and chemical bonding consistent with expected GY structures.[83] Although thermal or mechanical stability tests were not emphasized in this work, the successful synthesis and stable structural identification represent an experimental milestone toward future functional testing. In a bottom-up on-surface synthesis approach on Au(111), GY- and GDY-based molecular wires were formed and structurally characterized both *in situ* (*i.e.*, *via* scanning tunneling microscopy (STM) and XPS) and *ex situ* (*i.e.*, *via* Raman spectroscopy).[206] These structural analyses showed stable formation of sp-hybrid atomic frameworks with distinct triple-bond signatures, and the Raman spectra provided evidence of structural stability under ambient conditions, demonstrating that these atomic wires remain intact after synthesis and exposure to air.

The diverse physicochemical properties of GBMs form the foundation for their proposed technological applications. However, the practical relevance of these properties depends on how effectively they can be exploited under realistic operating conditions. In this context, the following section critically examines how material properties influence various application domains.

Applications of GBMs

GBMs have received growing attention for their wide range of technological applications, as shown in Fig. 11. The following subsections emphasize the versatile applications of these novel materials in multiple domains. The tunable bandgap and excellent charge transport characteristics make GBMs promising materials for applications in nanoelectronics, sensors, and optoelectronic devices. Its intrinsic porous architecture and strong chemical stability also support its use in membrane separations, gas purification, and next-generation energy storage technologies. Beyond these, GBMs demonstrate notable potential in catalysis, hydrogen storage, and various energy conversion processes. Moreover, its structural flexibility and inherent biocompatibility broaden its relevance to biomedical technologies and environmental remediation strategies.

Metal ion removal using GY-based membranes

One of the primary areas where GBMs are currently gaining significant attention is water purification. In addition to their well-established properties, GBMs exhibit exceptional potential as an advanced separation membrane for wastewater treatment. Their structurally tunable nanopores allow for the efficient passage of water molecules while blocking contaminants, making them highly suitable for membrane-based separation systems. These materials also possess highly adjustable surface energies and exhibit superhydrophobic behavior.[157] Compared to GYs, GDYs are semipermeable and feature multiple continuous channels that enable the transport of a substantial amount of water under applied pressure while effectively rejecting ions.[207,208] The performance of these nanoporous channels can be further enhanced through functionalization or by introducing negative surface charges, thereby improving both water permeability and salt rejection efficiency.[209] A

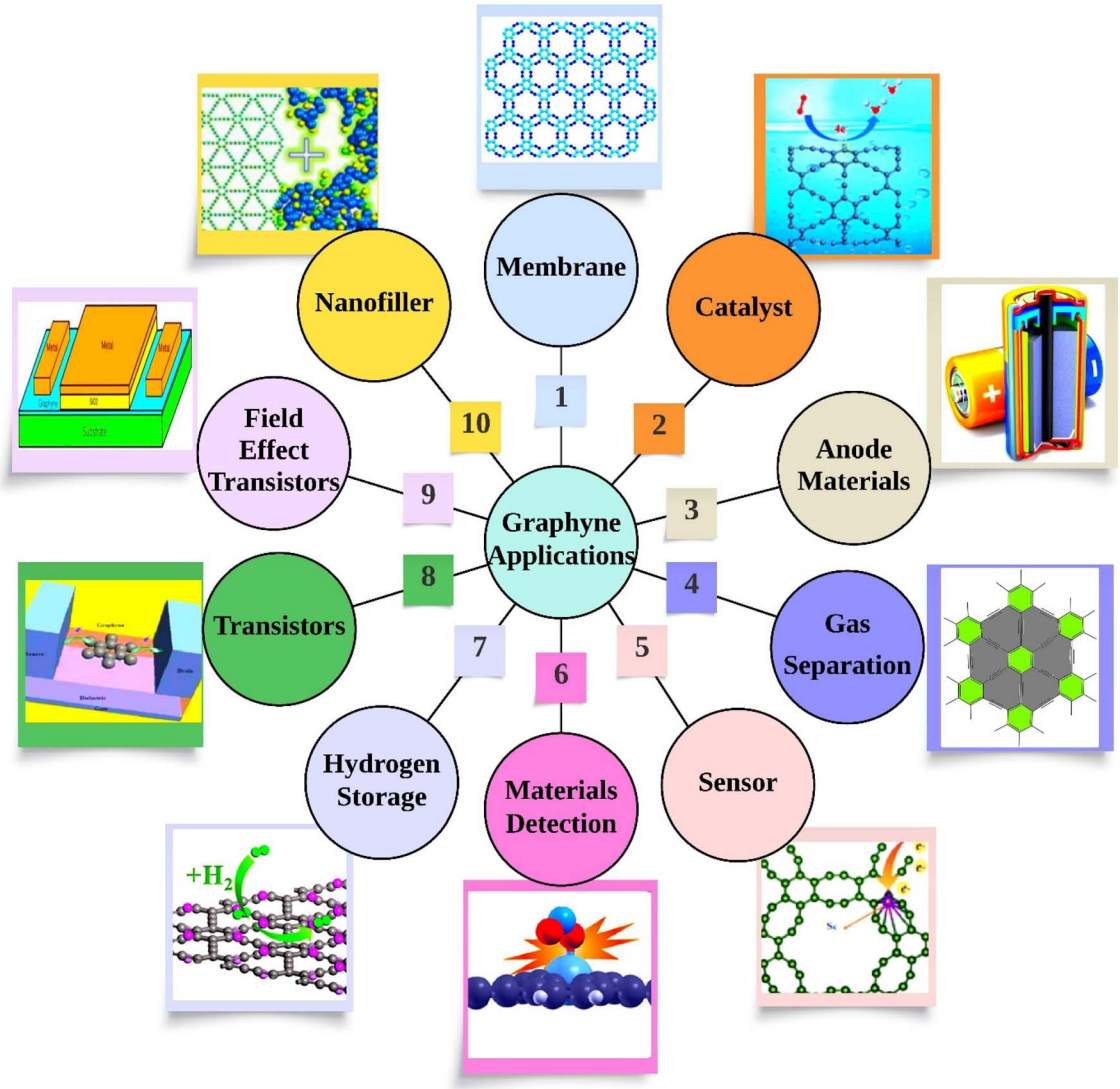

Fig. 11 Applications of GBMs in multiple fields.

distinctive feature contributing to the performance of GBMs is the presence of triple carbon–carbon bonds, which induce a momentum shift in their Dirac cones. This shift allows for tunability in the energy bandgap, a condition that enhances electron mobility and enables surface modifications tailored for specific separation applications.[35,161]

The promising role of GBMs in contaminant separation for water treatment has been explored in numerous studies. The investigation of GBMs as membranes has largely relied on theoretical and computational methodologies. These approaches are particularly effective for predicting material behavior, uncovering mechanisms behind complex or poorly understood phenomena and interpreting unexpected experimental findings.[210] Computational modeling also provides valuable guidance for identifying optimal material configurations and supports informed decision-making in selecting suitable materials for specific applications, such as in the design of GY-based membranes. The predictive studies have been reported on GY and its related structures.

Researchers are interested in γ-GY (see Fig. 12a–h) due to its high conjugation, profusion of chemical carbon bonds, extraordinary chemical inertness, and excellent electrical, optical, and physiological properties.[157] Xue *et al.*[193] performed water desalination on five different pristine GYs using MD simulations and first-principles calculations. The resulting water fluxes displayed a linear dependence on the applied hydrostatic pressure. A performance comparison between α-GY, β-GY, and γ-GY-3 and conventional RO membranes revealed that these GYs can achieve water permeability at 100% salt rejection that is two orders of magnitude higher than that of commercial RO membranes. Thus, the monolayer γ-GY-3 membrane, exhibiting the best performance, was confirmed as a promising candidate for use in water filtration and desalination applications.

In contrast, GDY was impermeable to both water and ions even under a pressure of 250 MPa, indicating its unsuitability for desalination applications. Water transport is vital for understanding the flow behaviour at extremely small length

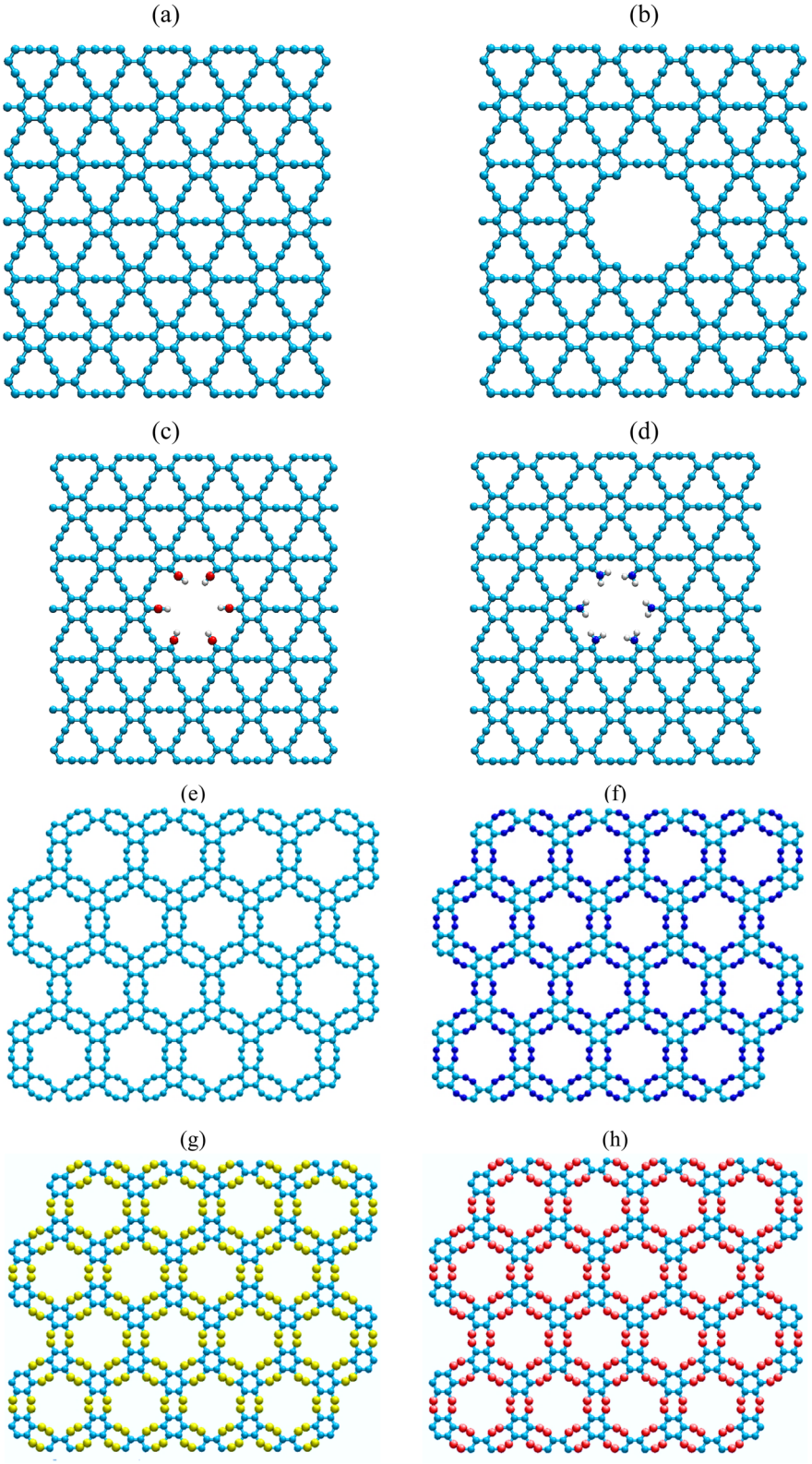

Fig. 12 Structures of γ-GY variants: (a) bare, (b) nanoporous, (c) –OH-functionalized nanoporous, (d) $-NH_2$-functionalized nanoporous, (e) bare HGY, (f) nitrogen-doped HGY, (g) silicon-doped HGY, and (h) boron-doped HGY.

scales in various applications. Therefore, MD simulation of continuous and spontaneous water molecule permeation *via* a single-layer γ-GY-3 membrane was investigated by Kou *et al.*[211] The authors reported that the γ-GY-3 membrane is more permeable to water molecules than (5,5) CNT membranes of equal pore diameter. The net water flux through the γ-GY-3 membrane is 27.5 ns^{-1}, compared to 13.5 ns^{-1} for the (5,5) CNT, despite their similar nanopore diameters. The remarkable hydraulic permeability of the γ-GY-3 membrane is mainly attributed to hydrogen bond formation, which connects the water molecules on both sides of the monolayer γ-GY-3 membrane and aids in overcoming nanopore resistance. As a result, a small single-file water structure will form, facilitating the rapid passage of water molecules across the γ-GY-3 membrane. Furthermore, a comparatively low energy barrier at the pore opening may account for the large net water flux. However, both the (10,0) and (9,0) CNTs demonstrated a higher water flux than the γ-GY-3 membrane. Lin and Buehler[212] explored a different strategy by utilizing a 2D nanoweb-like GY membrane for water purification and contaminant removal from both wastewater and seawater, employing MD simulations. GY membranes exhibited water permeability values ranging from 2.9 to 4.5 × 10^{-9} m Pa^{-1} s^{-1}, which initially increased with the number of acetylenic linkages. However, a decline in flow rate was observed when the linkage number reached 5 and 6. Additionally, the flow through the GTY membrane demonstrated optimal purification performance, ranging from 3.0 to 4.0 × 10^{-9} m Pa^{-1} s^{-1}, while maintaining excellent contaminant rejection under the applied hydrostatic pressures. The rejection rate for all contaminants is as follows: $CuSO_4$ > NaCl > CCl_4 > C_6H_6. Zhu *et al.*[213] studied the water desalination capability of the γ-GY-4 membrane. They also observed that there is a nonlinear relationship between water flux and membrane pore size; nonetheless, water flux rises linearly with pressure. Eventually, they concluded that γ-GY-4 outperformed GRA nanosheets for water desalination due to its high-water flow (*i.e.*, 10 times greater) and salt rejection.

In other work, Kou *et al.*[43] simulated the performance of γ-GY-3, γ-GY-4, and γ-GY-5 as membranes for water desalination. Their findings showed that γ-GY-3 had 100% salt rejection. Furthermore, γ-GY-4 nanosheet demonstrated superior salt rejection ability, with over 80% Na^+ rejection and close to 100% Cl^- rejection at 100 MPa pressures, which is an acceptable rate for salt rejection. This is attributed to the smaller pore size of γ-GY-4 when compared with the γ-GY-5 nanosheet. In addition, γ-GY-5 could not be employed as a membrane for water desalination due to its poor salt rejection. Progress has been achieved in utilizing GY membranes to study brine separation performance. Zhang and co-workers[214] explored the efficacy of single-layer GY-*n* allotropes (*i.e.*, n = 3, 4, 5, and 6) for water desalination by forward osmosis (FO). Their MD results show that γ-GY-3 performed better with high water flow (*i.e.*, 39.15 L cm^{-2} h^{-1}) and 100% salt rejection. Likewise, γ-GY-4, γ-GY-5, and γ-GY-6 membranes show comparable water fluxes slightly above or below that of γ-GY-3 but exhibit reduced salt rejection performance. The influence of membrane charge on water transport revealed that charged GY membranes consistently delivered higher water fluxes than their uncharged counterparts, indicating that charged GY-*n* (*i.e.*, n = 3, 4, 5, and 6) membranes offer enhanced performance for water transport in FO systems. In summary, the study indicates that γ-GY-3 offers superior performance for brine separation, whereas GY-*n* (*i.e.*, n = 4, 5, and 6) are suitable for applications where lower salt rejection is acceptable. In another research, Wu *et al.*[215] performed MD simulations to evaluate the effect of pristine γ-GY on water purification. They looked at the influence of positive and negative charges on water permeability and demonstrated that a GY membrane with a negative charge can increase both salt rejection and water permeability. Bagheri *et al.*[216] investigated water adsorption on the surfaces of GRA and GY nanosheets, demonstrating that GRA and GY-*n* (*i.e.*, n = 1 to 5) nanosheets had distinct wettability. Their findings revealed that the water layer between the water droplets and the membrane influences various aspects of the water droplets, such as the arrangement of water molecules in various layers, the number of hydrogen bonds, and parallel forces at the interface between the water molecules and the membrane.

Research on GYs extends beyond monolayer membranes, as noted in earlier studies, with investigations also exploring the water transport and desalination performance of bilayer GY membranes. Non-equilibrium MD simulations of water-salt solutions *via* single and double-layer GY membranes were explored by Akhavan *et al.*[217] This study revealed that the water flow rate through the γ-GY-4 membrane is double that of the γ-GY-3 membrane in both single- and double-layer membranes. GDY has been experimentally used to prepare filters on porous substrates for the capture of Pb^{2+} from an aqueous solution and showed high lead ion uptake.[218] Moreover, filter materials achieved efficiencies up to ~99.6%. According to Xue *et al.*[193] GDY was found to be impermeable to both water and ions even under a pressure of 250 MPa, rendering it unsuitable for desalination applications. However, Baghbani *et al.*[219] designed a pristine GDY nanosheet to study the salt rejection. The results showed that the GDY membrane exhibits 100% salt rejection at pressures. The structure of pristine GDY nanosheets contains inherent pores with optimum width for separating salt ions from aqueous solutions. This membrane shows a water permeability of 565.37 L m^{-2} h^{-1} bar^{-1} at 400 MPa and a salt rejection rate of 99.41%. The water permeability of pristine GDY observed in this study is comparable with that of other membranes, such as polymeric seawater RO with 1.87 L m^{-2} h^{-1} bar^{-1}, brackish RO with 4.58 L m^{-2} h^{-1} bar^{-1}, nanofiltration with 14.58 L m^{-2} h^{-1} bar^{-1}, high-flux RO with 27.08 L m^{-2} h^{-1} bar^{-1},[220] functionalized GRA with 255.41 L m^{-2} h^{-1} bar^{-1},[221] and functionalized graphene oxide (GO) with 409.16 L m^{-2} h^{-1} bar^{-1}.[222] The aforementioned data demonstrate that pristine GDY is a highly efficient membrane for water desalination compared to other membranes due to its superior water permeability and salt rejection. However, better water permeability has been reported in other systems like CNTs,[223] but when the pristine GDY was utilised as a membrane, there was no need to produce pores within the membrane for water desalination. This is a significant advantage over other single-

Table 4 Effects of pore sizes and functional groups on the GY-based membrane separation process

Membrane	Metal ion	Pore size (diameter)	Pore functionalization	Pressure	Ref.
α-GY, β-GY, GDY, γ-GY-3, γ-GY-4	Na^+, Cl^-, Mg^{2+}, K^+, Ca^{2+}	Pore radius α-GY-1.746 Å, β-GY-1.773 Å, GDY-1.002 Å, γ-GY-3-1.736 Å, γ-GY-4-2.470 Å	Pristine	0 to 250 MPa	193
γ-GY-3	Na^+, Cl^-	γ-GY-3-0.69 nm	Pristine	0 to 600 MPa	211
γ-GY-3, γ-GY-4, γ-GY-5, γ-GY-6	NaCl, $CuSO_4$, C_6H_6, CCl_4	γ-GY-3-3.8 Å, γ-GY-4-5.4 Å, γ-GY-5-7.0 Å, γ-GY-6-8.6 Å	Pristine	50 MPa	212
γ-GY-3/-4/-5/-6	Na^+, Cl^-	—	Pristine	100–500 MPa	213
γ-GY-3/-4/-5	Na^+, Cl^-	γ-GY-3-0.69 nm	Pristine	0 to 350 MPa	43
γ-GY-3, γ-GY-4, γ-GY-5, γ-GY-6	Na^+, Cl^-	γ-GY-3-3.8 Å, γ-GY-4-5.4 Å, γ-GY-5-7.0 Å, γ-GY-6-8.6 Å	Pristine	—	214
γ-GY-3/-4/-5	Na^+, Cl^-	γ-GY-3-0.69 nm	Pristine/charged	0 to 150 MPa	215
Bilayer γ-GY-3/-4	Na^+, Cl^-	γ-GY-3-3.8 Å, γ-GY-4-5.4 Å	Pristine	50 to 200 MPa	217
α-GY, γ-GY-2/-3/-4	Na^+, Cl^-	Pore area Pristine: α-GY-29.91 $Å^2$, γ-2-GY-25.15 $Å^2$, γ-3-GY-45.57 $Å^2$, γ-4-GY-71.89 $Å^2$ Hydrogenated: α-GY-20.48 $Å^2$, γ-2-GY-15.72 $Å^2$, γ-3-GY-35.31 $Å^2$, γ-4-GY-59.90 $Å^2$	Pristine, hydrogenated	0 to 1000 MPa	225
γ-GY-3, γ-GY-4, γ-GY-5	Na^+, Cl^-	γ-GY-3-69 Å, γ-GY-4-8.45 Å, γ-GY-5-9.92 Å	Pristine, hydrogen (–H), fluorine (–F), carboxyl ($–COO^-$), amine ($–NH_3^+$)	100 to 200 MPa	42
γ-GY-1	Na^+, Cl^-	Pore area 12.25 $Å^2$ to 26.09 $Å^2$	Hydroxyl (–OH), fluorine (–F), carboxylic acids (–COOH)	0 to 50 MPa	209
GDY	Na^+, Cl^-	—	Pristine	150 to 600 MPa	219
ANGMs, γ-GY membranes (γ-GY-3/-4/-5)	Na^+, Cl^-	Pore area ANGM-1-10 $Å^2$, ANGM-2-19.18 $Å^2$ ANGM-3-27.6 $Å^2$, ANGM-4-37.61 $Å^2$ γ-GY-3-16.88 $Å^2$, γ-GY-4-34.03 $Å^2$, γ-GY-5-55.6 $Å^2$	Hydrogen (–H), pristine	50 to 250 MPa	227
Graphenylene	Na^+, Cl^-	Pore area Pristine-49.24 $Å^2$, P1-35.94 $Å^2$, P2-33.04 $Å^2$, P3-22.94 $Å^2$, P4-28.20 $Å^2$	Pristine, P1-fluorinated (–F), P2-hydrogenated (–H), P3-combined fluorinated and hydroxylated (–F and –OH), P4-combined fluorinated and hydrogenated (–F and –H)	5 to 100 MPa	226

layer membranes including GRA, boron nitride, and silicon carbide membranes.

Since nitrate ions pose a risk to the ecosystem, it is vitally important to remove them from water. In order to achieve this, Majidi and co-workers[224] preferred to employ a pristine nanoporous GDY sheet with a pore density of 2.4×10^{18} pores per m^2 and an incircle radius of 2.8 Å. Water naturally moves through the GDY nanopores, and the two-hydrogen-bond transient structure activates the migration of water molecules through the pores, serving as a transition state. GDY can function as a good membrane for nitrate separation, as evidenced by its high-water permeability of 6.19 L per day per cm^2 per MPa with 100% nitrate ion rejection. The membrane's hydrophobicity aided in high water flux by accelerating water flow because there was no attraction connection between the water and the membrane after it passed through the holes.

The γ-GY-1 membrane with functional groups was not employed in any of the aforementioned research studies. In practical water desalination and contaminated wastewater treatment, bare GYs often become functionalized by protons or hydroxyl radicals found in the water. Hence, studying functionalization is essential for the potential application of GY in seawater desalination. Raju *et al.*[225] evaluated the performance of both bare and hydrogenated α-GY and γ-GY membranes in desalination as a function of pore geometry, pore size, chemical functionalization, and applied pressure. The MD simulation demonstrated that γ-GY, H γ-3-GY, α-GY, and H α-GY membranes can reject more than 90% of salt ions while allowing higher water fluxes. Water permeability can reach 85 L per cm^2 per day per MPa, which is three times higher than commercial seawater RO membranes and ten times higher than nanoporous GRA. As a result, they appear to be promising candidates for the desalination process among the membranes studied. Moreover, the scientists found that hexagonal pores with conical water flow (α-GY) have a higher water flux per unit accessible area than triangular pores. In another work, pristine GY-*n* (*i.e.*, $n = 3$, 4, and 5) membranes were modified for water desalination using chemical functionalities such as hydrogen, F, carboxyl, and amine by Mehrdad and co-workers.[42] According to their findings, γ-GY-3 and γ-GY-4 membranes function well in the desalination process. The effects of pore sizes and functionalizations on the GY-based membrane separation process are shown in Table 4.

The recent MD study conducted by Azamat *et al.*[209] explored the performance of functionalized (*i.e.*, –OH, –F, and –COOH) γ-GY-1 nanosheet for the RO water desalination process. In their work, each pore with various functional groups has a distinct pore size that affects the water permeability. Although the –OH-functionalized membrane exhibited a greater permeability (*i.e.*, 8953 L m^{-2} h^{-1} bar^{-1}), salt removal was minimal in this system, especially at high hydrostatic pressures. The –OH group, being a hydrophilic group, creates more hydrogen bonds with water molecules than other systems, allowing more water molecules to pass through the pore and enhance the flow. On the contrary, using –COOH-functionalized γ-GY-1 resulted in complete salt rejection and minimal water permeability (*i.e.*, 4235 L m^{-2} h^{-1} bar^{-1}). The low water permeability is mainly attributed to the large size of the –COOH group and reduced pore size. The water permeability of the –OH-functionalized system was over 2.11 times more than that of –COOH-functionalized γ-GY-1.

Majidi *et al.*[32] explored the permeation of heavy metal ions such as Hg^{2+} and Cu^{2+} across the functionalized pore of γ-GY-1 nanosheets under an external electric field. The effects of two different hydrophilic functional groups (*i.e.*, –COOH and $–NH_2$) were investigated by passivating at the pore edge. The $–NH_2$- and –COOH-functionalized pores had effective pore sizes of 4.45 Å and 3.95 Å, respectively, making them suitable for the permeation of Cu^{2+} and Hg^{2+} with atomic diameters of 2.56 Å and 3.42 Å, respectively. The authors found that the electrostatic interaction between ions with the $–NH_2$ group is higher than that of the –COOH pore, hence the $–NH_2$ pore allowed more ions to pass through under all applied electric fields. Notably, $–NH_2$-functionalized γ-GY-1 outperforms –COOH-functionalized γ-GY-1 in separating Cu^{2+} ions. However, Hg^{2+} ions encounter a high energy barrier when passing through the membrane, particularly in the –COOH-functionalized pore, due to their larger ionic radius and the smaller pore size of the membrane.

Balaban and Vollhardt introduced the graphenylene structure.[49] In recent times, graphenylene has received a lot of interest for its pore structure and thermodynamic stability. It has been employed as a membrane to separate gases, but not to desalinate water.[50] Thus, Jahangirzadeh and co-workers[226] made an effort to investigate the capability of functionalized graphenylene membranes for water desalination in terms of water permeability and salt rejection by considering four different membrane-based systems (P1, P2, P3, and P4) under various external pressures. The results showed that system P1 with fluorinated pore had the greatest performance among all systems, with a permeability of 11 032 L m^{-2} h^{-1} bar^{-1} and 99.4% salt rejection at $P = 10$ MPa. Similarly, system P3 with combined functional (*i.e.*, –F and –OH) groups at the pore had a permeability of 9293 L m^{-2} h^{-1} bar^{-1} and 100% salt rejection at $P = 5$ MPa. Although system P3, functionalized with both –F and –OH groups, exhibits greater hydrophilicity than the fluorine-functionalized P1 membrane, its permeability is lower. This reduction arises from the smaller effective pore area of P3 relative to that of P1. As a result, P1 and P3 systems can serve as effective solutions for desalination.

An innovative approach to efficient water desalination employing GY membranes was introduced. Nematipour *et al.*[227] proposed anisotropically nanoporous GY membranes (*i.e.*, ANGMs, $n = 1$, 2, 3, and 4) for water desalination and also compared its ion rejection and permeability with different γ-GY membranes (*i.e.*, $n = 3$, 4, and 5). These membranes were fabricated by synthesizing nanosheets through the meta-bromination of the same molecule. During the process, the pore size of an ANGM can be controlled to remain below 1 nm by adjusting the number of triple bonds between two phenyl rings. The findings revealed that ANGMs show high permeability (*i.e.*, 7.98–47.14 L per cm^2 per day per MPa) and enhanced ion rejection. The permeability of the proposed membrane is 2–3 orders of magnitude greater than that of the RO membrane. This is mostly owing to the existence of well-engineered nanopore morphologies. In particular, ANGM-2

and ANGM-3 membranes have the maximum water permeability and complete ion rejection. As a result, using these membranes will be more suitable and cost-effective than other membranes. Recently, HsGDY achieved a very high adsorption capacity (~2390 mg g^{-1}) for Pb^{2+}, significantly outperforming GDY.[228] It effectively treated large volumes and removed Pb^{2+} from biological fluids such as blood with higher efficiency than GDY. Another study, a functionalized GDYO-3M membrane was experimentally fabricated and tested for the removal of Hg^{2+} from water.[229] The membrane achieved >97% removal efficiency for 0.1 mg per L Hg^{2+} from >10 L of water within 1 h.

Catalyst

GY and its derivatives constitute a versatile platform for single-atom catalysts (SACs) because their mixed sp–sp^2 carbon lattice combines high surface area, tunable electronic structure, and sites that can strongly bind metal atoms, all of which favour high dispersion and suppressed aggregation of single metal atoms.[230] By contrast, pristine GRA is a poor SAC support: low diffusion barriers for metal adatoms (*i.e.*, ≈0.2–0.8 eV) allow rapid surface mobility and clustering, undermining single-atom stability.[231] GY's higher metal–substrate binding and larger diffusion barriers, therefore, play a decisive role in immobilizing single atoms and preserving uniform active-site distributions, which is a necessary precondition for the intrinsic advantages of SACs (maximal atom utilization and well-defined active centers).

A wide range of first-principles studies show that GY-supported SACs are active across many electrocatalytic reactions. Representative examples include Fe@GY for the alkaline ORR,[232] Fe@GY catalysing CO oxidation *via* an Eley–Rideal pathway with a low barrier of 0.21 eV,[233] and Ru-decorated GY proceeding through a two-step CO oxidation route with the highest barrier of ≈0.7 eV.[234] Boron-doped GY supporting single Co atoms (Co@B1-GY and Co@B2-GY) reached near-thermoneutral hydrogen adsorption ($\Delta G \approx -0.004$ eV for Co@B2-GY), highlighting exceptional HER activity, while N-doped variants (*e.g.*, Co@N1-GY) improve stability and surface charge density to furnish additional active sites for water-splitting electrocatalysis.[235,236] Beyond HER, Cr-doped GY was identified for CO_2 reduction (CO_2RR),[237] and Ni@V-c-GY shows highly selective H_2O_2 generation with a very low $2e^-$ ORR overpotential (0.03 V).[238] Pyrazine functionalization of GY (TM@pyGY) further demonstrates that transition-metal anchoring (Co, Ni, Cu, Mn, Fe, Ru, Pt, Rh, Pd, and Ir) can produce bifunctional/trifunctional behaviour (HER/OER/ORR), with Pd@pyGY and Ni@pyGY among the most versatile examples.[239]

Transition metals such as Fe, Co, Ni, and Cu anchored on GY have been studied for direct methane-to-methanol conversion, where Co–O-functionalized GY mimicked enzymatic methane oxidation with high activity and selectivity.[240] Ullah *et al.*[241] identified Ni-GY as highly stable and catalytically active for the HER ($\Delta G_{H^*} = 0.08$ eV). Heteroatom-doped GY (N, B, S, P, and O) further enhances the electrocatalytic performance; sp-hybridized B doping, alone or in combination with sp^2-B, significantly improves the nitrogen reduction reaction (NRR) activity, achieving limiting potentials as low as 0.12 V.[242] Systematic DFT and CoDOSA framework studies demonstrated the multifunctionality of SACs on doped GY substrates. Co@GY and Ni@3B-GY were identified as robust trifunctional catalysts for the ORR, HER, and OER, with AIMD simulations confirming stability at 400 K.[243] Nitrogen-doped GY synthesized *via* mechanochemical methods also facilitated photosynthetic H_2O_2 production with 74% selectivity and rates of 7.47 mmol h^{-1} g^{-1}.[244] Li *et al.*[245] conducted extensive DFT screening of 26 transition metals embedded in γ-GY, revealing Co, Rh, Fe, Ir, Cu, Pd, Ni, and Pt as effective unifunctional and bifunctional electrocatalysts for the ORR/OER. Multifunctional electrocatalytic activity of metals anchored on square GY (TM@S-GY) was further demonstrated, with Ni@S-GY showing trifunctional activity (HER, OER, and ORR) and Pt@S-GY, Ir@S-GY, and Pd@S-GY exhibiting strong bifunctional performance.[246] TM-doped γ-GY-like BN sheets (M/γBN) also displayed promising activity for the NRR, with V/γBN showing the lowest energy barrier *via* the distal mechanism.[247] The enhanced performance of V/γBN was attributed to an electron donation–back-donation effect, which also suppressed the competing HER activity. Additionally, incorporating Hubbard U corrections revealed a clear correlation between the adsorption energy and the bond distance. Single-atom electrocatalysts have also been applied for nitrogen reduction reactions (NRRs). Song *et al.*[248] developed noble-metal (Rh, Ru, Ir, Os, Pd, and Pt) single atoms anchored on N-, B-, and O-doped GY (NMX@GY), with B- and O-doped GY showing higher N_2 adsorption affinity. OsB@GY and RuB@GY were identified as the most effective catalysts, with Bader charge analysis indicating significant electron transfer to the adsorbed N_2, facilitating activation and reduction.

First-principles investigations by Talib *et al.*[249] on single-transition-metal atoms (STM1 = Sc–Au) anchored in GY H1 cavities confirmed structural stability *via* AIMD and phonon analysis. Sc1, Co1, Fe1, and Au1/GY exhibited efficient HER *via* the Volmer–Heyrovsky pathway, with Sc1 and Au1/GY outperforming others. Co1/GY showed excellent OER activity (0.46 V overpotential), while Rh1 and Co1/GY achieved low ORR overpotentials (0.36 V and 0.46 V). GY-supported SACs have also shown promise for selective CO_2 reduction.

Liu *et al.*[250] demonstrated that tensile-strain regulation enhances $2e^-$ CO_2RR selectivity over Co-GY by suppressing the competing HER. Constant-potential calculations and constrained AIMD confirmed the stability and high CO_2RR activity of Co-GY, where the tensile strain preferentially affected *COOH adsorption relative to *H, improving CO selectivity. The effect of heteroatom doping on oxygen electrocatalysis was further elucidated by Shao and Shao,[251] who studied N-doped TM-embedded GY SACs. N_0–Co-GY exhibited the highest ORR activity in both acidic and alkaline media, illustrating how heteroatom engineering tunes the electronic structure and intermediate adsorption. High-throughput DFT screening of 30 TM-anchored GY monolayers (Cr–Zn and Mo–Ag) by Ye *et al.*[252] highlighted that the catalytic performance depends on the interaction strength between intermediates and TM centers,

with d-band center tuning mitigating excessively strong adsorption. Fe-GY and Mn-GY showed the best performance, achieving low overpotentials of 0.42 V and 0.59 V while retaining high thermodynamic and electrochemical stability.

Moving beyond single atoms, multi-atom clusters and triple-atom catalysts expand the product scope (*e.g.*, C_1 products in CO_2RR). Triple-atom-doped systems (3Fe-GY, 3Cu-GY, 3Co-GY) show promising limiting potentials and product selectivity trends (3Cu-GY favouring CH_4 and 3Cu- and 3Fe-GY favouring CH_3OH), demonstrating that controlled sub-nanoscale ensembles on GY lattices can access reaction channels inaccessible to isolated SACs.[253] GDY and HGY variants similarly extend functionality: GDY integration with TiO_2 promotes interfacial charge transfer and suppresses recombination for improved photocatalysis;[254] Au single atoms on GDY favour acetylene hydrochlorination pathways with the Langmuir–Hinshelwood route showing lower barriers than Eley–Rideal;[255] and transition-metal three-atom single-cluster catalysts on GDY have been proposed as stable, high-activity alternatives to SACs.[256] HGY- and GDY-supported TM anchors achieve near-Pt HER benchmarks in certain cases (*e.g.*, Cr@HGY $\Delta G_H \approx -0.05$ eV, AIMD stable at 300–333 K) and exhibit appealing thermoelectric/catalytic multifunctionality under strain or with non-metal dopants.[257–260]

GY derivatives with specialized lattice topologies also display exceptional HER performance. Motaghi and Mohammadi-Manesh[261] found cobalt-anchored 6,6,12-GY to be thermodynamically stable with $\Delta G_{H^*} = 0.042$ eV, while Jafari and Reisi-Vanani[262] reported Co- and Ni-decorated 8-16-4 GY as low-cost dual-function electrocatalysts, achieving ΔG_{H^*} values of 0.03–0.09 eV and overpotentials of 0.42–0.72 V for overall water splitting. These findings collectively highlight that transition metal anchoring, heteroatom doping, and lattice engineering synergistically govern catalytic performance, enabling GY-based materials to serve as high-efficiency, stable, and multifunctional electrocatalysts for the HER and water splitting. GY-based nanostructures, including γ-, α-, and β-GY and GDY nanoribbons, have emerged as promising platforms for both single-atom and sub-nanoscale cluster electrocatalysts. Xu *et al.*[263] demonstrated that sub-nanoscale Pt_4 clusters on γ-GY exhibit strong binding due to optimal Pt–Pt/Pt–C bond length ratios, achieving CO oxidation activity comparable to Pt SACs, highlighting the potential of metal clusters on GY surfaces. For the ORR in acidic fuel cells, α-GY shows enhanced activity due to positively charged carbon sites that favor O_2 and OOH^+ adsorption, creating active catalytic centers.[264]

Beyond metal-supported systems, metal-free GY nanoribbons have shown notable bifunctional activities for the HER and ORR. Lv *et al.*[265] combined DFT and machine learning to investigate β-GY and β-GDY nanoribbons (βGyNRs/βGDyNRs), showing that edge engineering and N-doping significantly enhance catalytic performance. In γ-GY nanoribbons, only pristine zigzag configurations without benzene terminations exhibited intrinsic activity, while others remained inactive. Introducing single nitrogen dopants revealed that sp^2-N doping was more effective than sp-N, with catalytic efficiency decreasing as the doping depth increased, resulting in several N-doped γGYNRs serving as efficient bifunctional electrocatalysts.[266] Similarly, GDY nanoribbons were shown to possess edge-specific active sites for bifunctional catalysis. Lv *et al.*[267] reported that zigzag GDY NRs without benzene terminations display excellent HER and ORR activity, primarily at acetylenic linkages at the edges. Strategic N-doping further enhanced performance, with N1 doping at inner sites and N2 near edges effectively improving catalytic efficiency, while other dopant positions had negligible effects. The study highlighted the ΔE_H descriptor (optimal range: −0.474 to −0.119 eV) as critical for bifunctional HER/ORR performance, confirming that appropriately engineered GDY NRs can act as high-efficiency, metal-free bifunctional electrocatalysts.

Recent advances in metal-free and heteroatom-doped GDY/GY nanostructures highlight their multifunctional electrocatalytic and energy storage potential: metal-free TAGDY shows durable acidic-media HER activity by facilitating rapid proton–electron transfer;[268] GDY–GRA heterostructures with TM decoration tune Li–S battery chemistry through controlled LiPS binding and SRR catalysis;[269] TH-GY is proposed as a mechanically robust, optically active 2D allotrope with potential electronic and catalytic uses;[120] and dual-atom or small cluster motifs (*e.g.*, Mo–Ni DACs, Si-doped BN-GY analogues, Ca-doped γ-GY) open pathways for the enhanced HER, N_2O reduction and electronic property tuning for catalysis, storage and device applications.[270–272]

Ultrathin GDY-supported zero-valent palladium (Pd^0/GDY) was experimentally prepared and used as an HER cathode. Pd^0/GDY showed very low overpotential (*i.e.*,∼55 mV at 10 mA cm^{-2}) and higher mass activity than Pt/C, with robust stability.[273] Liu *et al.*[274] synthesized GDY nanotubes and nitrogen-doped graphdiyne (NGDY) nanotubes and demonstrated their activity as metal-free electrocatalysts for the ORR, with NGDY showing enhanced onset potential and faster kinetics. Wang and Jin[275] constructed a CuI-GDY/ZnAl-LDH S-scheme heterojunction that exhibited enhanced photocatalytic H_2 production by efficient charge separation across GDY-based interfaces. Li *et al.*[276] demonstrated a GDY-modified In_2O_3 nanocomposite for photocatalytic CO_2 hydrogenation, showing significantly improved formation of C_2^+ hydrocarbons by enhancing photogenerated charge separation and reducing kinetic barriers in photocatalysis. Zheng *et al.*[277] reported GDY grown with vanadium–iridium oxide ($VIrO_x$) quantum dots forming well-defined interfaces that acted as a highly active OER catalyst with low overpotential and excellent long-term stability in alkaline electrolytes. Studies have shown that GDY integrated with metal oxides or semiconductor supports enhances the catalytic performance (*e.g.*, improved hydrogen evolution and pollutant degradation) by improving charge separation and providing active sites.[278]

Taken together, the literature converges on several key, actionable insights: (i) GY-type lattices provide intrinsic binding sites and electronic tunability that stabilise single atoms and small clusters while suppressing aggregation; (ii) heteroatom doping, strain, and topology act as orthogonal levers to tune adsorption energetics, selectivity (*i.e.*, CO_2RR *vs.* HER), and multifunctionality; and (iii) high-throughput DFT, AIMD, and

descriptor-driven screenings reliably identify promising candidates but must be complemented by targeted experimental validation to translate predicted activity and stability into practical electrocatalysts. These principles position GY and its derivatives as a fertile design space for next-generation SACs and sub-nanoscale electrocatalysts across energy conversion and storage applications.

Materials for ion batteries

An ideal anode material should provide both high ion mobility and large storage capacity.[35] Theoretical studies suggest that GBMs meet these requirements due to their intrinsic porous frameworks. For instance, bulk GY enables 3D lithium diffusion with relatively low energy barriers (*i.e.*, 0.53–0.57 eV), compared to GRA where out-of-plane Li migration is strongly restricted by barriers >8 eV.[279,280] Consequently, GY exhibits superior Li mobility and higher theoretical storage capacity (LiC_4) than graphite (LiC_6).

GDY follows a similar trend, combining high capacity (LiC_3) with moderate diffusion barriers (*i.e.*, 0.18–0.84 eV).[281] First-principles calculations show that the triangular pores of GDY can host three Li atoms per pore at symmetric sites, forming an alternating occupation pattern across both surfaces of a monolayer. This facilitates uniform Li distribution, with in-plane diffusion (*i.e.*, 0.52 eV) and through-plane penetration (*i.e.*, 0.35 eV), both energetically favorable. Such dual mobility pathways enable GDY to achieve a maximum capacity of LiC_3, double that of graphite, while ensuring fast ion transport.[282] Together, the high diffusion kinetics and large storage capacity of GY and GDY highlight their potential as next-generation anode materials.

Boron doping and structural engineering strategies significantly enhance the electrochemical potential of GBMs for ion batteries. Boron-doped GY exhibits improved Li binding with a capacity of ~1130 mAh g^{-1},[283] while multilayer α-GY and GY intercalated with Li achieve volumetric capacities up to 1589 mAh cm^{-3}, far surpassing graphite.[284] Beyond lithium, both GY and GDY support efficient Na-ion storage through low in-plane diffusion barriers (*i.e.*, ~0.4 eV).[25] Emerging 2D carbon ene-yne has been predicted to deliver ultrahigh theoretical capacities (*i.e.*, 2680 mAh g^{-1} for Li, 1788 mAh g^{-1} for Na), surpassing most known 2D anodes.[285]

External modulation offers further improvements. Strain engineering on GY enhances Li adsorption, lowers diffusion barriers, and raises capacity to 2233 mAh g^{-1} under 12% biaxial strain, with favorable operating voltages (*i.e.*, 0.50 V).[286] Similarly, curvature effects in γ-GY nanotubes enable orbital rearrangement, boosting capacity up to 2232 mAh g^{-1} for C_6Li_6, while also improving the Li mobility.[287] B-GY offers balanced performance, with a high capacity of 525 mAh g^{-1}, moderate voltages (*i.e.*, ~0.73 V), and good diffusion kinetics.[288] Mechanical studies indicate that α-GY, though softer, provides greater strain tolerance, while γ-GY offers higher modulus and fracture stress; a 10% strain threshold was identified as the safe limit for enhancing storage without structural failure.[289] Functional group substitution further tailors electrochemical properties, with nitro- and carbonyl-modified GYs reaching redox potentials up to 4.1 V, outperforming GRA analogues.[290] Finally, α-GY nanotubes also show enhanced Li uptake (*i.e.*, 1273 mAh g^{-1} for C_4Li_4), with curvature promoting efficient adsorption and diffusion.[291] Collectively, these studies emphasize that doping, strain engineering, nanotube formation, and functionalization provide powerful routes to maximize the ion storage capacity and stability of GY derivatives. However, most capacities remain theoretical; challenges such as large-scale synthesis, electrode integration, and cycling durability must be addressed before their translation into practical ion batteries.

Recent computational studies highlight the versatility of GY-based materials (GYs, GDYs, and derivatives) as high-capacity anodes across a range of ion batteries. For Na-ion systems, layered GDY demonstrated stable Na intercalation up to $x = 0.61$ (*i.e.*, 1237 mAh g^{-1}), nearly 35 times the capacity of graphite, while α-GY achieved an even higher theoretical capacity of 1396 mAh g^{-1} with optimal OCV (0.81 V) and low diffusion barriers (*i.e.*, 0.18–0.96 eV).[292,293] Similarly, T4,4,4-GY exhibited exceptional Na mobility with a semiconductor-to-metal transition upon adsorption.[294] PG-yne extended this trend, it can host up to eight Li/Na ions, delivering a theoretical capacity of 680 mAh g^{-1}, with low diffusion barriers (*i.e.*, ≤0.50 eV), low open-circuit voltages, and enhanced electronic conductivity, surpassing many conventional 2D anodes, particularly for Na-ion systems.[28] For multivalent systems, boron–nitrogen-substituted GY (BN-yne) outperforms pristine GY for Ca-ion batteries, offering lower migration barriers (*i.e.*, 4.3 *vs.* 5.9 kcal mol^{-1}) and higher diffusion coefficients, indicative of faster charge/discharge kinetics.[295] similarly, 3D porous phosphorus-GDY (3D-PGDY) exhibits ultrahigh specific capacities of 1064.56 mAh g^{-1} (K) and 2129.12 mAh g^{-1} (Ca) with minimal diffusion barriers and negligible volume expansion, highlighting the advantages of 3D architectures and sp-hybridized frameworks for multivalent ion storage.[296] HGY demonstrates exceptional performance for K-ion batteries, balancing high capacity (*i.e.*, 651 mAh g^{-1}), moderate volume expansion, and good ionic conductivity, though lower structural stability can limit ion mobility; hybridization with more robust materials like GRA is suggested to optimize diffusivity for broader metal-ion battery applications.[26]

GY derivatives have emerged as promising cathode and anode materials for advanced metal-ion batteries, exhibiting high capacity, structural stability, and efficient ion transport. GDY has been proposed as an effective cathode for aluminum dual-ion batteries (ADIBs), with DFT and AIMD studies demonstrating rapid $AlCl_4^-$ diffusion, thermodynamic stability, and a high theoretical specific capacity of 186 mAh g^{-1}, about three times that of graphite, alongside strong cyclic durability.[297] Further investigations of α- and γ-GY as Al-ion battery cathodes reveal ample adsorption sites for $AlCl_4^-$, high open-circuit voltages (*i.e.*, 2.18–2.22 V), and excellent structural resilience, with α-GY exhibiting minimal volume expansion (186%) and extremely low expansion energy (*i.e.*, ~0.003 eV $Å^{-2}$), favoring reversibility and cycling stability.[298]

For anode applications, 3D porous PGY structures and sandwich GRA/PGY/GRA architectures facilitate multivalent ion storage

with low migration barriers and high thermal/mechanical stability. Li ions can traverse multiple pathways, whereas larger Na and K ions migrate through larger pores, yielding energy barriers of 0.18–0.43 eV in 3D-PGY, which further reduced to 0.12–0.37 eV in the sandwich configuration. These materials deliver theoretical specific capacities up to 558 mAh g^{-1} with favorable open-circuit voltages, highlighting the versatility of GY-based architectures for Li-, Na-, and K-ion battery anodes.[29]

A free-standing HsGDY film was experimentally synthesized *via* an *in situ* coupling reaction and used as a flexible anode for lithium-ion and sodium-ion batteries.[299] The HsGDY electrode delivered large reversible capacities (~1050 mAh g^{-1} for Li-ion and ~650 mAh g^{-1} for Na-ion) at 100 mA g^{-1}, along with good rate performance and cycling stability, attributed to its porous π-conjugated structure and facilitated ion transport. GDY/exfoliated graphene (EG) composite electrodes prepared by solvothermal methods were applied in Li-ion cells.[300] The composite showed a reversible capacity of ~1253 mAh g^{-1} after 600 cycles at 0.5 A g^{-1}, and maintained ~324 mAh g^{-1} after 2000 cycles at 5 A g^{-1}, attributed to enhanced conductivity. GDY was experimentally integrated with GRA in a GDY/Gr/GDY sandwich structure and tested as an anode for potassium-ion batteries.[301] This composite electrode showed enhanced capacity, rate capability, and cycling stability compared to bare GDY, demonstrating practical potassium storage performance.

Three-dimensional porous HsGDY was prepared *via* an interface-assisted synthesis and used as an anode in LIBs.[302] The electrode exhibited large reversible capacity (*i.e.*, ~930 mAh g^{-1} after 100 cycles at 1 A g^{-1}), excellent cycling (*i.e.*, ~720 mAh g^{-1} after 300 cycles), and good rate capability, *via* expanded interlayer spacing and enhanced ion accessibility. HsGDY has been experimentally investigated as a cathode additive or interlayer in lithium–sulfur (Li–S) batteries to mitigate the polysulfide shuttle and improve performance.[303] Heat-treated HsGDY showed enhanced sulfur trapping and improved cycle life, though the mechanism was linked to structural changes rather than direct chemical interaction during cycling. HsGDY aerogel was used as a host for molten Li metal to fabricate composite Li@HsGDY anodes, where the hierarchical pore structure and lithiophilic nature enabled improved lithium-ion transport and suppression of dendrite formation.[304] A composite of tin dioxide with GDY (SnO_2/GDY-400) was synthesized and applied as an anode in both lithium-ion and sodium-ion batteries.[305] The high conductivity of GDY mitigated SnO_2 agglomeration and volume expansion, resulting in excellent specific capacities (*i.e.*, ~1478 mAh g^{-1} in LIBs) and high capacity retention over long cycling. Collectively, these studies underscore the tunability of GBMs for both cathode and anode applications, combining high capacity, ion mobility, and structural resilience, making them strong candidates for next-generation rechargeable metal-ion batteries.

Gas separation

GY-based materials possess acetylenic linkages that generate intrinsic, tunable pores, enabling molecular sieving without additional pore engineering. This structural advantage allows small molecules such as H_2 to permeate through low-energy barriers, while larger gases like CH_4 encounter strong resistance. Their mechanical robustness and flexibility further support their use as stable separation membranes. In contrast, GRA suffers from intrinsically undersized carbon rings, requiring artificial nanopore introduction that complicates fabrication and compromises integrity.[306,307]

Computational studies have highlighted the remarkable selectivity of GBMs. For instance, defect-free hydrogenated α-GY achieved complete H_2/CH_4 separation with H_2/N_2 selectivity of ~700, although performance diminished at higher temperatures and in the presence of defects.[308] Functionalization strategies (*i.e.*, –OH, –F) were shown to enhance CH_4/H_2S separation, particularly at zero applied pressure, emphasizing the role of edge chemistry in tuning selectivity.[309] Similarly, among the γ-C_4X (*i.e.*, X = O, S, and Se) family, γ-C_4O was predicted to be structurally stable with extremely high H_2/CH_4 selectivity (*i.e.*, 10^{19}), though such idealized values may be difficult to replicate experimentally.[310] Hybrid designs, such as GY-based mixed matrix membranes (GY-polypyrrole), demonstrated adsorption selectivity (*i.e.*, $H_2O > CO_2 > O_2$) and optimal O_2 diffusion at ~15% filler loading, underscoring the delicate balance between permeability and filler dispersion.[311] Notably, γ-GY-3 showed extraordinary H_2 permeance (~10^7 GPU) while excluding larger hydrocarbons like C_2H_6, outperforming both GRA and other 2D membranes.[312] Despite these promising predictions, the exceptional selectivity and permeance of GBMs largely stem from idealized MD and DFT models, with performance highly sensitive to defects, pore chemistry, and operating conditions. Bridging this simulation-experiment gap remains the key challenge, particularly in synthesizing large-area, defect-controlled GY membranes and validating their separation efficiency under realistic mixed-gas feeds.

GDY has emerged as a promising membrane for H_2 extraction from syngas due to its intrinsic triangular pores, which offer size- and energy-dependent selectivity. Computational studies reveal that H_2 faces very low permeation barriers (*i.e.*, ~0.1 eV), while CO and CH_4 encounter significantly higher resistances (*i.e.*, 0.33 eV and 0.72 eV, respectively).[313] Importantly, selectivity can be tuned through pore size engineering, with permeation barriers decreasing exponentially with the increase in pore diameter.[314] Temperature and pressure exert strong influences: H_2 flux rises with temperature (*i.e.*, 7.3 to 9.4 g cm^{-2} s^{-1} between 300 and 500 K), whereas CO and CH_4 require extreme thermal or pressure conditions (*i.e.*, >1100 K or ~200 MPa) to penetrate, confirming GDY's intrinsic molecular sieving capability.[315] Electrostatic tuning further enhances selectivity, as positive charging increases diffusion barriers for CO and CH_4, yielding up to 100-fold improvements in H_2/CO separation.[316]

Beyond syngas purification, GDY shows chemical robustness (*i.e.*, oxidation barrier ~1.97 eV) and versatile separation potential. Meng *et al.*[317] demonstrated its strong O_2 selectivity against toxic gases (*i.e.*, Cl_2, HCN, SO_2, and H_2S), while engineered structures such as dumbbell-shaped GYs[318] and rhombic-GY[314] expand the design space for tailored gas sieving. Chemical modification also plays a decisive role: GDY-F and GDY-O achieved efficient $CO_2/N_2/CH_4$ separation, with GDY-O

highly selective for CO_2/N_2 below 300 K.[319] Zhou *et al.*[320] fabricated suspended GDY membranes over micrometer-scale apertures and measured gas flow rates through them. They observed fast permeation of light gases (*i.e.*, He, H_2, Ne) with suppressed flow of heavier noble gases, indicating size-dependent gas transport through GDY nanopores. For CO_2/CH_4 separation, nanoporous GDY exploited geometric effects, linear CO_2 could align with triangular pores, lowering barriers relative to spherical CH_4, whereas boron-GDY's larger hexagonal pores lost selectivity.[321] Quantum effects also emerge: Rafiei *et al.*[322] reported exceptionally high O_2/N_2 selectivity (*i.e.*, 10^6 at 100 K) due to differences in transmission barriers coupled with zero-point energy contributions. Strain engineering offers another pathway; rhombic N-GDY under 3–3.5% zigzag tensile strain achieved ultrahigh CO_2/N_2 selectivity (*i.e.*, 10^3–10^4) with high permeance.[323] Collectively, these findings underscore GDY's unique combination of intrinsic porosity, chemical stability, and tunability through functionalization, charge doping, or strain. However, most reports rely on DFT and MD predictions under idealized conditions. Realizing GDY's promise in industrial gas purification demands scalable synthesis of defect-controlled monolayers, validation under mixed-gas feeds, and long-term stability tests.

Recent computational studies have extended gas separation research to GTY and graphenylene membranes. Apriliyanto *et al.*[324] demonstrated that GTY multilayers combine permeation and adsorption mechanisms, with single layers showing a modest CO_2/N_2 selectivity (*i.e.*, 4.25), while bilayers improved the separation performance for post-combustion capture. Trilayers further enhanced CO_2 uptake due to interlayer adsorption, highlighting GTY's tunability and competitiveness with other carbon nanomaterials in emission control. Rezaee and Naeij[325] reported graphenylene-1 membranes as structurally stable and exceptionally selective, with remarkably low energy barriers for H_2 and He transport. Predicted selectivities reached extreme values (*i.e.*, 10^{27} for H_2/CO_2 and 10^{46} for H_2/CH_4), with permeance surpassing industrial benchmarks, especially at elevated temperatures. While these findings position GTY and graphenylene as highly promising candidates for CO_2 capture and H_2 purification, the extraordinary selectivities are largely derived from idealized MD and DFT models, and their experimental translation hinges on scalable synthesis and defect control.

Graphyne as a sensor

GRA's exceptional electronic and surface properties have long made it a reference material for gas sensing. However, its zero bandgap and poor selectivity severely limit its practical sensing performance despite its ability to detect trace gases such as CO, NO, NO_2, and NH_3.[152] These limitations have driven the exploration of GY and its derivatives as alternative 2D sensing materials with tunable band structures, diverse adsorption sites, and higher chemical reactivity.[326] The emergence of GY offers new opportunities for the development of selective gas sensors. GY exists in four structural forms: α, β, γ, and 6,6,12-GY. Among its allotropes, γ-GY-with a moderate bandgap (*i.e.*, ~0.46 eV) exhibits semiconducting behavior ideal for gas sensing, whereas α-, β-, and 6,6,12-GY remain metallic and less suitable.[326,327] The porous acetylenic framework of GY enhances gas–surface interactions and allows controllable modulation of its electronic and optical responses upon adsorption.

DFT and MD studies confirm the strong and orientation-dependent adsorption behavior of GY. Nikmanesh *et al.*[326] found CH_4 adsorption to be most favorable in the UP configuration (*i.e.*, −0.594 eV), indicating stable physisorption. Metal functionalization further enhanced performance, and Al-decorated γ-GY displayed strong nitrobenzene binding (*i.e.*, −1.18 eV), substantial charge transfer (*i.e.*, 0.57 e), and fast recovery (*i.e.*, 2.4 s at 450 K), ensuring both selectivity and reusability.[328] Singh *et al.*[329] similarly observed strong chemisorption and HOMO–LUMO gap reduction during SO_2 adsorption, confirming stable interaction and electronic sensitivity. Beyond pristine GY, heteroatom doping and hybridization significantly expand its sensing versatility. Au-doped BN-yne nanosheets exhibited improved hydroxyurea detection efficiency, electrical conductivity, and rapid recovery (*i.e.*, 1.36 s),[330] while γ-GY-like SiC nanoflakes with a 1.749 eV bandgap showed selective physisorption and strong charge transfer toward CNCl, underscoring their potential for toxic gas detection.[331]

Recent studies further highlight the tunability and superior sensing potential of GY through functionalization and heteroatom doping. Lakshmy *et al.*[328] demonstrated that Al anchoring enhances adsorption energy and charge transfer compared to pristine γ-GY, increasing work-function sensitivity by 10% and maintaining thermal stability under AIMD conditions, ideal for reusable nitrobenzene sensors. Similarly, Zhang *et al.*[332] showed that N-doped GY exhibits distinct conductivity modulation for volatile organic compounds, with maximum sensitivity to acetone (*i.e.*, 81%), highlighting its applicability in biomedical diagnostics such as non-invasive diabetes detection. The combination of physisorption and measurable conductance modulation highlights the potential of N-GY for biomedical diagnostics, including breath-based acetone sensing for diabetes detection.

Surface functionalization and heteroatom doping further broaden the potential of GY in environmental and molecular sensing by enhancing its electronic responsiveness, selectivity, and adsorption capability. Sakr *et al.*[333] demonstrated that γ-GY functionalized with electron-withdrawing groups (*i.e.*, $–NO_2$, –COOH, and –CN) exhibited improved adsorption affinity and bandgap reduction, following the stability order of $Gp–NO_2$ < Gp–COOH < Gp–CN < Gp–SOH < $Gp–CH_3$. Among these, $–NO_2$ functionalization showed the strongest interaction with heavy metal ions (*i.e.*, Hg^{2+}, Pb^{2+}, and Cd^{2+}) and a highly stable electronic structure, making it a strong candidate for wastewater monitoring. Similarly, Movlarooy and Nooranbjar[334] revealed that α-GY exhibits selective chemisorption of NO, O_2, and Cl_2, whereas CO_2 and F_2 remain weakly physisorbed, demonstrating that charge transfer-induced bandgap modulation enables high selectivity toward oxidizing gases.

Beyond chemical sensing, GY's mechanical flexibility and wide elastic strain range offer efficient electromechanical coupling, making it suitable for temperature and strain

sensing.[37] Its ability to undergo reversible deformation without lattice degradation underpins its application in flexible and wearable sensors. GDY, in particular, combines tunable electronic and mechanical properties, exhibiting strain- and temperature-dependent bandgap modulation. Thermally induced tensile strain increases the bandgap, generating measurable voltage responses and enabling self-regulating behavior in adaptive electronic systems such as thermally controlled transistors.[37]

GDY has been used as a support platform for electrochemical sensors such as Pt-nanoparticle-decorated GDY used to detect bisphenol AF with excellent sensitivity and low detection limits (*i.e.*, ~0.09 μM).[335] Recently, γ-GY films synthesized *via* chemical exfoliation have been demonstrated as functional room-temperature chemiresistive sensors, showing strong responses to low concentrations of NO_2 and high selectivity at room temperature, indicating real gas sensing capability in experiments.[336] GDYO has been experimentally employed in flexible, self-powered humidity sensors on fabric substrates, exploiting moisture adsorption to generate measurable electrical output, demonstrating the material's utility in real sensing systems.[337] HsGY sheets integrated with WO_3 nanoparticles have been experimentally developed for NO gas sensing at low temperatures, showing improved response values compared to pure WO_3 due to the conductive support of HsGY.[338]

Computational studies further emphasize the role of dopant engineering in enhancing the sensing efficiency of GDY. Xu *et al.*[339] found that pristine GDY interacts weakly with temozolomide, whereas B-doped GDY shows much higher adsorption energies (*i.e.*, −21.92 to −45.44 kcal mol^{-1}) and stronger charge transfer, demonstrating improved molecular sensitivity. Similarly, Kadhim *et al.*[340] reported that Si-doped GDY enhances cisplatin adsorption (*i.e.*, −49.39 kcal mol^{-1}) while improving conductivity, making Si-GDY a promising nanosensor for drug detection. Extending this concept, Lakshmy *et al.*[341,342] showed that transition-metal-doped HGY, particularly Sc-doped variants, exhibits robust adsorption, strong charge transfer, and AIMD-verified thermal stability for catechol and NH_3 detection. Collectively, these findings reveal that strategic functionalization and dopant engineering, especially with Sc, Si, and B, significantly strengthen GDY and HGY's electronic sensitivity, adsorption strength, and thermal resilience. This establishes them as highly adaptable materials for next-generation nanosensors targeting environmental pollutants, toxic gases, and biomedical analytes.

Detection of materials by pristine and doped GYs

Pristine GY. Majidi *et al.*[343] studied the adsorption behavior of hydrogen peroxide on GY to assess its potential for detection. All possible adsorption sites were considered, with H_2O_2 oriented both parallel and perpendicular to the GY sheet at each site. The highest binding energies were observed at the O site when the molecule was aligned parallel to the surface, and at the s site when oriented perpendicularly, indicating these as the most favorable adsorption positions. Zhang *et al.*[327] studied the adsorption behavior of individual gas molecules such as NH_3, CO, H_2S, SO_2, NO, and NO_2 on the GY surface. By comparing their binding energies, they identified the most energetically favourable (stable) configurations. Among the studied gas molecules, NO (*i.e.*, 0.263 eV), NO_2 (*i.e.*, 0.229 eV), and H_2S (*i.e.*, 0.157 eV) exhibited higher binding energies than those of CO (*i.e.*, 0.081 eV), NH_3 (*i.e.*, 0.133 eV), and SO_2 (*i.e.*, 0.238 eV), indicating stronger interactions with the GY surface. Guo *et al.*[344] explored the adsorption behavior of NO and NO_2 gases on both pristine GY and boron-doped γ-GY. Multiple initial configurations with different orientations and positions were considered to identify the most energetically favorable adsorption structures. For adsorption on pristine GY, four distinct sites (*i.e.*, TC1, TC2, H1, and H2) were analyzed.

The most stable configuration for NO adsorption was at the H2 site (see Fig. 13a) with nitrogen facing downward, exhibiting a binding energy of −0.16 eV. For NO_2, the highest binding energy (*i.e.*, −0.17 eV) was also observed at the H2 site, but with nitrogen oriented upward. Madhumitha *et al.*[345] explored the adsorption behavior of the nucleobases guanine and cytosine on pristine γ-GY sheets. As illustrated in Fig. 13b, cytosine was adsorbed at positions P1 and P2 through interactions involving oxygen and hydrogen atoms, respectively. Similarly, Fig. 13c shows guanine adsorption at positions P3 and P4 *via* oxygen and hydrogen atoms. The calculated adsorption energies indicated that configurations involving oxygen interactions P1 (*i.e.*, −0.637 eV) for cytosine and P3 (*i.e.*, −0.619 eV) for guanine were more energetically favorable than their hydrogen-interacting counterparts, P2 (*i.e.*, −0.363 eV) and P4 (*i.e.*, −0.460 eV). To identify the most stable configuration for a single CS_2 molecule adsorbed on a GY sheet, Zhang and Derakhshandeh[347] investigated the adsorption behavior of CS_2 gas on pristine GY using several plausible initial adsorption geometries.

Ebadi *et al.*[346] investigated the adsorption behavior of methanol and CO on pristine GDY by analyzing three possible adsorption sites (see Fig. 13d), each with different molecular orientations. For the H and h sites, the C–O bond of the adsorbates was positioned either perpendicular (C-head and O-head) or parallel to the GDY surface. In the case of the acetylenic link (*i.e.*, Position A), only parallel configurations with favorable interaction energies were considered. Their findings revealed that methanol favored the parallel orientation over perpendicular ones, while CO exhibited a preference for the perpendicular C-head configuration. Among all the adsorption sites evaluated, the H site emerged as the most energetically favorable for both methanol and CO. Quej *et al.*[348] explored hydrogen adsorption on γ-GY and γ-BNyne using DFT-D3. Results indicated that H_2 adsorption does not significantly affect their structural or electronic properties, confirming material stability under hydrogen exposure. These findings suggest γ-GY and γ-BNyne as promising candidates for applications in nanosensors, nanomedicine, and hydrogen storage.

Doped GY. Doping emerges as a powerful strategy to enhance the adsorption and sensing performance of GY. Felegari *et al.*[349] demonstrated that phosgene adsorption is markedly improved upon doping, with BN-doped GY showing moderate enhancement (*i.e.*, −4.77 to −7.15 kcal mol^{-1}) and Si-doped GY exhibiting

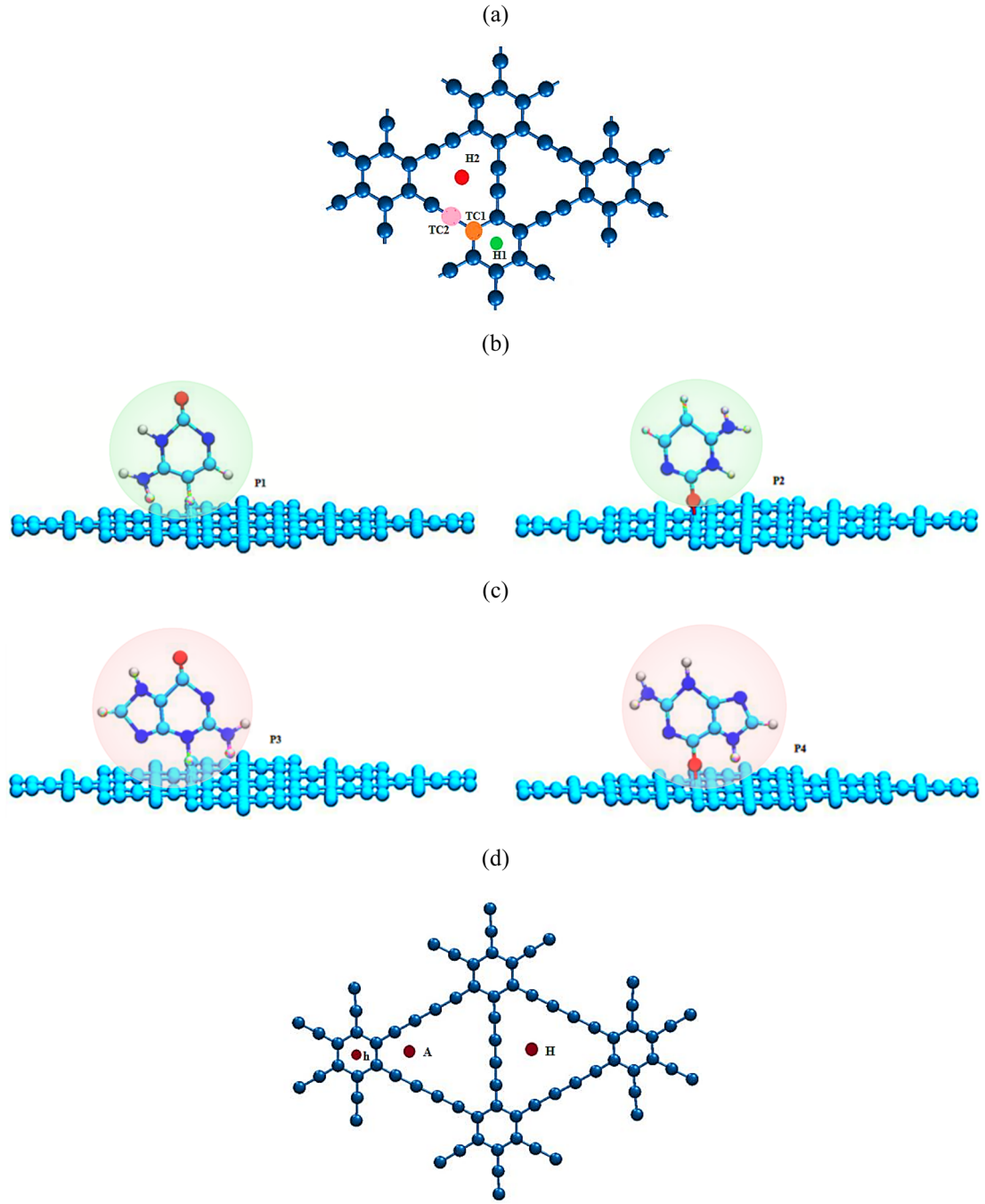

Fig. 13 (a) Representation of pristine GY with selected binding sites.[344] Adsorption behavior of nucleobases on GY nanosheets: (b) cytosine adsorption on pure γ-GY at P1 and P2 and (c) guanine adsorption on pure γ-GY at P3 and P4.[345] (d) Structure of GDY with possible adsorption sites.[346]

a dramatic increase (*i.e.*, −38.15 kcal mol^{-1}), highlighting silicon's efficacy in strengthening adsorbate interactions. Similarly, Vazhappilly *et al.*[350] reported that second- and third-period element doping (*i.e.*, B, Be, Al, N, P, and Si) significantly boosts noble gas adsorption (Xe and Kr) compared to pristine GY, with Al and P at the bottom surface providing the strongest binding. These findings underscore the critical role of both dopant identity and adsorption site in modulating adsorption strength. BN doping also enhances interactions with toxic molecules. Vessally *et al.*[351] showed that mustard gas preferentially binds to the boron site *via* its chlorine atom, with sequential adsorption energies slightly decreasing yet remaining substantial (*i.e.*, −18.3 to −17.2 kcal mol^{-1}), indicating strong multipoint adsorption facilitated by boron's low coordination number and positive charge. Oxidative functionalization similarly tunes electronic and adsorption properties: Mofidi and Vanani[352] found that oxygen incorporation at sp-hybridized carbons in graphyne oxide (GYO)

forms stable oxides (carbonyl favored over epoxy), enhancing CO, CO_2, and NH_3 adsorption and modulating band gaps.

Metal doping further amplifies adsorption and sensing performance. Zhang and Derakhshandeh[347] reported that Al-doped γ-GY shows significantly stronger CS_2 adsorption, with exothermic doping at two carbon sites (*i.e.*, −6.38 and −5.61 eV), highlighting the site-dependent efficacy of doping (see Fig. 14a and b). Yang *et al.*[353] demonstrated that Fe doping in γ-GY substantially increases adsorption energies for various gases (CO, O_2, NO, NO_2, and SO_2), with values up to −3.706 eV depending on the doping site (Fig. 14c), indicating markedly enhanced sensing capabilities. Collectively, these studies illustrate that element doping, whether with light atoms (*i.e.*, B, N, O, Si, and Al) or transition metals (Fe), can strategically tune GY's electronic structure, local charge distribution, and adsorption sites, thereby optimizing its interaction with diverse chemical species. The choice of dopant, its position, and the nature of the target molecule govern the extent of adsorption enhancement, making doped GY a highly versatile platform for gas sensing, toxic molecule detection, and adsorption-driven applications.

Zeng *et al.*[354] examined rare base (RB) adsorption on pristine and transition metal (*i.e.*, Fe, Co, and Ni)-doped γ-GY using DFT. While pristine γ-GY showed weak physisorption, TM-doping enabled stronger chemisorption, enhancing selectivity and sensitivity. Notably, Ni-GY exhibited high selectivity, whereas Fe-GY demonstrated excellent responsiveness, highlighting TM-GY nanosheets as promising candidates for RB detection and biosensor design. Li *et al.*[355] investigated rare base-pair adsorption on pristine and B/N-doped γ-GY using DFT. Results showed that B-doping enhanced adsorption stability compared to pure and N-doped γ-GY. Translocation time analysis confirmed that rare base-pairs can be effectively distinguished, while sensing response indicated that B-GY favored G-5hmCyt adsorption and N-GY favored G-Cyt. These findings highlight B/N-doped γ-GY nanosheets as promising candidates for biosensor development in epigenetic detection.

Hydrogen storage

Metal-decorated GBMs have emerged as highly promising candidates for hydrogen storage due to their unique in-plane π states, which are absent in sp^2-bonded GRA and fullerenes.[356,357] Calcium decoration notably enhances hydrogen storage capacity owing to strong Ca-GY interactions mediated by p_x–p_y π/π* states, as demonstrated by Li *et al.*[356] where Ca-GY achieved up to 9.6 wt% H_2 uptake with a binding energy of ∼0.2 eV per molecule, ideal for reversible storage without Ca clustering. Hwang *et al.*[357] confirmed the thermodynamic stability of this system, while comparative studies revealed that Ca-GY outperforms Ca-GRA, which stores only 8.4 wt% H_2.[358]

Another system of interest for H_2 storage is Li-decorated GY, benefiting from lithium's extremely low atomic mass.[359] Light metal decoration further improves performance. Li-GY exhibits exceptional hydrogen storage potential owing to lithium's low atomic mass and strong polarization capability, reaching up to 18.6 wt% storage with an optimal H_2 binding energy (*i.e.*, ∼0.2 eV).[360] Kumar and Dhilip Kumar[361] advanced this concept using a porous Li-decorated metal–GY framework (MGF-Li_8), where each Li atom adsorbs three H_2 molecules *via* charge-induced polarization, forming MGF-Li_8–H_{24}. The interaction leads to H–H bond elongation and decreasing adsorption energy (*i.e.*, 0.40–0.20 eV) with the increasing loading, indicating reversible physisorption. MD simulations further verified the high reversibility of the system and a practical hydrogen storage capacity of 6.4 wt% under ambient conditions.

Recent computational investigations highlight the exceptional hydrogen storage potential of metal-decorated GY derivatives due to their uniform pore networks, strong metal anchoring, and favorable adsorption energetics. Hussain *et al.*[362] demonstrated that boron-doped graphdiyne (BGDY) provides an ideal platform for light-metal functionalization, as its uniformly distributed pores enable stable incorporation of Li, Na, K, and Ca atoms with high binding energies and minimal clustering. Substantial charge transfer from dopants to the BGDY matrix induces positive polarization, enhancing H_2 adsorption through electrostatic interactions. The resulting storage capacities, 14.29, 11.11, 9.10, and 8.99 wt% for Li-, Na-, K-, and Ca-BGDY, significantly surpass those of most 2D materials, with adsorption energies (*i.e.*, 0.17–0.40 eV per H_2) ideally suited for reversible storage. Liu *et al.*[363] revealed that Li-decorated C_{68}-GY achieves a stable and dispersion-resistant configuration, where strong Li-substrate bonding prevents aggregation. The system exhibits a gravimetric storage capacity of 8.04 wt% with an optimal adsorption energy (*i.e.*, −0.227 eV per H_2), driven by electrostatic polarization and orbital hybridization between Li and H_2. Similarly, Gao *et al.*[34] reported a Li-decorated HGY exhibiting a storage capacity of 12.8 wt%, with each Li atom adsorbing four H_2 molecules *via* polarization-driven physisorption, and excellent thermodynamic reversibility verified through AIMD simulations.

Transition-metal functionalization further enhances the binding strength and thermal stability. Singh *et al.*[364] showed that Y-decorated HGY stores up to seven H_2 molecules per Y atom (*i.e.*, 9.34 wt%), exceeding the U.S. DOE target, with adsorption mediated by Kubas-type interactions and stability retained up to 438 K. Likewise, Zr-decorated γ-GY[30] demonstrated strong metal anchoring, high desorption temperature (*i.e.*, 574 K), and substantial gravimetric capacity (*i.e.*, 7.95 wt%), with diffusion barriers effectively preventing Zr clustering, conditions particularly favorable for fuel-cell applications. Collectively, these findings affirm that metal-decorated GY frameworks, especially Li-, Y-, and Zr-functionalized variants, combine high gravimetric density, optimal adsorption energies, and robust thermal reversibility, positioning them as promising candidates for next-generation solid-state hydrogen storage materials.

Transistors

GY and GDY exhibit exceptional potential as next-generation transistor materials due to their tunable band structures and superior charge transport characteristics. The mechanically adjustable band gap of GY enables post-fabrication tuning of transistor properties, such as on/off ratio[37] and carrier mobility, unlike conventional semiconductors, where doping fixes these

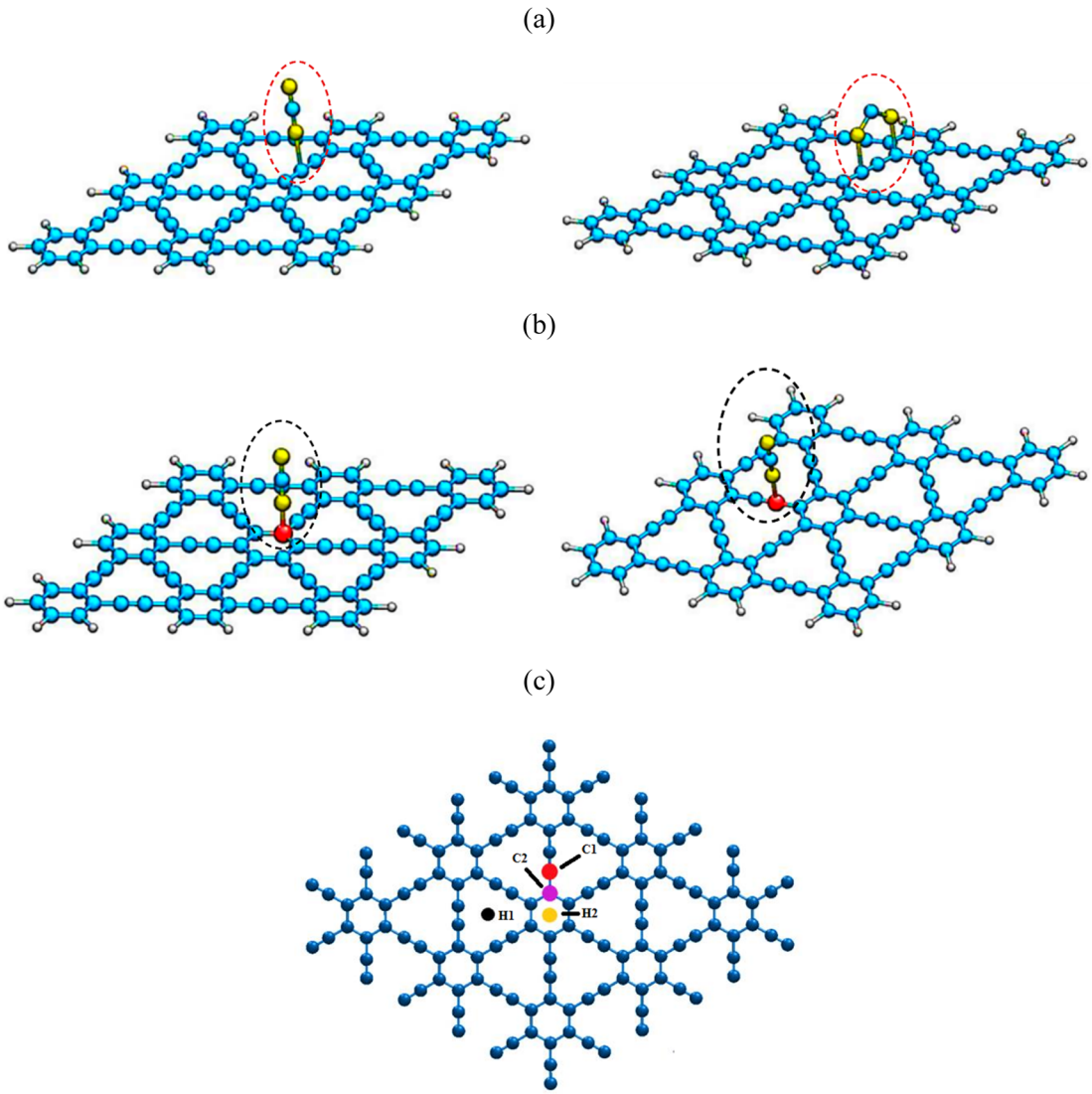

Fig. 14 Adsorption behaviour of the CS_2 molecule on (a) pristine and (b) Al-doped GY.[347] (c) Four possible sites of γ-GY for Fe atom-doped C1, C2, H1 and H2.[353]

parameters permanently. This mechanical tunability allows electronic characteristics to be modulated simply through geometric or strain-based design modifications, offering unprecedented flexibility in device engineering. GDY, with its low effective electron mass and appropriate band gap, demonstrates superior intrinsic carrier mobility compared to silicon, enabling faster switching even under low electric fields. This intrinsic advantage mitigates the performance constraints of traditional transistors that rely on aggressive channel scaling to enhance speed. Furthermore, GDY's band gap can be symmetrically and linearly modulated through mechanical strain, narrowing under compression and widening under tension, which provides predictable and precise control of electronic behavior, a desirable feature for transistor optimization. For example, a strain range of −0.05 to +0.06 modulates the band gap from 0.28 to 0.71 eV, respectively.[48]

From a quantum transport perspective, *ab initio* studies reveal that GY molecules function effectively as active elements in single-electron transistors operating under Coulomb blockade conditions.[365] DFT simulations highlight stable charge configurations and significant polarization-induced renormalization effects, with gate coupling values comparable to GRA and benzene-based systems, but notably higher than fullerene counterparts.[365] These findings underscore the promise of GY-based frameworks for high-performance nanoscale transistors, where controllable band gaps, high mobility, and quantum-level tunability collectively address the limitations of silicon-based technologies.

Field effect transistors

Material selection is central to transistor design, dictating trade-offs between charge transport efficiency, power consumption, and fabrication compatibility.[366] GY, with its intrinsically high electron mobility and low resistivity, has emerged as a potential next-generation channel material for field effect transistors (FETs). Its superior charge transport properties enable faster

switching and reduced power loss compared to conventional semiconductors. The tunable electronic structure of GY further allows flexibility in modulating device performance without chemical doping. Although research on GY-based FETs remains in its developmental phase, the combination of high carrier mobility, low resistance, and structural versatility makes GY a promising platform for high-performance, low-power nanoelectronic applications.

GDY introduces additional functionality owing to its electric-field-dependent band gap. Under a strong gate bias, GDY transitions from semiconducting to metallic behavior, facilitating efficient channel modulation.[37] Experimental studies have confirmed its semiconducting nature with a conductivity of 2.516×10^{-4} S m^{-1},[58] while theoretical models predict superior performance due to its low electron effective mass and strong π-conjugation. Simulated GDY-FETs with aluminum electrodes exhibit an on/off ratio of 10^4 and high on-state current (*i.e.*, 1.3×10^4 mA mm^{-1} at 10 nm channel length),[367] highlighting its capability for high-speed nanoscale electronics. Among GY allotropes, γ-GY-1 demonstrates excellent compatibility with tunneling FET (TFET) architectures. Rouzkhash *et al.*[368] reported that γ-GY-1 nanotubes (GYNTs) effectively suppress ambipolar behavior and improve subthreshold swing (SS), achieving values as low as 5 mV dec^{-1} for 9.6 nm 3AGYNT-TFETs with an ultrahigh on/off current ratio of 1.6×10^{10} at VDD = 0.2 V. These results, supported by the deformation potential and NEGF-DFTB analyses, indicate strong electron–phonon coupling and ballistic transport behavior, positioning GYNT-TFETs as viable low-power alternatives to silicon MOSFETs.

Heterostructure integration further enhances transistor performance. First-principles studies on GY/GRA van der Waals heterostructures reveal n-type ohmic contact formation with zero Schottky barrier height (SBH) and tunable electronic behavior under vertical electric fields.[369] The seamless charge transfer between GRA and GY layers facilitates efficient electron tunneling, offering design flexibility for all-carbon 2D FETs. Similarly, α-GY nanoribbon-based FETs have shown near-compliance with the International Roadmap for Devices and Systems 2022 targets, achieving an SS of 73.9 mV dec^{-1} and low dynamic power dissipation (*i.e.*, 0.00864 fJ μm^{-1}).[366] Interestingly, defect engineering, *via* single or edge vacancies, improves SS (*i.e.*, 59.8–63.3 mV dec^{-1}) at the expense of higher power dissipation, reflecting the tunability–stability trade-off in GY-based electronics. Together, these studies highlight the promise of GY and GDY for next-generation FETs, combining tunable band structures, high carrier mobility, and compatibility with quantum-scale device operation. Their structural diversity and integration potential mark a significant advancement beyond silicon and GRA platforms toward fully carbon-based nanoelectronics.

GDY thin-film transistors exhibit efficient and reversible performance modulation *via* light and thermal stimuli, delivering switching ratios up to 10^3–10^4 and enhanced conductivity (*i.e.*, $\sim 1.5 \times 10^4$ S m^{-1}), underscoring their suitability for logic and flexible electronic applications.[370] An interfacial method enables rapid synthesis of nitrogen-substituted GY films that act as efficient semiconductors in FETs, achieving carrier mobilities up to 9.8 cm^2 V^{-1} s^{-1} at low operating voltages, demonstrating strong potential for GY-based electronic devices.[371] GDY has been used as the active charge carrier layer in FET biosensor devices, where non-covalent functionalization preserved electrical properties and enabled ultrasensitive detection of biomolecules with high on/off ratios (*i.e.*, $>10^4$).[372] A noncovalent grafting strategy enables GDY to act simultaneously as a charge-transport layer and bioaffinity substrate in FET biosensors, allowing stable immobilization of receptors while preserving electrical properties for ultrasensitive detection.[372] GDY particles have been experimentally incorporated as nano-floating-gate materials in organic field-effect transistor (OFET) memory devices.[373] When blended into a polymer matrix, these OFETs show bipolar memory behavior with a large memory window (*i.e.*, up to ~86 V), long retention (*i.e.*, $>10^4$ s), and high ON/OFF current ratios (*i.e.*, $\sim 7.5 \times 10^5$), demonstrating GDY's capability as a functional charge-trapping medium in FET-type devices.

Nanofillers

GY demonstrates exceptional potential as a nanofiller in polymer composites due to its remarkable mechanical strength and high surface adhesion energy (*i.e.*, 223.5 mJ m^{-2}), which collectively enhance matrix–filler interfacial bonding and mitigate delamination, a primary failure mechanism in reinforced composites.[37] Edge-functionalized or well-dispersed GY flakes contribute to increased stiffness, strength, and isotropic mechanical behavior despite the intrinsic anisotropy of individual sheets, positioning GY as a superior alternative to conventional fillers like short graphite fibers.[124]

Beyond mechanical reinforcement, GY incorporation significantly improves functional properties. Luo *et al.*[374] reported that GY/polypyrrole (GY/PPy) composites exhibit enhanced thermal conductivity, with 20 wt% GY loading achieving ~90% higher conductivity than pure PPy, attributed to favorable flake aspect ratios and enhanced electronic transport. Similarly, in mixed-matrix membranes (MMMs), GY acts as a selective barrier and transport modulator. Luo *et al.*[311] demonstrated that the incorporation of GY into MMMs optimizes gas permeation, with adsorption capacities following $H_2O > CO_2 > O_2$, and oxygen diffusion reaching a maximum at ~15 wt% GY. These findings underscore GY's dual role as both a mechanical reinforcer and a functional nanofiller, offering a versatile strategy to tailor composite properties for advanced structural and separation applications.

GDY was used as an ultralow-loading filler in PVDF composites, demonstrating its strong potential for high-performance polymer thermal management and electronic cooling applications.[375] Experimental studies have fabricated γ-GY/graphitic carbon nitride quantum dot (CNQD) hybrid composites with epoxy matrices, showing improved tensile strength (*i.e.*, ~27% enhancement) and thermal properties compared to pure epoxy.[106]

Although GBMs have been proposed for diverse applications, their practical promise varies substantially when evaluated

through the lens of manufacturability, performance tolerance, and integration complexity. Applications such as membrane-based separation, catalysis, and electrochemical energy storage currently represent the most viable directions because they can operate effectively with multilayer, polycrystalline, and defect-containing GY structures, which are the dominant products of scalable synthesis methods. In membrane-based separations, for instance, selective transport is governed primarily by local pore chemistry and size, rather than long-range crystalline coherence, while during catalysis and in batteries, defects and heteroatom doping can actively enhance adsorption, charge transfer, and reaction kinetics. By contrast, nanoelectronic applications, including transistors and field-effect devices, demand stringent material requirements such as wafer-scale continuity, atomically precise thickness control, minimal defect densities, and stable metal-contact interfaces. These requirements are fundamentally misaligned with the current state of GY synthesis, which cannot yet deliver large-area, single-crystalline films with reproducible electronic properties. Similarly, hydrogen storage and sensing applications remain limited by intrinsic material constraints: hydrogen binding energies in GY are often insufficient for reversible storage under ambient conditions, while sensing performance is sensitive to environmental fluctuations and structural variability, complicating reproducibility and scale-up.

Biocompatibility

Assessing the suitability of GBMs for real-world applications necessitates evaluating their potential toxicological and ecological effects. Although GY family materials are newer than GRA and GO, emerging studies, especially on GDY, offer important insights into biocompatibility, cytotoxicity, and environmental interactions of such carbon frameworks. In this context, Zheng *et al.*[376] systematically compared GDYO and GO with similar sizes and morphologies, evaluating their physicochemical properties and cytotoxic responses. GO was quite stable in aqueous media but rapidly aggregated in saline solutions, whereas GDYO maintained significantly higher stability in both aqueous and saline media. This enhanced stability of GDYO is attributed to stronger intermolecular hydrogen bonding and acetylenic bonds that link carboxyl groups within its structure. The results showed that GO prefers to stick onto cell membranes, causing membrane ruffling and elevated reactive oxygen species (ROS) generation, which ultimately leads to cytotoxicity and cell death. Conversely, GDYO exhibited minimal impacts on cell viability and induced significantly lower levels of apoptosis, suggesting that GDYO is safer and more biocompatible than GO in biological systems. In recent years, GDY and its derivatives have demonstrated significant promise in biological fields, driven by their distinctive structural characteristics and notable functional properties.[377] These advantages place GDY-based materials at the forefront of emerging material platforms for diverse biomedical and bio-related applications, including cell proliferation, differentiation/maturation, targeted drug delivery, enzyme catalysis, anticancer therapy, and biosensing. For instance, the proteins adsorbed on GDY sheets showed minimal molecular-level structural perturbations, which are likely attributed to the heterogeneous surface energy distribution arising from the presence of distinct carbon bonding environments in GDY.[377] Moreover, the unique geometry of GDY promotes point-to-point protein adsorption rather than face-to-face contact, a mode of interaction that markedly reduces protein deformation and preserves their native structure. Furthermore, GDY has been demonstrated to be an effective platform for loading and delivering therapeutic agents, metal ions, proteins, and nanocatalysts across diverse application scenarios. The triple carbon bonds in GDY provide potential active sites that can engage in both covalent and noncovalent interactions with external ligands. In biological applications, these sites enable GDY to form covalent linkages with targeting agents, tracking molecules, or biocompatible functional groups. Structurally, the acetylenic bond consists of one σ bond and two π bonds, whose electron pairs can act as electron donors to coordinate with transition metal atoms possessing vacant orbitals, thereby facilitating metal binding and functionalization.

Coupling the intrinsic properties, such as unique pore structure and fully conjugated networks, with rational surface engineering approaches, including elemental doping and biomolecular functionalization, further broadens the applicability of GDY biomaterials by enabling tailored interactions with biological systems (*i.e.*, enhanced cellular uptake and reduced nonspecific cytotoxicity), suggesting favorable biocompatibility under controlled conditions.[378] Preliminary *in vitro* investigations have shown that GDY demonstrates relatively low cytotoxicity toward mammalian cell lines at moderate concentrations, with cell viability strongly dependent on dosage, exposure time, and surface functionalization.[379] The presence of uniformly distributed pores in GBMs has been proposed to reduce membrane disruption effects commonly observed in GBMs, potentially improving biocompatibility in drug delivery and biosensing applications.[380]

Experimental work has demonstrated that GDYO can undergo biological degradation, producing quantum dots that elicit a minor foreign-body response *in vivo*, indicating that GBMs may not be inherently inert but do engage dynamically with biological environments, with implications for both safety and clearance pathways.[381] Moreover, acute toxicity to aquatic organisms such as microalgae has been reported, with GDY shown to influence gene expression associated with lipid metabolism and autophagy, and exhibit dose-dependent effects in larvae development models, highlighting species-specific sensitivities and ecological risk potentials.[382] These findings indicate that although GBMs may exhibit lower cytotoxicity than materials such as GO under certain conditions, they still interact with biological systems in nontrivial ways, highlighting the need for careful evaluation of their biological effects. Furthermore, the biological impact of GBMs is strongly influenced by physicochemical factors such as size, shape, surface chemistry, oxidative state, dispersion, and functional groups.

Environmental impact assessments of GBMs are even more limited but critically important, given their proposed use in water purification, ion separation, and catalytic applications.

Early eco-toxicological evaluations suggest that GDY exhibits lower toxicity toward aquatic microorganisms than GO, potentially due to its lower defect density and reduced generation of ROS. However, concerns remain regarding long-term persistence, bioaccumulation, and degradation pathways in natural ecosystems. The high chemical stability of sp–sp^2 carbon frameworks may lead to prolonged environmental residence times, necessitating further investigation into their life-cycle impact.

Long-term stability of GBMs

A critical prerequisite for the practical deployment of GBMs across diverse applications is their long-term structural and functional stability under operational conditions. One of the primary concerns in membrane applications is the ability of GBMs to maintain structural and chemical integrity when exposed to variable pH, ionic environments, and mechanical forces over time. The porous and less densely packed carbon network of GBMs is inherently different from GRA. Theoretical studies have shown that while GY and GDY structures are stable at elevated temperatures and maintain covalent bonding networks, their stability can be lower than that of GRA due to reduced π–π stacking and overall structural porosity, which may predispose them to deformation under stress or in aggressive chemical environments.[383] Earlier molecular simulations of GY membranes reveal that 2D GY sheets exhibit high mechanical strength and tolerance to deformation, with ultimate stresses in the gigapascal range and modest tensile strain limits, suggesting that they can withstand installation and pressure differentials typical in filtration modules.[212] However, these analyses measure static or short-duration mechanical tolerances rather than cumulative mechanical degradation or fatigue relevant to real membrane service life.

While recent computational studies consistently demonstrate the intrinsic structural integrity, thermal robustness, and mechanical strength of various GY allotropes, these investigations are largely limited to idealized or short-timescale conditions and do not offer systematic, long-term degradation assessments under realistic chemical and mechanical environments relevant to practical membrane applications. Latest atomistic simulations and DFT studies indicate that emerging GY structures, such as TH-GY, exhibit substantial mechanical resilience, characterized by high Young's modulus values (*i.e.*, ~263–356 GPa) and confirmed dynamical stability from phonon dispersion analyses and AIMD at elevated temperatures.[120] These findings suggest a mechanically robust lattice capable of withstanding applied stress, which is essential for maintaining membrane integrity under pressure. Nevertheless, these assessments are primarily confined to short-timescale simulations and intrinsic material properties and do not address long-term mechanical deformation, fatigue, or failure mechanisms under continuous membrane operation. Detailed MD studies of GY variants such as 8-16-4-GY reveal that vacancy defects, microcracks, and elevated temperatures strongly influence mechanical behavior, with crack formation leading to pronounced degradation in mechanical performance and pre-existing defects promoting brittle fracture.[384] The fracture in 8-16-4-GY initiates with the breaking of ethylene bonds once the strain approaches a critical threshold of about 0.29. While these findings underscore the critical role of realistic structural imperfections in governing mechanical durability, they do not extend to correlating such defect-driven degradation with long-term operational failure modes over extended service lifetimes relevant to membrane applications.

In energy storage systems, especially Li ion and Li–S batteries, GBMs have been explored both as active electrode components and as protective interlayers. Atomistic simulations suggest that nanoporous GY and GDY layers can facilitate Li ion transport while preventing electrolyte penetration to electrodes, contributing to enhanced safety and performance in solid-state configurations.[385] However, ensuring that these materials retain their structural integrity during extensive cycling is critical: repeated lithiation/delithiation, ion intercalation, and volumetric changes can stress the carbon lattice, potentially leading to microcracks, delamination, or pore collapse. Although direct experimental studies on GBM cycling stability remain limited, analogous work on other 2D carbon materials indicates that mechanical deformation and fracture can significantly contribute to capacity fading and performance loss over time when volume changes are large.[386] In composites such as GDY grown on scaffold materials, enhanced cycle stability has been observed, but long-term studies (*i.e.*, hundreds to thousands of cycles) are needed to validate durability claims under realistic conditions.[387]

Understanding the degradation mechanisms, whether chemical (*i.e.*, oxidation and hydrolysis in aqueous environments), mechanical (*i.e.*, crack formation and pore coalescence), or electrochemical (*i.e.*, SEI formation, volume changes during cycling), is essential for rational GBM design. For example, carbon materials in membrane or battery environments can undergo surface oxidation or react with electrolyte species over time, leading to the loss of pore integrity or mechanical weakening. Insights from studies on GRA and related materials show that such degradation pathways can be mitigated by surface passivation, doping, or integration with mechanically robust matrices, indicating that similar strategies could be adapted for GY systems.[383]

Conclusion and future outlook

The remarkable progress in GBMs has unlocked vast potential across diverse technological frontiers, surpassing many other carbon allotropes due to their unique hybridized structure, tunable electronic properties, and intrinsic porosity. This review has comprehensively examined the evolution of GBMs, particularly the transition from GRA analogs to advanced GY systems, emphasizing their structural versatility, electronic tunability, and emerging functional applications. In membrane separation processes, GY membranes have shown immense promise, with tunable pore sizes, chemical functionalization, and doping strategies enabling superior selectivity and permeability. MD simulations have revealed that γ-GY-3 and γ-GY-4 can achieve water permeability up to two orders of magnitude

higher than the best-performing RO membranes while maintaining complete salt rejection. Complementary DFT studies have further elucidated the underlying adsorption energies, charge transfer behavior, and interaction mechanisms, providing an atomistic-level understanding critical for the rational GY membrane design. Beyond desalination and wastewater treatment, the exceptional electronic conductivity, adjustable bandgap, and mechanical robustness of GY significantly broaden its scope of applications. GY-based materials hold promises for next-generation sensors and optoelectronic devices, while their intrinsic porous architecture and strong chemical stability make them suitable for membrane separations, gas purification, and energy storage systems. Furthermore, GY's high catalytic activity, hydrogen storage potential, and structural adaptability position it as a strategic candidate for energy conversion and catalytic processes. While GBMs are often highlighted for their exceptional properties in applications such as ion batteries and membrane separation, these assessments are predominantly based on idealized simulations that assume perfect, defect-free structures, uniform pore sizes, and optimal functionalization. In practice, GBMs are highly sensitive to structural defects, edge irregularities, and chemical heterogeneity, which can drastically reduce ion selectivity, permeability, and mechanical robustness. Moreover, scaling up GBMs for device integration poses significant fabrication challenges including the production of large-area continuous films and ensuring interfacial compatibility with electrodes or membranes. Long-term chemical and mechanical stability under realistic operational conditions such as repeated cycling, exposure to electrolytes, or pressure gradients remains largely unexplored, yet it is crucial for practical deployment.

However, scalable and cost-effective synthesis with high crystallinity of GBMs remains fundamentally constrained by kinetic and thermodynamic limitations. Unlike GRA, which is composed entirely of sp^2-hybridized carbon stabilized by strong π–π conjugation, GBMs such as GY and GDY comprise mixed sp–sp^2 carbon networks with acetylenic linkages that possess higher formation energies and reduced thermodynamic stability under equilibrium conditions. First-principles calculations consistently indicate that GY allotropes are energetically less favorable than GRA, favoring the formation of sp^2-dominated carbon phases and hindering the growth of extended, defect-free crystalline domains.[158] Consequently, GBM synthesis is often governed by kinetic control, where irreversible C–C coupling reactions readily trap metastable, disordered, or amorphous structures unless narrowly optimized conditions are employed. The core difficulty lies in the formation of acetylenic (–C≡C–) linkages, which require precise catalytic conditions and high activation energies for sp–sp^2 coupling, often resulting in side reactions, chain buckling, or cross-linking that introduce defects and low crystallinity. Even recent approaches that embed GDY motifs into well-defined covalent organic framework (COF) architectures, facilitating crystalline GDY analogues, underscore that controlling the linkage distribution and framework periodicity is critical to suppress random coupling and defect formation, yet this introduces additional synthetic complexity and cost.[388] Moreover, controlling the number of layers and uniform layer stacking is difficult because sp–sp^2 hybridization weakens interlayer π–π stacking relative to GRA, increasing the likelihood of both stacking faults and heterogeneous domains, which, in turn, impairs the electronic and mechanical properties essential for applications. The lack of reversible error-correction mechanisms in typical irreversible polymerization pathways further limits the ability to anneal out defects during growth, as seen in many crystalline 2D polymers. Finally, large-scale synthesis is constrained by the availability of suitable precursors, catalysts, and substrates, as well as by the need to balance reaction conditions that favor network growth with those that minimize unwanted side reactions and structural disorder; this contributes to high production costs and limited reproducibility, blocking commercial adoption.[85]

The biocompatibility and structural flexibility of certain GY derivatives also open new pathways in biomedical applications, such as drug delivery, biosensing, and tissue engineering, as well as in environmental remediation and pollution control technologies. Moreover, the long-term stability of GY membranes under harsh chemical and thermal conditions continues to hinder commercial translation. Although GY offers precise ion sieving due to its intrinsic tunable pore size, achieving high selectivity among similarly sized metal ions remains a challenge. Moreover, one critical aspect is toxicity, as previous studies on GRA family nanomaterials have shown that factors such as lateral size, surface structure, functionalization, and aggregation influence cytotoxic effects.[389] However, the toxicological assessments also remain largely unexplored, necessitating further experimental and environmental studies to ensure safe and sustainable deployment.

Looking ahead, developing advanced functionalization and doping strategies, incorporating chemical ligands or hybrid nanostructures such as metal–organic frameworks, could further improve ion selectivity and separation efficiency. The design of multifunctional GY membranes capable of simultaneous removal of multiple contaminants, including heavy metals and radioactive ions, offers a promising direction for future research. Additionally, retrofitting GY-based membranes into existing industrial separation infrastructures could accelerate their practical adoption. From a computational perspective, MD and DFT are powerful tools for exploring the unique properties of GBMs and guiding the rational design of next-generation GBMs with tailored functionalities for environmental, energy, and healthcare applications. While MD simulations enable the dynamic investigation of ion transport, water permeation, and rejection mechanisms at the nanoscale, DFT offers atomistic-level insights into adsorption energies, charge transfer, electronic structures, and interfacial interactions. Together, these complementary approaches deepen our understanding of the structure–property relationships that govern GY's separation performance, sensing, and catalytic activity. Despite this promise, several challenges remain. The high computational costs required to simulate millions of atoms over numerous time steps limited timescales that constrain the investigation of slower processes, including large-scale structural changes and sensitivity to the precision of force

fields, which approximate interatomic interactions and directly impact the dependability of the computational results.[390–392]

In summary, GBMs represent a transformative platform with cross-disciplinary impacts, bridging nanoscience and practical technology. With sustained research efforts focused on scalable synthesis, defect control, performance optimization, and toxicity evaluation, GBMs are poised to revolutionize advanced separation, sensing, energy conversion, and biomedical systems, contributing to a sustainable and technologically advanced future.

Author contributions

Drisya G. Chandran: writing – original draft, methodology, investigation, formal analysis, data collection, visualization, conceptualization. N. Ramkumar: writing – original draft, methodology, investigation, formal analysis, data collection, visualization, conceptualization. Rima Biswas: writing – review & editing, supervision, validation, investigation, formal analysis, data collection, visualization, methodology, conceptualization.

Conflicts of interest

The authors declare no competing interests.

Data availability

All data discussed in this review were obtained from previously published studies and publicly available sources, which are cited throughout the manuscript. No primary research results, software or code have been included and no new data were generated or analysed as part of this review.

Acknowledgements

The authors gratefully acknowledge the School of Chemical Engineering, Vellore Institute of Technology, Vellore Campus, for providing the necessary facilities. This research did not receive any financial support from public, commercial, or non-profit funding bodies.

References

1 D. G. Chandran, L. Muruganandam and R. Biswas, *Environ. Sci. Pollut. Res.*, 2023, **30**, 110010–110046.
2 N. Ramkumar and P. Monash, *Environ. Sci.: Water Res. Technol.*, 2025, **11**, 1086–1136.
3 D. G. Chandran, L. Muruganandam and R. Biswas, *Mol. Simul.*, 2025, 1–22.
4 S. Lei, Q. Cao, X. Geng, Y. Yang, S. Liu and Q. Peng, *Crystals*, 2018, **8**, 465.
5 D. G. Chandran, L. Muruganandam and R. Biswas, *Chem. Eng. J. Adv.*, 2025, 100891.
6 D. G. Chandran, L. Muruganandam and R. Biswas, *Quantum Optics Devices on a Chip*, 2025, pp. 35–54.
7 A. James, C. John, C. Owais, S. N. Myakala, S. C. Shekar, J. R. Choudhuri and R. S. Swathi, *RSC Adv.*, 2018, **8**, 22998–23018.
8 Y. Li, J. Wu, C. Li, Q. Wang and L. Shen, *ACS Omega*, 2021, **6**, 10997–11004.
9 B. G. Kim and H. J. Choi, *Phys. Rev. B: Condens. Matter Mater. Phys.*, 2012, **86**, 115435.
10 E. Eray, V. Boffa, M. K. Jørgensen, G. Magnacca and V. M. Candelario, *J. Membr. Sci.*, 2020, **606**, 118080.
11 M. Kuhn, A. Bakshi, E. Sheridan, F. Rodrigues, A. Vincent, M. Moeller and R. Neufert, *Ceram. Environ. Syst.*, 2016, 119–128.
12 M. S. Sankhla, M. Kumari, M. Nandan, R. Kumar and P. Agrawal, *Int. J. Curr. Microbiol. Appl. Sci.*, 2016, **5**, 759–766.
13 S. Bolisetty, M. Peydayesh and R. Mezzenga, *Chem. Soc. Rev.*, 2019, **48**, 463–487.
14 J. R. Werber, C. O. Osuji and M. Elimelech, *Nat. Rev. Mater.*, 2016, **1**, 1–15.
15 W. Cheng, J. Ma, X. Zhang and M. Elimelech, *Environ. Sci. Technol. Lett.*, 2019, **6**, 492–498.
16 M. D. Young and C. Esau, in *Investing in Water for a Green Economy*, Routledge, 2015, pp. 45–57.
17 H. Li, T.-J. Ko, M. Lee, H.-S. Chung, S. S. Han, K. H. Oh, A. Sadmani, H. Kang and Y. Jung, *Nano Lett.*, 2019, **19**, 5194–5204.
18 N. Abdullah, N. Yusof, W. Lau, J. Jaafar and A. Ismail, *J. Ind. Eng. Chem.*, 2019, **76**, 17–38.
19 M. Qasim, M. Badrelzaman, N. N. Darwish, N. A. Darwish and N. Hilal, *Desalination*, 2019, **459**, 59–104.
20 Y. Zhai, G. Liu and W. G. van der Meer, *Engineering*, 2022, **9**, 27–34.
21 N. Ramkumar and P. Monash, *J. Environ. Chem. Eng.*, 2025, 119571.
22 M. M. Pendergast and E. M. Hoek, *Energy Environ. Sci.*, 2011, **4**, 1946–1971.
23 T. Humplik, J. Lee, S. O'hern, B. Fellman, M. Baig, S. Hassan, M. Atieh, F. Rahman, T. Laoui and R. Karnik, *Nanotechnology*, 2011, **22**, 292001.
24 H. Li, J. H. Lim, Y. Lv, N. Li, B. Kang and J. Y. Lee, *Chem. Rev.*, 2023, **123**, 4795–4854.
25 Z. Xu, X. Lv, J. Li, J. Chen and Q. Liu, *RSC Adv.*, 2016, **6**, 25594–25600.
26 T. Jeon, Y. C. Lee and S. C. Jung, *Nanoscale*, 2025, **17**, 15924–15934.
27 K. H. Lasisi, O. K. Abass, K. Zhang, T. F. Ajibade, F. O. Ajibade, J. O. Ojediran, E. S. Okonofua, J. R. Adewumi and P. D. Ibikunle, *Front. Chem.*, 2023, **11**, 1125625.
28 J. Deb, R. Ahuja and U. Sarkar, *ACS Appl. Nano Mater.*, 2022, **5**, 10572–10582.
29 H. Liu, X. Li, H. Chen, J. Chen and Z. Shi, *Phys. Chem. Chem. Phys.*, 2024, **26**, 8426–8435.
30 M. Singh, A. Shukla and B. Chakraborty, *Int. J. Hydrogen Energy*, 2023, **48**, 37834–37846.

31 P. Ruggerone, A. Kley and M. Scheffler, *arXiv*, 1998, preprint, arXiv:cond-mat/9802012, DOI: 10.48550/arXiv.cond-mat/9802012.
32 S. Majidi, H. Erfan-Niya, J. Azamat, E. R. Cruz-Chú and J. H. Walther, *J. Phys. Chem. B*, 2021, **125**, 12254–12263.
33 G. Piccini, M.-S. Lee, S. F. Yuk, D. Zhang, G. Collinge, L. Kollias, M.-T. Nguyen, V.-A. Glezakou and R. Rousseau, *Catal. Sci.*, 2022, **12**, 12–37.
34 Y. Gao, H. Zhang, H. Pan, Q. Li and J. Zhao, *Nanotechnology*, 2021, **32**, 215402.
35 J. Kang, Z. Wei and J. Li, *ACS Appl. Mater. Interfaces*, 2018, **11**, 2692–2706.
36 H. Qiu, M. Xue, C. Shen, Z. Zhang and W. Guo, *Adv. Mater.*, 2019, **31**, 1803772.
37 Q. Peng, A. K. Dearden, J. Crean, L. Han, S. Liu, X. Wen and S. De, *Nanotechnol., Sci. Appl.*, 2014, 1–29.
38 Y. Fang, Y. Liu, L. Qi, Y. Xue and Y. Li, *Chem. Soc. Rev.*, 2022, **51**, 2681–2709.
39 A. Balaban, C. C. Rentia and E. Ciupitu, *Rev. Roum. Chim.*, 1968, **13**, 231–247.
40 R. Baughman, H. Eckhardt and M. Kertesz, *J. Chem. Phys.*, 1987, **87**, 6687–6699.
41 Z. Jia, Y. Li, Z. Zuo, H. Liu, C. Huang and Y. Li, *Acc. Chem. Res.*, 2017, **50**, 2470–2478.
42 M. Mehrdad and A. Moosavi, *Polymer*, 2019, **175**, 310–319.
43 J. Kou, X. Zhou, H. Lu, F. Wu and J. Fan, *Nanoscale*, 2014, **6**, 1865–1870.
44 S. Wang, J. Li, X. Zhu and M. Wang, *Carbon*, 2019, **143**, 517–522.
45 M. M. Haley, S. C. Brand and J. J. Pak, *Angew. Chem., Int. Ed. Engl.*, 1997, **36**, 836–838.
46 C. Pan, C. Wang, Y. Fang, Y. Zhu, H. Deng and Y. Guo, *Environ. Sci. Nano*, 2021, **8**, 1863–1885.
47 A. Ivanovskii, *Prog. Solid State Chem.*, 2013, **41**, 1–19.
48 Y. Pei, *Phys. B*, 2012, **407**, 4436–4439.
49 A. T. Balaban and K. P. C. Vollhardt, *Open Org. Chem. J.*, 2011, **5**, 117–126.
50 L. Wang, F. Li, J. Wang, Y. Li, W. Li, Y. Yang, M. Zhao and Y. Qu, *Phys. Chem. Chem. Phys.*, 2020, **22**, 9789–9795.
51 M. Gholami, F. Melin, R. McDonald, M. J. Ferguson, L. Echegoyen and R. R. Tykwinski, *Angew. Chem., Int. Ed.*, 2007, **46**, 9081–9085.
52 F. Diederich, *Nature*, 1994, **369**, 199–207.
53 J. M. Kehoe, J. H. Kiley, J. J. English, C. A. Johnson, R. C. Petersen and M. M. Haley, *Org. Lett.*, 2000, **2**, 969–972.
54 T. Yoshimura, A. Inaba, M. Sonoda, K. Tahara, Y. Tobe and R. V. Williams, *Org. Lett.*, 2006, **8**, 2933–2936.
55 M. M. Haley, *Pure Appl. Chem.*, 2008, **80**, 519–532.
56 C. Lee, X. Wei, J. W. Kysar and J. Hone, *Science*, 2008, **321**, 385–388.
57 K. S. Kim, Y. Zhao, H. Jang, S. Y. Lee, J. M. Kim, K. S. Kim, J.-H. Ahn, P. Kim, J.-Y. Choi and B. H. Hong, *Nature*, 2009, **457**, 706–710.
58 G. Li, Y. Li, H. Liu, Y. Guo, Y. Li and D. Zhu, *Chem. Commun.*, 2010, **46**, 3256–3258.
59 D. Tan, W. Fan, W. Xiong, H. Sun, Y. Cheng, X. Liu, C. Meng, A. Li and W. Q. Deng, *Macromol. Chem. Phys.*, 2012, **213**, 1435–1440.
60 Q. Yuan and F. Ding, *Nanoscale*, 2014, **6**, 12727–12731.
61 H. Qi, P. Yu, Y. Wang, G. Han, H. Liu, Y. Yi, Y. Li and L. Mao, *J. Am. Chem. Soc.*, 2015, **137**, 5260–5263.
62 J. Zhou, X. Gao, R. Liu, Z. Xie, J. Yang, S. Zhang, G. Zhang, H. Liu, Y. Li and J. Zhang, *J. Am. Chem. Soc.*, 2015, **137**, 7596–7599.
63 B. Cirera, Y.-Q. Zhang, J. Björk, S. Klyatskaya, Z. Chen, M. Ruben, J. V. Barth and F. Klappenberger, *Nano Lett.*, 2014, **14**, 1891–1897.
64 B. Wu, M. Li, S. Xiao, Y. Qu, X. Qiu, T. Liu, F. Tian, H. Li and S. Xiao, *Nanoscale*, 2017, **9**, 11939–11943.
65 X. Kong, Y. Huang and Q. Liu, *Carbon*, 2017, **123**, 558–564.
66 Q. Li, Y. Li, Y. Chen, L. Wu, C. Yang and X. Cui, *Carbon*, 2018, **136**, 248–254.
67 J. Lee, Y. Li, J. Tang and X. Cui, *Acta Phys.-Chim. Sin.*, 2018, **34**, 1080.
68 Q. Li, C. Yang, L. Wu, H. Wang and X. Cui, *J. Mater. Chem. A*, 2019, **7**, 5981–5990.
69 Q. Li, C. Yang, L. Wu, H. Wang and X. Cui, *J. Mater. Chem. A*, 2023, **11**, 20271–20272.
70 J. Li, S. Li, Q. Liu, C. Yin, L. Tong, C. Chen and J. Zhang, *Small*, 2019, **15**, 1805344.
71 Y. Song, X. Li, Z. Yang, J. Wang, C. Liu, C. Xie, H. Wang and C. Huang, *Chem. Commun.*, 2019, **55**, 6571–6574.
72 Z. Yang, C. Zhang, Z. Hou, X. Wang, J. He, X. Li, Y. Song, N. Wang, K. Wang and H. Wang, *J. Mater. Chem. A*, 2019, **7**, 11186–11194.
73 Y. Lin, H. Liu, C. Yang, X. Wu, C. Du, L. Jiang and Y. Zhong, *Appl. Catal., B*, 2020, **264**, 118479.
74 W. Ding, M. Sun, Z. Zhang, X. Lin and B. Gao, *Ultrason. Sonochem.*, 2020, **61**, 104850.
75 F. Sedona, M. M. S. Fakhrabadi, S. Carlotto, E. Mohebbi, F. De Boni, S. Casalini, M. Casarin and M. Sambi, *Phys. Chem. Chem. Phys.*, 2020, **22**, 12180–12186.
76 X. Yu, L. Cai, M. Bao, Q. Sun, H. Ma, C. Yuan and W. Xu, *Chem. Commun.*, 2020, **56**, 1685–1688.
77 W. Ding, M. Sun, B. Gao, W. Liu, Z. Ding and S. Anandan, *Dalton Trans.*, 2020, **49**, 10958–10969.
78 G. Abdi, A. Filip, M. Krajewski, K. Kazimierczuk, M. Strawski, P. Szarek, B. Hamankiewicz, Z. Mazej, G. Cichowicz and P. J. Leszczyński, *RSC Adv.*, 2020, **10**, 40019–40029.
79 J. Liang, J. Wu, Y. Zhang, X. Zhao and C. Yuan, *Tetrahedron*, 2021, **89**, 132171.
80 B. Gao, M. Sun, W. Ding, Z. Ding and W. Liu, *Appl. Catal., B*, 2021, **281**, 119492.
81 Q. Pan, S. Chen, C. Wu, F. Shao, J. Sun, L. Sun, Z. Zhang, Y. Man, Z. Li and L. He, *CCS Chem.*, 2021, **3**, 1368–1375.
82 D. Zhao and J. Han, *Synfacts*, 2022, **18**, 1080.
83 J. Yang, Z. Bi, S. Zhang, L. Zeng, Y. Zhang, Y. Wang, J. Yan, W. Zhao, Y. Dai and J. Yun, *Diamond Relat. Mater.*, 2022, **129**, 109336.
84 M. Barua, A. Saraswat and C. Rao, *Carbon*, 2022, **200**, 247–252.

85 V. G. Desyatkin, W. B. Martin, A. E. Aliev, N. E. Chapman, A. F. Fonseca, D. S. Galvão, E. R. Miller, K. H. Stone, Z. Wang and D. Zakhidov, *J. Am. Chem. Soc.*, 2022, **144**, 17999–18008.
86 Y. Xu, Y. Yue, F. Kong and S. Ren, *Chem. Eng. J.*, 2022, **435**, 135121.
87 Y. Zheng, M. Sun, W. Sun, X. Meng, X. Huang and Z. Li, *Sep. Purif. Technol.*, 2022, **301**, 122062.
88 X. Liu, S. M. Cho, S. Lin, Z. Chen, W. Choi, Y.-M. Kim, E. Yun, E. H. Baek, D. H. Ryu and H. Lee, *Matter*, 2022, **5**, 2306–2318.
89 Z. Liu, Y. Li and Z. Jin, *J. Mater. Chem. C*, 2023, **11**, 9327–9340.
90 L. Wu, Q. Li, C. Yang, X. Ma, Z. Zhang and X. Cui, *J. Mater. Chem. A*, 2023, **11**, 16414–16415.
91 S. He, B. Wu, Z. Xia, P. Guo, Y. Li and S. Song, *Nanoscale Adv.*, 2023, **5**, 2487–2492.
92 Z. Zhang, Z. Li, L. Xia, R. Wang, Y. Cao, Z. Cheng and Y. Huang, *Nano Res.*, 2023, **16**, 88–100.
93 J. Yin, J. Liang, C. Yuan and W. Zheng, *Nanomaterials*, 2023, **13**, 1018.
94 Z. Jin and Y. Wu, *Green Chem.*, 2023, **25**, 9251–9261.
95 T. Song, H. Liu, H. Zou, C. Wang, S. Shu, H. Dai and L. Duan, *Angew. Chem., Int. Ed.*, 2024, **63**, e202411228.
96 X. Huang, H. Chen, M. Sun, J. Zhao, H. Teng, Y. Gao, J. Li, S. Lee and J. Tang, *Fuel*, 2024, **375**, 132613.
97 J. Zhao, M. Sun, W. Liu, H. Chen, X. Huang, Y. Gao, H. Teng and Z. Li, *Spectrochim. Acta, Part A*, 2024, **320**, 124629.
98 S. Li, M. Sun, X. Huang, H. Chen, J. Zhao and Z. Li, *Dalton Trans.*, 2024, **53**, 917–931.
99 Y. Li, X. Wang, B. Qiang, S. Xu, J. Gu, X. He and C. Li, *Green Chem.*, 2024, **26**, 6190–6199.
100 X. Huang, M. Sun, W. Sun, Z. Li, H. Chen and J. Zhao, *Int. J. Hydrogen Energy*, 2024, **55**, 581–591.
101 X. Huang, M. Sun, M. Humayun, S. Li, J. Zhao, H. Chen and Z. Li, *J. Alloys Compd.*, 2024, **976**, 173025.
102 C.-Y. Lee, K.-W. Sung and H.-J. Ahn, *J. Energy Storage*, 2025, **109**, 115064.
103 P. L. Krøll, M. B. Johansen, A. E. Hillers-Bendtsen, A. Ali El-Sayed, M. Dowds, A. Knakkergaard Knub, V. B. R. Pedersen, K. V. Mikkelsen and M. Brøndsted Nielsen, *Chem.–Eur. J.*, 2025, **31**, e202500360.
104 S. Shu, J. Yin, T. Song, Z. Chen, H. Dai, C. Wang and L. Duan, *ACS Appl. Mater. Interfaces*, 2025, **17**, 65639–65648.
105 P.-W. Chen, M.-I. Wu, Y.-H. Chen, M.-J. Wu, H.-W. Chang and Y.-C. Tsai, *Diamond Relat. Mater.*, 2025, 112872.
106 C. Min, J. Huang, H. Liang, A. Siddique and Z. Xu, *Polym. Compos.*, 2025, 1–13.
107 X. Tian, X. Ma, Q. Li, J. Si, D. Wang and J. Wu, *J. Alloys Compd.*, 2025, **1022**, 180072.
108 C. Zhang, L. Yu, S. Li, L. Cao, N. Nan, R. Xue, M. Gong, Y. Zhang, H. Zhang and X. Xiao, *Sens. Actuators, B*, 2025, **425**, 136972.
109 B. Kang, H. Liu and J. Y. Lee, *Phys. Chem. Chem. Phys.*, 2014, **16**, 974–980.
110 A. R. Puigdollers, G. Alonso and P. Gamallo, *Carbon*, 2016, **96**, 879–887.
111 N. V. R. Nulakani and V. Subramanian, *ACS Omega*, 2017, **2**, 6822–6830.
112 B. Mortazavi, M. Shahrokhi, M. E. Madjet, T. Hussain, X. Zhuang and T. Rabczuk, *J. Mater. Chem. C*, 2019, **7**, 3025–3036.
113 J. Deb, D. Paul and U. Sarkar, *J. Mater. Chem. C*, 2020, **8**, 16143–16150.
114 S. Borhani, M. Moradi, M. Pooriraj and B. Chameh, *Surf. Interfaces*, 2021, **26**, 101313.
115 T. A. Oliveira, P. V. Silva, A. Saraiva-Souza, J. G. da Silva Filho and E. C. Girão, *Phys. Rev. Mater.*, 2022, **6**, 016001.
116 J. M. de Sousa, W. H. d. S. Brandão, W. L. A. P. Silva, L. A. Ribeiro Júnior, D. S. Galvão and M. L. Pereira Júnior, *C*, 2023, **9**, 110.
117 C. Li, T. Li, G. Yu and W. Chen, *Molecules*, 2023, **28**, 3888.
118 C. Chowdhury, E. Karthikraja and V. Subramanian, *Phys. Chem. Chem. Phys.*, 2024, **26**, 25143–25155.
119 E. Unsal, A. Pecchia, A. Croy and G. Cuniberti, *arXiv*, 2025, preprint, arXiv:2505.21234, DOI: 10.48550/arXiv.2505.21234.
120 K. A. Lima, R. A. Alves, D. A. da Silva, F. L. Mendonça, M. L. Pereira and L. A. Ribeiro, *Phys. Chem. Chem. Phys.*, 2025, **27**, 8684–8691.
121 H. Pan, H. Zhang, H. Wang, J. Li, Y. Sun, W. Lu and X. Wang, *Appl. Surf. Sci.*, 2020, **513**, 145694.
122 B. Faria, N. Silvestre and J. N. Lopes, *Comput. Mater. Sci.*, 2020, **171**, 109233.
123 Q. Peng, W. Ji and S. De, *Phys. Chem. Chem. Phys.*, 2012, **14**, 13385–13391.
124 S. W. Cranford and M. J. Buehler, *Carbon*, 2011, **49**, 4111–4121.
125 Y. Zhang, Q. Pei and C. Wang, *Appl. Phys. Lett.*, 2012, **101**, 081909.
126 Y. Yang and X. Xu, *Comput. Mater. Sci.*, 2012, **61**, 83–88.
127 R. C. Andrew, R. E. Mapasha, A. M. Ukpong and N. Chetty, *Phys. Rev. B: Condens. Matter Mater. Phys.*, 2012, **85**, 125428.
128 J. Kang, J. Li, F. Wu, S.-S. Li and J.-B. Xia, *J. Phys. Chem. C*, 2011, **115**, 20466–20470.
129 Y. Wen, E. Gao, Z. Hu, T. Xu, H. Lu, Z. Xu and C. Li, *Nat. Commun.*, 2019, **10**, 2446.
130 S. Ajori, R. Ansari and M. Mirnezhad, *Mater. Sci. Eng., A*, 2013, **561**, 34–39.
131 T. Shao, B. Wen, R. Melnik, S. Yao, Y. Kawazoe and Y. Tian, *J. Chem. Phys.*, 2012, **137**, 194901.
132 Y.-Y. Zhang, Q.-X. Pei, Y.-W. Mai and Y.-T. Gu, *J. Phys. D: Appl. Phys.*, 2014, **47**, 425301.
133 B. Wu, X. Tang, J. Yin, W. Zhang, Y. Jiang, P. Zhang and Y. Ding, *Mater. Res. Express*, 2017, **4**, 025603.
134 K. Xiao, J. Li, X. Wu, H. Liu, C. Huang and Y. Li, *Carbon*, 2019, **144**, 72–80.
135 S. Georgantzinos, D. Katsareas and N. Anifantis, *Int. J. Mech. Sci.*, 2012, **55**, 85–94.
136 Y. Yang, Q. Cao, Y. Gao, S. Lei, S. Liu and Q. Peng, *RSC Adv.*, 2020, **10**, 1697–1703.
137 S. K. Georgantzinos and S. G. Siampanis, *Mater. Des.*, 2021, **202**, 109524.
138 B. Mortazavi and X. Zhuang, *FlatChem*, 2022, **36**, 100446.

139 P. V. Polyakova, R. T. Murzaev, D. S. Lisovenko and J. A. Baimova, *Comput. Mater. Sci.*, 2024, **244**, 113171.
140 K. J. Kotoko, K. Sodoga, Y. Shaidu, N. Seriani, S. Borah and K. Beltako, *J. Phys. Chem. C*, 2024, **128**, 17058–17072.
141 A. K. Akhunova and J. Baimova, *Surf. Interfaces*, 2025, 108307.
142 N. Galamba, C. Nieto de Castro and J. F. Ely, *J. Chem. Phys.*, 2007, **126**, 204511.
143 F. Font, W. Micou and F. Bresme, *Int. J. Heat Mass Transfer*, 2021, **164**, 120601.
144 L. Manjunatha, H. Takamatsu and J. J. Cannon, *Sci. Rep.*, 2021, **11**, 5597.
145 X. Tan, H. Shao, T. Hu, G. Liu, J. Jiang and H. Jiang, *Phys. Chem. Chem. Phys.*, 2015, **17**, 22872–22881.
146 P. Jiang, H. Liu, L. Cheng, D. Fan, J. Zhang, J. Wei, J. Liang and J. Shi, *Carbon*, 2017, **113**, 108–113.
147 Y. Zhang, Q. Pei and C. Wang, *Comput. Mater. Sci.*, 2012, **65**, 406–410.
148 T. Ouyang, Y. Chen, L.-M. Liu, Y. Xie, X. Wei and J. Zhong, *Phys. Rev. B: Condens. Matter Mater. Phys.*, 2012, **85**, 235436.
149 J. Wang, A.-J. Zhang and Y. Tang, *J. Appl. Phys.*, 2015, **118**, 195102.
150 M. Hu, Y. Jing and X. Zhang, *Phys. Rev. B: Condens. Matter Mater. Phys.*, 2015, **91**, 155408.
151 J. Zhang, Y. Cui and S. Wang, *Phys. E*, 2017, **90**, 116–122.
152 G. Narang, D. Bansal, S. Joarder, P. Singh, L. Kumar, V. Mishra, S. Singh, K. Tumba and K. Kumari, *FlatChem*, 2023, **40**, 100517.
153 L. Sun, P. Jiang, H. Liu, D. Fan, J. Liang, J. Wei, L. Cheng, J. Zhang and r. Shi, *Carbon*, 2015, **90**, 255–259.
154 J. Li and J. Zhang, *Nanoscale*, 2024, **16**, 17992–18004.
155 J. de Lima, L. V. Bastos and C. F. Woellner, *Comput. Mater. Sci.*, 2025, **250**, 113728.
156 I. M. Felix, R. M. Tromer, L. D. Machado, D. S. Galvão, L. A. Ribeiro Jr and M. L. Pereira Jr, *Int. J. Heat Mass Transfer*, 2025, **241**, 126746.
157 C. Huang, Y. Li, N. Wang, Y. Xue, Z. Zuo, H. Liu and Y. Li, *Chem. Rev.*, 2018, **118**, 7744–7803.
158 D. Malko, C. Neiss, F. Vines and A. Görling, *Phys. Rev. Lett.*, 2012, **108**, 086804.
159 X.-L. Sheng, C. Chen, H. Liu, Z. Chen, Z.-M. Yu, Y. Zhao and S. A. Yang, *Phys. Rev. Lett.*, 2019, **123**, 256402.
160 S. S. Sani, H. Mousavi, M. Asshabi and S. Jalilvand, *ECS J. Solid State Sci. Technol.*, 2020, **9**, 031003.
161 B. G. Kim and H. J. Choi, *Phys. Rev. B: Condens. Matter Mater. Phys.*, 2012, **86**, 115435.
162 H. Huang, W. Duan and Z. Liu, *New J. Phys.*, 2013, **15**, 023004.
163 J. Li and Y. Han, *Giant*, 2023, **13**, 100140.
164 S. Guo, H. Yan, F. Wu, L. Zhao, P. Yu, H. Liu, Y. Li and L. Mao, *Anal. Chem.*, 2017, **89**, 13008–13015.
165 X. Gao, H. Liu, D. Wang and J. Zhang, *Chem. Soc. Rev.*, 2019, **48**, 908–936.
166 X. Li, B.-H. Li, Y.-B. He and F.-Y. Kang, *New Carbon Mater.*, 2020, **35**, 619–629.
167 A. León and M. Pacheco, *Chem. Phys. Lett.*, 2015, **620**, 67–72.
168 Q. Zheng, G. Luo, Q. Liu, R. Quhe, J. Zheng, K. Tang, Z. Gao, S. Nagase and J. Lu, *Nanoscale*, 2012, **4**, 3990–3996.
169 R. Matsuoka, R. Sakamoto, K. Hoshiko, S. Sasaki, H. Masunaga, K. Nagashio and H. Nishihara, *J. Am. Chem. Soc.*, 2017, **139**, 3145–3152.
170 X. Gao, Y. Zhu, D. Yi, J. Zhou, S. Zhang, C. Yin, F. Ding, S. Zhang, X. Yi and J. Wang, *Sci. Adv.*, 2018, **4**, eaat6378.
171 P. Yan, T. Ouyang, C. He, J. Li, C. Zhang, C. Tang and J. Zhong, *Nanoscale*, 2021, **13**, 3564–3571.
172 Q. Yue, S. Chang, J. Kang, S. Qin and J. Li, *J. Phys. Chem. C*, 2013, **117**, 14804–14811.
173 F. C. Rodrigues, N. Silvestre and A. M. Deus, *Comput. Mater. Sci.*, 2017, **134**, 171–183.
174 S. A. Hernandez and A. F. Fonseca, *Diamond Relat. Mater.*, 2017, **77**, 57–64.
175 S. W. Cranford, D. B. Brommer and M. J. Buehler, *Nanoscale*, 2012, **4**, 7797–7809.
176 J. Chen, J. Xi, D. Wang and Z. Shuai, *J. Phys. Chem. Lett.*, 2013, **4**, 1443–1448.
177 X. Hou, Z. Xie, C. Li, G. Li and Z. Chen, *Materials*, 2018, **11**, 188.
178 J.-M. Ducere, C. Lepetit and R. Chauvin, *J. Phys. Chem. C*, 2013, **117**, 21671–21681.
179 J. Qu, H. Zhang, J. Li, S. Zhao and T. Chang, *Carbon*, 2017, **120**, 350–357.
180 H. Zhao, K. Min and N. R. Aluru, *Nano Lett.*, 2009, **9**, 3012–3015.
181 X. Wei, B. Fragneaud, C. A. Marianetti and J. W. Kysar, *Phys. Rev. B: Condens. Matter Mater. Phys.*, 2009, **80**, 205407.
182 W. Li, *Eur. Phys. J. Plus*, 2024, **139**, 813.
183 X. Chen, P. Gao, L. Guo, Y. Wen, Y. Zhang and S. Zhang, *J. Phys. Chem. Solids*, 2017, **105**, 61–65.
184 M. Zhang, X. Wang, H. Sun, N. Wang, Q. Lv, W. Cui, Y. Long and C. Huang, *Sci. Rep.*, 2017, **7**, 11535.
185 X. Zhan, H. Kang, F. Qian, L. Xu, Y. Zheng and Z. Huang, *J. Alloys Compd.*, 2023, **940**, 168693.
186 H.-B. Li, Z.-G. Shao, C.-L. Wang and L. Yang, *Phys. Chem. Chem. Phys.*, 2023, **25**, 28141–28149.
187 H. Rezania, E. Nourian, M. Abdi and B. Astinchap, *RSC Adv.*, 2023, **13**, 7988–7999.
188 H. Kang, Y. Zhong, P. Gao, X. Liang, H. Qiu and Y. Zheng, *RSC Adv.*, 2024, **14**, 37628–37632.
189 L. Zhang, Y. Hao, Y. Yang, J. Chen and L. Zhang, *J. Mater. Chem. C*, 2025, **13**, 884–891.
190 H.-B. Li and Z.-G. Shao, *Phys. Rev. B*, 2025, **111**, 214420.
191 Y.-P. Zheng, Q. Feng, N.-J. Tang and Y.-W. Du, *New Carbon Mater.*, 2018, **33**, 516–521.
192 G.-R. Xu, J.-M. Xu, H.-C. Su, X.-Y. Liu, H.-L. Zhao, H.-J. Feng and R. Das, *Desalination*, 2019, **451**, 18–34.
193 M. Xue, H. Qiu and W. Guo, *Nanotechnology*, 2013, **24**, 505720.
194 R. M. Tromer, M. L. Pereira Júnior, K. A. L. Lima, A. F. Fonseca, L. R. da Silva, D. S. Galvão and L. A. Ribeiro Junior, *J. Phys. Chem. C*, 2023, **127**, 12226–12234.
195 L. Nie, Y. Zhao, P. Guo, W. Wang, Z. Jin, D. Zhang, X. Li, Y. Guo, T. Chai and R. Liu, *Appl. Opt.*, 2023, **62**, 5023–5027.

196 R. Majidi, *Mater. Today Commun.*, 2024, **38**, 107641.
197 I. M. Felix, J. M. Pontes, D. S. Gomes, T. B. Guerra, S. Azevedo, L. D. Machado, L. C. Gomes and R. M. Tromer, *Phys. E*, 2025, **167**, 116163.
198 A. E. Hillers-Bendtsen, F. Ø. Kjeldal, N. M. Høyer and K. V. Mikkelsen, *J. Phys. Chem. A*, 2025, **129**, 10039–10054.
199 S. Ali, B. Ali, S. Abdulkarim and M. Sun, *Chem. Phys.*, 2025, 112847.
200 K. Lin, H. Huang, J. Zhang, Q. Zhong, W. Wang and S. Zhang, *J. Mater. Chem. C*, 2025, **13**, 9768–9778.
201 H. Bai, Y. Zhu, W. Qiao and Y. Huang, *RSC Adv.*, 2011, **1**, 768–775.
202 A. Enyashin and A. Ivanovskii, *Superlattices Microstruct.*, 2013, **55**, 75–82.
203 D. A. Solis, D. D. Borges, C. F. Woellner and D. S. Galvao, *ACS Appl. Mater. Interfaces*, 2018, **11**, 2670–2676.
204 H. Bao, L. Wang, C. Li and J. Luo, *ACS Appl. Mater. Interfaces*, 2018, **11**, 2717–2729.
205 C. Lu, Y. Yang, J. Wang, R. Fu, X. Zhao, L. Zhao, Y. Ming, Y. Hu, H. Lin and X. Tao, *Nat. Commun.*, 2018, **9**, 752.
206 F. De Boni, R. Pilot, A. Milani, V. V. Ivanovskaya, R. J. Abraham, S. Casalini, D. Pedron, C. S. Casari, M. Sambi and F. Sedona, *Nanoscale*, 2024, **16**, 11211–11222.
207 C. Zhu, H. Li, X. C. Zeng and S. Meng, *arXiv*, 2013, preprint, arXiv:1307.0208, DOI: 10.48550/arXiv.1307.0208.
208 M. Bartolomei, E. Carmona-Novillo, M. I. Hernández, J. Campos-Martínez, F. Pirani, G. Giorgi and K. Yamashita, *J. Phys. Chem. Lett.*, 2014, **5**, 751–755.
209 J. Azamat, N. B. Baghbani and H. Erfan-Niya, *J. Membr. Sci.*, 2020, **604**, 118079.
210 D. Cohen-Tanugi and J. C. Grossman, *Desalination*, 2015, **366**, 59–70.
211 J. Kou, X. Zhou, Y. Chen, H. Lu, F. Wu and J. Fan, *J. Chem. Phys.*, 2013, **139**, 064705.
212 S. Lin and M. J. Buehler, *Nanoscale*, 2013, **5**, 11801–11807.
213 C. Zhu, H. Li, X. C. Zeng, E. Wang and S. Meng, *Sci. Rep.*, 2013, **3**, 3163.
214 X. Zhang and J.-G. Gai, *RSC Adv.*, 2015, **5**, 68109–68116.
215 B. Wu, H. Jin, J. Yin, W. Zhang, X. Tang, P. Zhang and Y. Ding, *Carbon*, 2017, **123**, 688–694.
216 S. Bagheri, A. Shameli, M. Darvishi and G. Fakhrpour, *Phys. E*, 2017, **90**, 123–130.
217 M. Akhavan, J. Schofield and S. Jalili, *Phys. Chem. Chem. Phys.*, 2018, **20**, 13607–13615.
218 R. Liu, J. Zhou, X. Gao, J. Li, Z. Xie, Z. Li, S. Zhang, L. Tong, J. Zhang and Z. Liu, *Adv. Electron. Mater.*, 2017, **3**, 1700122.
219 N. B. Baghbani, J. Azamat, H. Erfan-Niya, S. Majidi and L. Khazini, *J. Mol. Graphics Modell.*, 2020, **101**, 107729.
220 G. Guillen and E. M. Hoek, *Chem. Eng. J.*, 2009, **149**, 221–231.
221 S. P. Surwade, S. N. Smirnov, I. V. Vlassiouk, R. R. Unocic, G. M. Veith, S. Dai and S. M. Mahurin, *Nat. Nanotechnol.*, 2015, **10**, 459–464.
222 M. Hosseini, J. Azamat and H. Erfan-Niya, *Appl. Surf. Sci.*, 2018, **427**, 1000–1008.
223 E. Y. Ang, T. Y. Ng, J. Yeo, R. Lin, Z. Liu and K. R. Geethalakshmi, *J. Membr. Sci.*, 2019, **581**, 383–392.
224 S. Majidi, H. Erfan-Niya, J. Azamat, E. R. Cruz-Chú and J. H. Walther, *J. Mol. Graphics Modell.*, 2023, **118**, 108337.
225 M. Raju, P. B. Govindaraju, A. C. Van Duin and M. Ihme, *Nanoscale*, 2018, **10**, 3969–3980.
226 M. Jahangirzadeh, J. Azamat and H. Erfan-Niya, *Comput. Mater. Sci.*, 2022, **203**, 111126.
227 A. Nematipour, E. Houshfar and M. M. S. Fakhrabadi, *Appl. Surf. Sci.*, 2021, **559**, 149977.
228 S. Xie, C. Pan, Y. Yao, X. Yu, Z. Xu, W. Yuan, Y. Zhang, N. Guo, X. Li and X. Mao, *Proc. Natl. Acad. Sci. U. S. A.*, 2023, **120**, e2221002120.
229 Q. He, X. Li, W. Chai, L. Chen and X. Mao, *J. Hazard. Mater.*, 2024, **467**, 133711.
230 X.-F. Yang, A. Wang, B. Qiao, J. Li, J. Liu and T. Zhang, *Acc. Chem. Res.*, 2013, **46**, 1740–1748.
231 A. Krasheninnikov, P. Lehtinen, A. S. Foster, P. Pyykkö and R. M. Nieminen, *Phys. Rev. Lett.*, 2009, **102**, 126807.
232 K. Srinivasu and S. K. Ghosh, *J. Phys. Chem. C*, 2013, **117**, 26021–26028.
233 P. Wu, P. Du, H. Zhang and C. Cai, *Phys. Chem. Chem. Phys.*, 2015, **17**, 1441–1449.
234 D. Ma, T. Li, Q. Wang, G. Yang, C. He, B. Ma and Z. Lu, *Carbon*, 2015, **95**, 756–765.
235 X. Gao, Y. Zhou, Z. Cheng, Y. Tan, S. Liu and Z. Shen, *Int. J. Hydrogen Energy*, 2019, **44**, 27421–27428.
236 X. Gao, Y. Zhou, S. Liu, Z. Cheng, Y. Tan and Z. Shen, *Appl. Surf. Sci.*, 2020, **502**, 144155.
237 L. Fu, R. Wang, C. Zhao, J. Huo, C. He, K.-H. Kim and W. Zhang, *Chem. Eng. J.*, 2021, **414**, 128857.
238 W. Zhang, Y.-J. Gao, Q.-J. Fang, J.-K. Pan, X.-C. Zhu, S.-W. Deng, Z.-H. Yao, G.-L. Zhuang and J.-G. Wang, *J. Colloid Interface Sci.*, 2021, **599**, 58–67.
239 Z. Zhang, S. Qi, X. Song, J. Wang, W. Zhang and M. Zhao, *Appl. Surf. Sci.*, 2021, **553**, 149464.
240 L. Jasin Arachchige, A. Dong, T. Wang, H. Li, X. L. Zhang, F. Wang, H. Su and C. Sun, *ACS Appl. Nano Mater.*, 2021, **4**, 12006–12016.
241 F. Ullah, K. Ayub and T. Mahmood, *Int. J. Hydrogen Energy*, 2021, **46**, 37814–37823.
242 B. Kang, Y. Yuan, Y. Lv, H. Ai and J. Y. Lee, *Chem. Eng. J.*, 2022, **428**, 131318.
243 M. Guo, M. Ji and W. Cui, *Appl. Surf. Sci.*, 2022, **592**, 153237.
244 Q. Li, Y. Chen, F. Du, X. Cui and L. Dai, *Appl. Catal., B*, 2022, **304**, 120959.
245 S.-L. Li, Q. Li, Y. Chen, Y. Zhao and L.-Y. Gan, *Appl. Surf. Sci.*, 2022, **605**, 154828.
246 X. Liu, G. Li, J. Liu and J. Zhao, *Mol. Catal.*, 2022, **531**, 112706.
247 T. Li, Y. Wu and M. Pei, *J. Alloys Compd.*, 2022, **908**, 164675.
248 W. Song, Z. Fu, P. Ma, X. Liu, Y. Guo, L. Fu and C. He, *Appl. Surf. Sci.*, 2023, **617**, 156550.
249 S. H. Talib, B. Bashir, M. A. Khan, B. Ali, S. Mohamed, A. Qurashi and J. Li, *Energy Environ. Mater.*, 2024, **7**, e12723.
250 T. Liu, T. Xu, T. Li and Y. Jing, *J. Am. Chem. Soc.*, 2024, **146**, 24133–24140.
251 M. Shao and Y. Shao, *J. Mater. Chem. A*, 2025, **13**, 22066–22073.

252 J. Ye, Z. He, L. Ma, K. Chen, Y. Wu, H. Li, J. Rong, Z. Liu and X. Yu, *Mater. Today Commun.*, 2025, 113255.
253 S. Zhou, S. Cao, S. Wei, Z. Wang, H. Chen, X. Lin, X. Chen, S. Liu and X. Lu, *Appl. Mater. Today*, 2021, **25**, 101245.
254 N. Yang, Y. Liu, H. Wen, Z. Tang, H. Zhao, Y. Li and D. Wang, *ACS Nano*, 2013, **7**, 1504–1512.
255 S. Ali, Z. Lian and B. Li, *ACS Appl. Nano Mater.*, 2021, **4**, 6152–6159.
256 J.-C. Liu, H. Xiao, X.-K. Zhao, N.-N. Zhang, Y. Liu, D.-H. Xing, X. Yu, H.-S. Hu and J. Li, *CCS Chem.*, 2023, **5**, 152–163.
257 D. Chodvadiya, B. Chakraborty and P. K. Jha, *Int. J. Hydrogen Energy*, 2023, **48**, 18326–18337.
258 M. Sajjad, S. S. Nair, Y. A. Samad and N. Singh, *Sci. Rep.*, 2023, **13**, 9123.
259 M. Ren, X. Guo, S. Zhang and S. Huang, *Adv. Funct. Mater.*, 2023, **33**, 2213543.
260 K. S. Joseph, B. Chakraborty and S. Dabhi, *Surf. Interfaces*, 2025, **56**, 105561.
261 F. Motaghi and H. Mohammadi-Manesh, *J. Serb. Chem. Soc.*, 2025, **90**, 609–621.
262 G. Jafari and A. Reisi-Vanani, *Int. J. Hydrogen Energy*, 2025, **109**, 424–435.
263 J. Xu, Y. Wang, J. Lu, X. Li, X. Wang and J. Yang, *Vacuum*, 2021, **183**, 109847.
264 P. Wu, P. Du, H. Zhang and C. Cai, *J. Phys. Chem. C*, 2012, **116**, 20472–20479.
265 Y. Lv, G. Chen, R. Ma, J. Y. Lee and B. Kang, *Fuel*, 2024, **357**, 130017.
266 Y. Lv, B. Kang, Y. Yuan, G. Chen and J. Y. Lee, *Chem. Eng. J.*, 2022, **430**, 133126.
267 Y. Lv, B. Kang, G. Chen, Y. Yuan, J. Ren and J. Y. Lee, *Appl. Surf. Sci.*, 2023, **613**, 156084.
268 F. He, C. Xing and Y. Xue, *J. Catal.*, 2021, **395**, 129–135.
269 A. VG, R. Batra and B. Nanda, *ACS Catal.*, 2024, **14**, 8874–8888.
270 P. Daghooghi and H. Tavakol, *Fullerenes, Nanotubes Carbon Nanostruct.*, 2025, **33**, 370–384.
271 A. A. Khan, M. D. Esrafili, F. Ali, R. Ahmad and I. Ahmad, *J. Mol. Graphics Modell.*, 2022, **114**, 108186.
272 C. Quej, C. Cab, G. Canto, J. Medina and A. Tapia, *J. Phys. Chem. Solids*, 2025, **200**, 112596.
273 H. Yu, Y. Xue, B. Huang, L. Hui, C. Zhang, Y. Fang, Y. Liu, Y. Zhao, Y. Li and H. Liu, *iScience*, 2019, **11**, 31–41.
274 T. Liu, X. Hao, J. Liu, P. Zhang, J. Chang, H. Shang and X. Liu, *Int. J. Mol. Sci.*, 2023, **24**, 16813.
275 T. Wang and Z. Jin, *J. Mater. Sci. Technol.*, 2023, **155**, 132–141.
276 W. Li, Y. Zhang, Y. Wang, W. Ran, Q. Guan, W. Yi, L. Zhang, D. Zhang, N. Li and T. Yan, *Appl. Catal., B*, 2024, **340**, 123267.
277 Y. Zheng, Y. Xue, Y. Gao, S. Chen, S. Chen and Y. Li, *ChemPhysMater*, 2025, **4**, 124–130.
278 H. Ali, O. Iqbal, M. Sadiq, J. U. Hassan, B. Al Alwan, A. El Jery, A. M. Abu-Dief, R. El-Kasaby, A. Hayat and D. Yue, *Renewable Sustainable Energy Rev.*, 2025, **215**, 115570.
279 M. Khantha, N. A. Cordero, J. Alonso, M. Cawkwell and L. A. Girifalco, *Phys. Rev. B: Condens. Matter Mater. Phys.*, 2008, **78**, 115430.
280 H. Zhang, M. Zhao, X. He, Z. Wang, X. Zhang and X. Liu, *J. Phys. Chem. C*, 2011, **115**, 8845–8850.
281 C. Sun and D. J. Searles, *J. Phys. Chem. C*, 2012, **116**, 26222–26226.
282 H. Zhang, Y. Xia, H. Bu, X. Wang, M. Zhang, Y. Luo and M. Zhao, *J. Appl. Phys.*, 2013, **113**, 044309.
283 R. Lu, D. Rao, Z. Meng, X. Zhang, G. Xu, Y. Liu, E. Kan, C. Xiao and K. Deng, *Phys. Chem. Chem. Phys.*, 2013, **15**, 16120–16126.
284 H. J. Hwang, J. Koo, M. Park, N. Park, Y. Kwon and H. Lee, *J. Phys. Chem. C*, 2013, **117**, 6919–6923.
285 M. Makaremi, B. Mortazavi and C. V. Singh, *Appl. Mater. Today*, 2018, **10**, 115–121.
286 Q. Zhang, C. Tang, W. Zhu and C. Cheng, *J. Phys. Chem. C*, 2018, **122**, 22838–22848.
287 J. Ma, Y. Yuan, S. Wu, J. Y. Lee and B. Kang, *Appl. Surf. Sci.*, 2020, **531**, 147343.
288 Y.-T. Yan, Z.-G. Shao, C.-L. Wang and L. Yang, *Chem. Phys. Lett.*, 2022, **804**, 139897.
289 R. Momen, R. Rezaee, B. Azizi, S. Rezaee, H. Hou and X. Ji, *Eur. Phys. J. Plus*, 2022, **137**, 360.
290 R. E. Dias and A. L. Magalhaes, *Comput. Theor. Chem.*, 2024, **1233**, 114494.
291 M. Bahrami, F. Momen, F. Shayeganfar and A. Ramazani, *Comput. Mater. Sci.*, 2024, **240**, 113017.
292 H. Huang, K. Li, X. Fan, D. J. Singh and W. Zheng, *J. Mater. Chem. A*, 2019, **7**, 25609–25618.
293 T. Singh, J. R. Choudhuri and M. K. Rana, *Nanotechnology*, 2022, **34**, 045404.
294 R. Majidi and A. I. Ayesh, *Mol. Simul.*, 2023, **49**, 1044–1050.
295 L. Wu, H. Zhang and J. Zhou, *Mol. Simul.*, 2021, **47**, 326–333.
296 I. Muhammad, U. Younis, W. Wu, H. Xie, A. Khaliq and Q. Sun, *J. Power Sources*, 2020, **480**, 228876.
297 S. B. Mishra, A. VG, S. Ramaprabhu and B. Nanda, *ACS Appl. Energy Mater.*, 2021, **4**, 7786–7799.
298 S. B. Mishra, S. Ramaprabhu and B. Nanda, *Nanoscale Adv.*, 2022, **4**, 3870–3882.
299 J. He, N. Wang, Z. Cui, H. Du, L. Fu, C. Huang, Z. Yang, X. Shen, Y. Yi and Z. Tu, *Nat. Commun.*, 2017, **8**, 1172.
300 B. Hua, H. Kang, J. Zhong, X. Zhan, L. Xu, J. Li, Y. Zheng and Z. Zheng, *ACS Appl. Mater. Interfaces*, 2021, **13**, 34332–34340.
301 J. Li, Y. Yi, X. Zuo, B. Hu, Z. Xiao, R. Lian, Y. Kong, L. Tong, R. Shao and J. Sun, *ACS Nano*, 2022, **16**, 3163–3172.
302 Z. Man, P. Li, S. Liu, Y. Zhang, X. Zhu, S. Ye, W. Lu, W. Chen, G. Wu and N. Bao, *ACS Appl. Mater. Interfaces*, 2023, **15**, 26910–26917.
303 K. Eeso, B. R. Wygant, Z. Chen, A. Sarswat, T. N. Lambert and N. Liu, *Chem. Commun.*, 2024, **60**, 14232–14235.
304 X. Gao, X. Zheng, Y. Ye, H. K. Lee, P. Zhang, A. Cui, X. Xiao, Y. Yang and Y. Cui, *Nano Lett.*, 2024, **24**, 3044–3050.
305 Z. Wang, Z. Zhao, T. Li, Y. Yuan, X. Shen and J. Zhou, *J. Power Sources*, 2025, **638**, 236609.

306 D.-e. Jiang, V. R. Cooper and S. Dai, *Nano Lett.*, 2009, **9**, 4019–4024.
307 D. Cohen-Tanugi and J. C. Grossman, *Nano Lett.*, 2012, **12**, 3602–3608.
308 M. Alaghemandi, *Chem. Phys. Lett.*, 2015, **629**, 65–69.
309 R. Jafarzadeh, J. Azamat and H. Erfan-Niya, *Pet. Sci. Technol.*, 2019, **37**, 2043–2048.
310 C. Ning, Y. Zhang, J. Wang, H. Gao, C. Xiao, Z. Meng and H. Dong, *Phys. Chem. Chem. Phys.*, 2020, **22**, 19492–19501.
311 M. Luo, Y. Qiao, Y. Wang, Q. Yin and G. Zhou, *Polym. Compos.*, 2023, **44**, 8974–8987.
312 K. Azizi, S. M. Vaez Allaei, A. Fathizadeh, A. Sadeghi and M. Sahimi, *Sci. Rep.*, 2021, **11**, 16325.
313 Y. Jiao, A. Du, M. Hankel, Z. Zhu, V. Rudolph and S. C. Smith, *Chem. Commun.*, 2011, **47**, 11843–11845.
314 H. Zhang, X. He, M. Zhao, M. Zhang, L. Zhao, X. Feng and Y. Luo, *J. Phys. Chem. C*, 2012, **116**, 16634–16638.
315 S. W. Cranford and M. J. Buehler, *Nanoscale*, 2012, **4**, 4587–4593.
316 X. Tan, L. Kou, H. A. Tahini and S. C. Smith, *Mol. Simul.*, 2016, **42**, 573–579.
317 Z. Meng, X. Zhang, Y. Zhang, H. Gao, Y. Wang, Q. Shi, D. Rao, Y. Liu, K. Deng and R. Lu, *ACS Appl. Mater. Interfaces*, 2016, **8**, 28166–28170.
318 P. Sang, L. Zhao, J. Xu, Z. Shi, S. Guo, Y. Yu, H. Zhu, Z. Yan and W. Guo, *Int. J. Hydrogen Energy*, 2017, **42**, 5168–5176.
319 L. Zhao, P. Sang, S. Guo, X. Liu, J. Li, H. Zhu and W. Guo, *Appl. Surf. Sci.*, 2017, **405**, 455–464.
320 Z. Zhou, Y. Tan, Q. Yang, A. Bera, Z. Xiong, M. Yagmurcukardes, M. Kim, Y. Zou, G. Wang and A. Mishchenko, *Nat. Commun.*, 2022, **13**, 4031.
321 S. Mahnaee, M. J. López and J. A. Alonso, *Phys. Chem. Chem. Phys.*, 2024, **26**, 15916–15926.
322 M. A. Rafiei, J. Campos-Martínez, M. Bartolomei, F. Pirani, A. Maghari and M. I. Hernández, *Phys. Chem. Chem. Phys.*, 2024, **26**, 24553–24563.
323 Y. Wang, G. Sun, J. Guan, Y.-Q. Li, Y. Yang, M. Zhao, W. Li and Y. Qu, *ACS Appl. Nano Mater.*, 2024, **7**, 27355–27364.
324 Y. B. Apriliyanto, N. Faginas Lago, A. Lombardi, S. Evangelisti, M. Bartolomei, T. Leininger and F. Pirani, *J. Phys. Chem. C*, 2018, **122**, 16195–16208.
325 P. Rezaee and H. R. Naeij, *Carbon*, 2020, **157**, 779–787.
326 S. Nikmanesh, R. Safaiee and M. H. Sheikhi, *Mater. Chem. Phys.*, 2021, **257**, 123808.
327 P. Zhang, Q. Song, J. Zhuang and X.-J. Ning, *Chem. Phys. Lett.*, 2017, **689**, 185–189.
328 S. Lakshmy, N. Kalarikkal and B. Chakraborty, *J. Phys. D: Appl. Phys.*, 2023, **56**, 495104.
329 M. B. Singh, G. Narang and P. Singh, *Indian J. Microbiol.*, 2025, **65**, 359–374.
330 S. Alamri, C.-Y. Hsu, A. M. Al-Ma'abreh, S. Alawideh, A. A. Lagum, A. A. Duhduh, A. A. Rajhi and M. M. Kadhim, *Diamond Relat. Mater.*, 2023, **139**, 110303.
331 M. T. Ahmed, D. Roy, A. A. Roman, S. Islam and F. Ahmed, *Langmuir*, 2024, **40**, 15332–15352.
332 L. Zhang, B. He, Y. Li, J. Yun, L. Yao, H. Zhao, J. Yan, W. Zhao and Z. Zhang, *ACS Sens.*, 2025, **10**, 2499–2509.
333 M. A. Sakr, M. A. Saad, V. A. Saroka, H. Abdelsalam and Q. Zhang, *J. Fluoresc.*, 2024, **34**, 945–960.
334 T. Movlarooy and A. Nooranbjar, *Diamond Relat. Mater.*, 2024, **148**, 111471.
335 Y. Zhang, Z. Xia, G. Gui, P. Zhang, Q. Li and L. Meng, *Chemosensors*, 2022, **10**, 485.
336 U. Kumar, P.-Y. Wu, C.-E. Lin, Z.-Y. Deng, R.-J. Wu, K.-L. Chen, W.-M. Huang and C.-H. Wu, *ACS Sens.*, 2025, **10**, 7508–7520.
337 J. Zhang, W. Li, C. Pan, W. Ma, P. Yu and L. Mao, *ChemPhysMater*, 2025, **4**, 179–186.
338 C. Zhang, L. Yu, S. Li, R. Xue, L. Cao, N. Nan, X. Xiao, S. Yang, C. Li and X. Fan, *Sens. Actuators, B*, 2025, 138048.
339 P. Xu, N. Na and A. Mohamadi, *Comput. Theor. Chem.*, 2020, **1190**, 112996.
340 M. M. Kadhim, A. Taha, R. K. Mahal, S. K. Hachim, S. A. Abdullaha and A. M. Rheima, *J. Mol. Model.*, 2023, **29**, 129.
341 S. Lakshmy, A. Kundu, N. Kalarikkal and B. Chakraborty, *J. Mater. Chem. B*, 2022, **10**, 5958–5967.
342 S. Lakshmy, A. Kundu, N. Kalarikkal and B. Chakraborty, *J. Phys. D: Appl. Phys.*, 2023, **56**, 055402.
343 R. Majidi and A. Karami, *Phys. E*, 2013, **54**, 177–180.
344 Y. Guo, Z. Chen, W. Wu, Y. Liu and Z. Zhou, *Appl. Surf. Sci.*, 2018, **455**, 484–491.
345 S. Madhumitha, V. Nagarajan and R. Chandiramouli, *Comput. Theor. Chem.*, 2019, **1163**, 112514.
346 M. Ebadi and A. Reisi-Vanani, *Phys. E*, 2021, **125**, 114425.
347 C. Zhang and M. Derakhshandeh, *Comput. Theor. Chem.*, 2021, **1204**, 113380.
348 C. Quej, J. Medina, G. Canto, M. Casais-Molina, C. Cab and A. Tapia, *Comput. Mater. Sci.*, 2024, **232**, 112677.
349 Z. Felegari and S. Hamedani, *Results Phys.*, 2017, **7**, 2626–2631.
350 T. Vazhappilly and T. K. Ghanty, *Mater. Today Commun.*, 2020, **22**, 100738.
351 E. Vessally, M. Vali, A. Hosseinian, M. R. P. Heravi and A. Bekhradnia, *Phys. Lett. A*, 2020, **384**, 126479.
352 F. Mofidi and A. Reisi-Vanani, *Appl. Surf. Sci.*, 2020, **507**, 145134.
353 W. Yang, B. Zhao, C. Li, P. Guo, M. Li, X. Ge, M. Zhang, X. Guan and J. Wang, *Appl. Surf. Sci.*, 2022, **601**, 154083.
354 X. Zeng, R. Zhang, R. Li, R. Li, H. Cui, C. Zhao, S. Zhang and L. Jin, *Phys. Chem. Chem. Phys.*, 2024, **26**, 25208–25221.
355 R. Li, X. Zeng, M. Lv, R. Zhang, S. Zhang, T. Zhang, X. Yu, C. Li, L. Jin and C. Zhao, *Phys. Chem. Chem. Phys.*, 2024, **26**, 5558–5568.
356 C. Li, J. Li, F. Wu, S.-S. Li, J.-B. Xia and L.-W. Wang, *J. Phys. Chem. C*, 2011, **115**, 23221–23225.
357 H. J. Hwang, Y. Kwon and H. Lee, *J. Phys. Chem. C*, 2012, **116**, 20220–20224.
358 C. Ataca, E. Aktürk and S. Ciraci, *Phys. Rev. B: Condens. Matter Mater. Phys.*, 2009, **79**, 041406.
359 K. Srinivasu and S. K. Ghosh, *J. Phys. Chem. C*, 2012, **116**, 5951–5956.
360 Y. Guo, K. Jiang, B. Xu, Y. Xia, J. Yin and Z. Liu, *J. Phys. Chem. C*, 2012, **116**, 13837–13841.

361 S. Kumar and T. J. Dhilip Kumar, *ACS Appl. Mater. Interfaces*, 2017, **9**, 28659–28666.
362 T. Hussain, B. Mortazavi, H. Bae, T. Rabczuk, H. Lee and A. Karton, *Carbon*, 2019, **147**, 199–205.
363 Y. Liu, S. Gao, F. Lu, A. Yu, S. Song, H. Shi, Y. Mai and B. Liao, *Int. J. Hydrogen Energy*, 2020, **45**, 24938–24946.
364 M. Singh, A. Shukla and B. Chakraborty, *Nanotechnology*, 2022, **33**, 405406.
365 J. Sarma, R. Chowdhury and R. Jayaganthan, *Nano*, 2014, **9**, 1450032.
366 H. Khan, M. M. Islam, R. I. Roya, S. N. Azad and M. Alam, *Micromachines*, 2023, **14**, 1385.
367 Y. Pan, Y. Wang, L. Wang, H. Zhong, R. Quhe, Z. Ni, M. Ye, W.-N. Mei, J. Shi and W. Guo, *Nanoscale*, 2015, **7**, 2116–2127.
368 B. Rouzkhash, A. Salehi and M. T. Ahmadi, *J. Comput. Electron.*, 2022, **21**, 1098–1107.
369 J. Huang and J. Kang, *J. Phys.: Condens. Matter*, 2022, **34**, 165301.
370 Y. Li, M. Zhang, X. Hu, X. Fan, L. Yu and C. Huang, *J. Phys. Chem. Lett.*, 2020, **11**, 1998–2005.
371 Z. Yang, X. Ren, X. Ma, Y. Song, X. Hu, M. Zhang, Y. Li, C. Xie, X. Li and J. Li, *Mater. Chem. Front.*, 2021, **5**, 7993–8001.
372 Z. Ghafary, A. Salimi and R. Hallaj, *ACS Biomater. Sci. Eng.*, 2022, **8**, 3986–4001.
373 Y. Liu, Z. Shao, X. Yu, D. Guo, S. Wang, L. Bian, Y. Chen, H. Liu, H. Ling and L. Xie, *Org. Electron.*, 2024, **128**, 107027.
374 M. Luo, Q. Yin, B. Jiang and G. Zhou, *Macromol. Theory Simul.*, 2022, **31**, 2100093.
375 M. Wang, M. Liao, L. Li, M. Li, Y. Chen, X. Hou, C. Yan, N. Jiang and J. Yu, *2D Mater.*, 2020, **7**, 035007.
376 T. Zheng, Y. Gao, X. Deng, H. Liu, J. Liu, R. Liu, J. Shao, Y. Li and L. Jia, *ACS Appl. Mater. Interfaces*, 2018, **10**, 32946–32954.
377 K. Khan, A. K. Tareen, M. Iqbal, A. Mahmood, N. Mahmood, Z. Shi, J. Yin, D. Qing, C. Ma and H. Zhang, *J. Mater. Chem. B*, 2021, **9**, 9461–9484.
378 L.-X. Zhao, Y.-G. Fan, X. Zhang, C. Li, X.-Y. Cheng, F. Guo and Z.-Y. Wang, *J. Nanobiotechnol.*, 2025, **23**, 169.
379 W. Xie, Y. Zhang, Q. Xu, G. Zhong, J. Lin, H. He, Q. Du, H. Tan, M. Chen and Z. Wu, *Int. J. Nanomed.*, 2024, 3957–3972.
380 Z. Wang, H. Wang, X. Zhang, Y. Yuan, L. Wang, J. Liu and C. Chen, *ChemPhysMater*, 2025, **4**, 207–233.
381 L. Wang, Y. Zhang, L. Li, X. Geng, D. Dou, L. Yu, H. Jing and Y. Fan, *J. Hazard. Mater.*, 2023, **445**, 130512.
382 W. Hong, F. Zhang and Z. Wang, *Aquat. Toxicol.*, 2025, 107419.
383 M. Yu, J. He, X. Hu, B. Liu, W. Zhao, J. Sun and Q. Wang, *Adv. Compos. Hybrid Mater.*, 2025, **8**, 377.
384 Q. Peng, Z. Huang, G. Chen, Y. Zhang, X. Zhang, X.-J. Chen and Z. Hu, *Nanomaterials*, 2024, **14**, 556.
385 M. Lemaalem, N. Khossossi, G. Bouder, P. Dey and P. Carbonnière, *J. Power Sources*, 2023, **581**, 233482.
386 Y. Du, M. Wang, X. Ye, B. Liu, L. Han, S. H. M. Jafri, W. Liu, X. Zheng, Y. Ning and H. Li, *Crystals*, 2023, **13**, 912.
387 L. Guo, H. Shang, J. Peng, H. Li and H. Pan, *J. Mater. Chem. A*, 2025, **13**, 36436–36443.
388 Z. Lin, S. Dai, S. Yao, Q.-C. Lin, M. Fu, L.-H. Chung, B. Han and J. He, *Chem. Sci.*, 2025, **16**, 1948–1956.
389 L. Ou, B. Song, H. Liang, J. Liu, X. Feng, B. Deng, T. Sun and L. Shao, *Part. Fibre Toxicol.*, 2016, **13**, 1–24.
390 D. Cohen-Tanugi, *Nanoporous graphene membranes for desalination and gas separation*, PhD thesis, Massachusetts Institute of Technology, 2015.
391 J. W. Kang and H. J. Hwang, *J. Appl. Phys.*, 2004, **96**, 3900–3905.
392 A. Panahi, A. Shomali, M. H. Sabour and E. Ghafar-Zadeh, *J. Mol. Liq.*, 2019, **278**, 658–671.